Theoretical Study on the Origin of the Antiferromagnetic-Ferromagnetic Phase Transition and the Inverse Magnetocaloric Effect of FeRh

Theoretical Study on the Origin of the Antiferromagnetic-Ferromagnetic Phase Transition and the Inverse Magnetocaloric Effect of FeRh

Hidekazu Takahashi

September 2016

Theoretical Study on the Origin of the Antiferromagnetic-Ferromagnetic Phase Transition and the Inverse Magnetocaloric Effect of FeRh

Hidekazu Takahashi

Doctoral Program in Nano-Science and Nano-Technology

Submitted to the Graduate School of

Pure and Applied Sciences

in Partial Fulfillment of the Requirements

for the Degree of Doctor of Philosophy in

Science

at the

University of Tsukuba

Abstract

Theoretical Study on the Origin of the Antiferromagnetic-Ferromagnetic Phase Transition and the Inverse Magnetocaloric Effect of FeRh

Hidekazu Takahashi

Graduate School of Pure and Applied Sciences, University of Tsukuba

Recently, a great deal of attention has been drawn to room-temperature magnetic refrigeration technology (RTMR) based on the magnetocaloric effect (MCE). The materials that exhibit this effect are called magnetocaloric materials (MCMs). Likewise, RTMR using inverse magnetocaloric materials (IMCMs), which show the inverse magnetocaloric effect (IMCE), has also been attracting attention. In particular, the IMCE in FeRh has an antiferromagnetic (AFM)-ferromagnetic (FM) phase transition and exhibits a giant adiabatic temperature change (ΔT_{ad}) under a low applied magnetic field (ΔT_{ad} = –13 K under 1.95 T, i.e., –6.5 K per T). However, the magnitude of $|\Delta T_{ad}|$ for FeRh is still less than that required for practical applications (for example, about 20K for an air-conditioner). However, new MCMs and IMCMs superior to FeRh have yet to be discovered. Therefore, it is important to clarify the origin of the IMCE in FeRh. Moreover, the origin of the AFM-FM phase transition has not as yet been fully understood, and the electronic and magnetic structures on which this phase transition is based have also not been clarified, so it is essential that these are examined. Recently first principles calculations have been made. Even the most advanced first principles calculations cannot reproduce important physical quantities such as the total energy difference between the AFM and FM states (ΔE). This seems to be because the electronic correlation has not been adequately taken into account. Therefore, in this work, we examined the electronic and magnetic structures of FeRh using first principles calculations including the on-site Coulomb interaction (U) in order to obtain the data necessary to

understand the origins of the AFM-FM phase transition and the IMCE. This is the first time such calculations have been done.

We used the generalized gradient approximation (GGA) plus Hubbard U (GGA + U) to perform calculations for the AFM and FM states using the VASP program with the projector-augmented-wave (PAW) method. By choosing appropriate values of U for the Fe_{3d} and Rh_{4d} electrons, we succeeded in reproducing the AFM-FM phase transition quantitatively for the first time. Physical quantities such as ΔE, the lattice constant, the bulk modulus, Young's modulus, the magnetization, the critical magnetic field at 0 K ($H_c(0)$), the density of states (DOS), the band structures and the wavefunctions are consistent with experimental reports. In particular, the following important effects on the physical quantities obtained in the present work were found. (i) U strongly influences ΔE, $H_c(0)$ and the magnetic moment of the Fe atom, m_{Fe}. As the magnitude of U_{Rh} increases, the FM state gradually becomes more energetically advantageous compared with the AFM state. The m_{Fe} of the AFM state gradually approaches that of the FM state as the magnitude of U_{Fe} increases, while the m_{Fe} of the AFM state < m_{Fe} of the FM state when the magnitude of U_{Fe} is equal to zero. (ii) Changes in lattice constant more strongly influence m_{Fe} than the magnetic moment of the Rh atom, m_{Rh}. In particular, the magnitude relation of m_{Fe} values between the AFM and FM states is reversed near the observed lattice constant. (iii) The ratio of the density of states at the Fermi level (E_F) ($D(E_F)$) in the FM state to that in the AFM state ($D(E_F)_{FM}$ / $D(E_F)_{AFM}$) is large because the partial density of states (PDOS) at E_F ($PD(E_F)$) of the Fe atoms (especially the Fe_{3d} electrons) changes when changing from the AFM to the FM state. (iv) Strong hybridization of the orbitals of Fe and Rh atoms (especially, the Fe_{3d} and Rh_{4d} orbitals for the AFM and FM states, and the Fe_{3d}, Rh_{5p} and Rh_{4d} orbitals for the AFM state) comprising the wavefunctions of the valence band near E_F appears. Hybridization in the AFM state is different to that in the FM state, which reflects the difference between the interactions in the AFM and FM states. The interaction between Fe atoms via a Rh atom generated by this hybridization plays an important role in determining the magnetic state. From these results, the microscopic mechanisms for the differences between the electronic, magnetic and mechanical properties in the AFM and FM states can be understood. In particular, changes in physical properties, such as the electrical conductivity, that occur with the AFM-FM phase transition can be understood

from the theories of solid state physics, such as electron transport theory and so on, using the obtained physical quantities for the AFM and FM states such as $D(E_F)_{FM}$ / $D(E_F)_{AFM}$ and the band structures. Consequently, we can further determine the electronic and magnetic structures and understand them more deeply, enabling us to clarify the origins of the AFM-FM phase transition and the IMCE of FeRh.

Contents

Acknowledgement

I would like to express my sincere gratitude to my supervisor, Prof. Kenji Shiraishi of Nagoya University and to Prof. Susumu Okada who gave me the precious opportunity to study for a Ph.D. degree in their laboratory. From the start, they taught me how to devise a research plan and how to write a good paper, and then encouraged me to submit a dissertation. For this help, I shall remain eternally grateful. Moreover, I thank them kindly for their thoughtful discussions of the results of my computations and advising me how to explain them. I would also like to thank Assistant Prof. Masaaki Araidai of Nagoya University who taught me how to use the first principles band calculation program.

I am indebted to many colleagues in our team for their advice on computer system support. I thank Reiko Wada and Kayoko Hosono of Nagoya University for the many times they reserved the discussion room to hold meetings, and Shiromi Kikawada for providing much useful information to help me acquire credits for the doctoral course. I thank other teachers and secretaries who are part of the Doctoral Program in Nano-Science and Nano-Technology for advising me how to achieve the credits needed to gain the Ph.D degree.

Chapter1

Introduction

1.1 Background

Recently, a great deal of attention has been drawn to room-temperature magnetic refrigeration technology (RTMR) using magnetocaloric materials (MCMs) that exhibit the magnetocaloric effect (MCE).[1-6] This growing interest is due to the need to curtail or eliminate the use of refrigerants, which are greenhouse gases, and to the improvements that can be made in the efficiency of refrigerators, which the use of RTMR is expected to bring. According to Ref. 3, this efficiency is 20-30% higher than that of currently available vapor compression based systems In particular, eliminating a large amount of the loss associated with expansion and compression of gas, has a significant effect on the reduction in energy consumption.

MCE is a process whereby the temeperature in a material increases in response to a decrease in entropy caused by alignment of the magnetic moments in the material with increasing magnetic field. With decreasing magnetic field, the random alignment of the magnetic moments in the material causes an increase in entropy and thereby a decrease in temeperature. This can be illustrated by the concept of the magnetic refrigeration cycle shown in Fig. 1.

In magnetic refrigeration, there are several basic thermodynamic cycles, i.e., the Brayton cycle, the Ericsson cycle and the Carnot cycle.[4] Magnetic refrigeration utilizing the Brayton cycle in a MCM is detailed in the following using the *T*-*S* diagram of the thermal cycle shown in Fig. 2.

i) In adiabatic magnetization (increasing the magnetic field (*H*)), the temperature (*T*) in the MCM increases in step 1-2.

ii) The waste heat is released in step 2-3.

iii) In adiabatic demagnetization (decreasing *H*), the temperature in the MCM decreases in step 3-4.

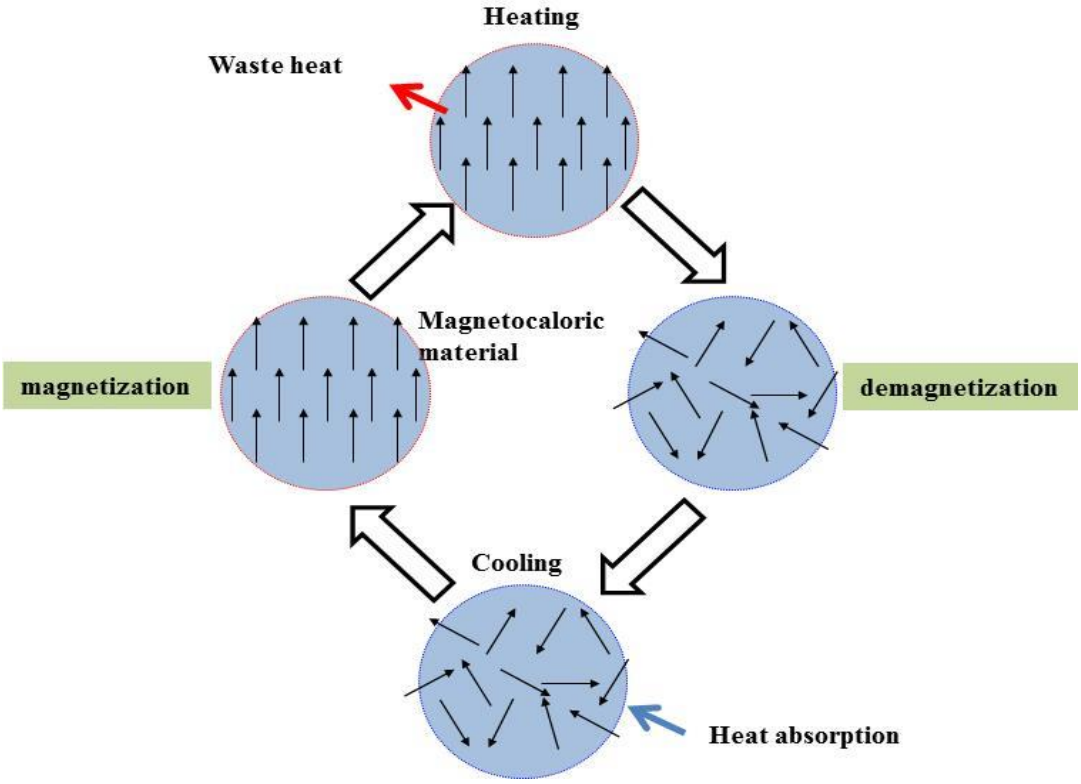

Fig. 1. The concept of the magnetic refrigeration cycle.

iv) The heat is absorbed in step 4-1.

The net work w of the Brayton cycle using a MCM is given by:

$$w = \oint dw = -\int_2^3 TdS - \int_4^1 TdS \,, \tag{1.1}$$

$$Q_{\text{abs}} = \int_4^1 TdS \,, \tag{1.2a}$$

$$Q_{\text{waste}} = \int_3^2 TdS \,, \tag{1.2b}$$

$$w = Q_{\text{waste}} - Q_{\text{abs}} \,, \tag{1.2c}$$

where Q_{waste} is the waste heat and Q_{abs} is the absorbed heat.

In order to assess the system performance, the coefficient of performance (COP) is defined by

$$\mathrm{COP} = \frac{Q_{\mathrm{abs}}}{w} . \qquad (1.3)$$

A high-performance system has large COP, and in order to make COP large, it is necessary to make Q_{abs} large for a given w. If there is a large change in entropy from 4 to 1, formula (1.2) shows that Q_{abs} is large, and therefore COP is large.

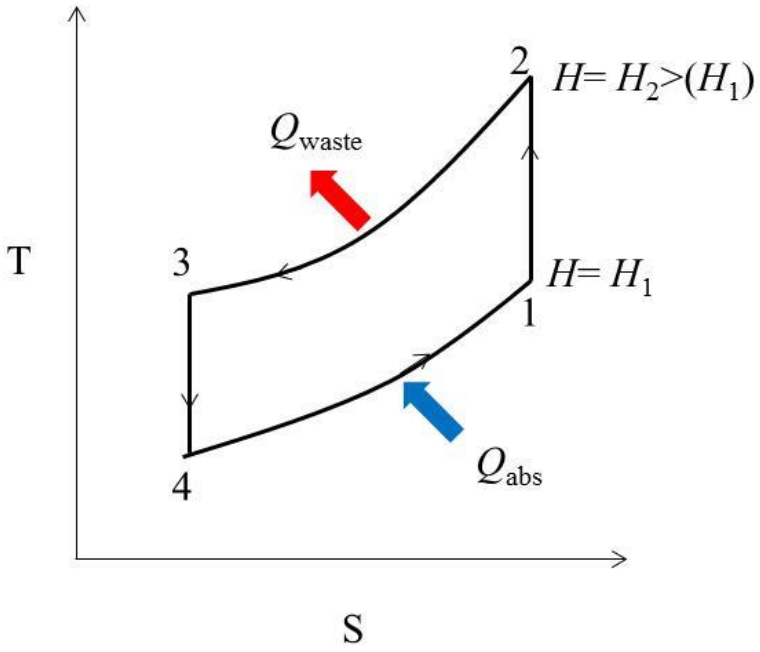

Fig. 2. The Brayton cycle using a MCM.

Recently, active magnetic regenerator (AMR) devices have been used in magnetic refrigeration. These devices consists of a porous bed of a magnetic refrigerant material such as a MCM which acts as both the agent that produces refrigeration and the regenerator for the heat transfer fluid.[1-2)] In the case of using a MCM, the AMR cycle consists of the following four cycles shown in Fig. 3. (a) magnetization, (b) flow from the cold heat exchanger to the hot heat exchanger, (c) demagnetization, and (d) flow from the hot heat exchanger to the cold heat exchanger. After the above cycle, the temperature in the cold heat exchanger decreases and temperature in the hot heat

exchanger increases. The AMR cycle is repeated until the temperature in the cold heat exchanger, T_{low}, is sufficiently low and the temperature in the hot heat exchanger, T_{high}, is sufficiently high. The temperature difference between the hot and cold heat exchangers (ΔT_{exh}) is $T_{high} - T_{low}$.

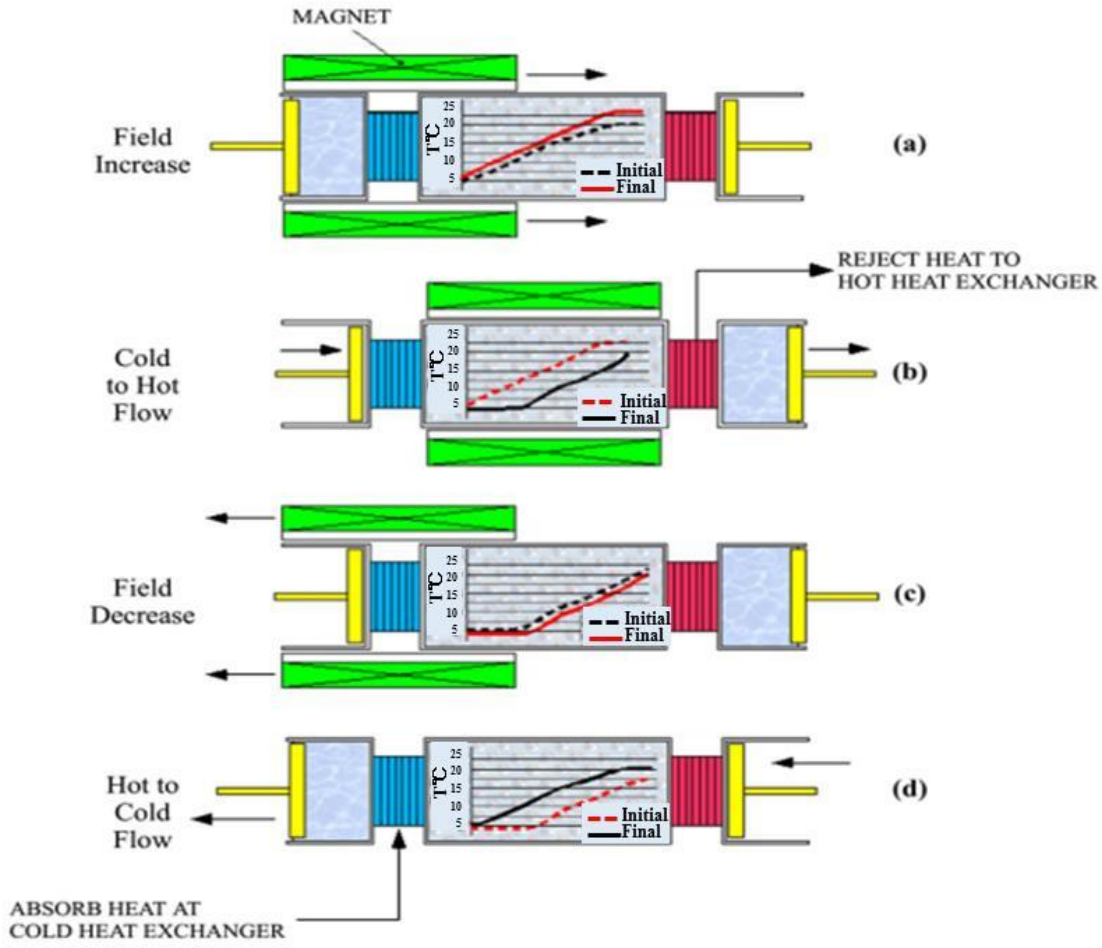

Fig. 3. The AMR cycle cited from Ref. 3.

A number of enhanced performance MCMs, including $Gd_5Si_2Ge_2$,[7] $MnAs_{1-x}Sb_x$,[8] $MnFeP_{0.45}As_{0.55}$,[9] $La(Fe_xSi_{1-x})_{13}H_y$,[10] and MnFe(P,Si),[11] have been found so far. The MCE in these materials occurs in the vicinity of the ferromagnetic (FM) – paramagnetic (PM) phase transition. Increasing the applied magnetic field to 10 T, generated by a superconducting magnet, or to 40 T generated by a pulsed magnetic field generator increases the strength of the MCE to a practical level. However, since

superconducting magnets and pulsed magnetic field generators are expensive, these cannot be justifiably used for commercial air conditioners.

Therefore, the attention has been redirected toward inverse magnetocaloric materials (IMCMs) such as FeRh,[12-14] Mn_3GaC,[15] (Co,Fe)MnP[16] and $Mn_{2-x}Cr_xSb$[17] because of the occurrence of a giant inverse magnetocaloric effect (IMCE) (IMCE is a process whereby the temeperature of a material decreases with increasing magnetic field and increases with decreasing magnetic field) under a low magnetic field generated by a Nd-Fe-B magnet (2T at most). The occurrence of the above IMCE is related to two complex phase transitions, the antiferromagnetic - ferromagnetic (AFM-FM) phase transition and the antiferromagnetic - ferrimagnetic (AFM-FI) phase transition, under an applied magnetic field.

Magnetic refrigeration utilizing the Brayton cycle in an IMCM can be described using the *T*-*S* diagram of the thermal cycle shown in Fig. 4.

i) With an adiabatically increasing *H*, the temperature in the IMCM decreases in step 1-2.

ii) The heat is absorbed in step 2-3.

iii) With an adiabatically decreasing *H*, the temperature in the IMCM increases in step 3-4.

iv) The waste heat is released in step 4-1.

The net work *w* of the Brayton cycle using an IMCM is given by:

$$w = \oint dw = -\int_2^3 TdS - \int_4^1 TdS \quad , \tag{1.4}$$

$$Q_{\text{waste}} = \int_1^4 TdS \quad , \tag{1.5a}$$

$$Q_{\text{abs}} = \int_2^3 TdS \quad , \tag{1.5b}$$

$$w = -Q_{\text{abs}} + Q_{\text{waste}} , \tag{1.5c}$$

where Q_{waste} is the waste heat and Q_{abs} is the absorbed heat.

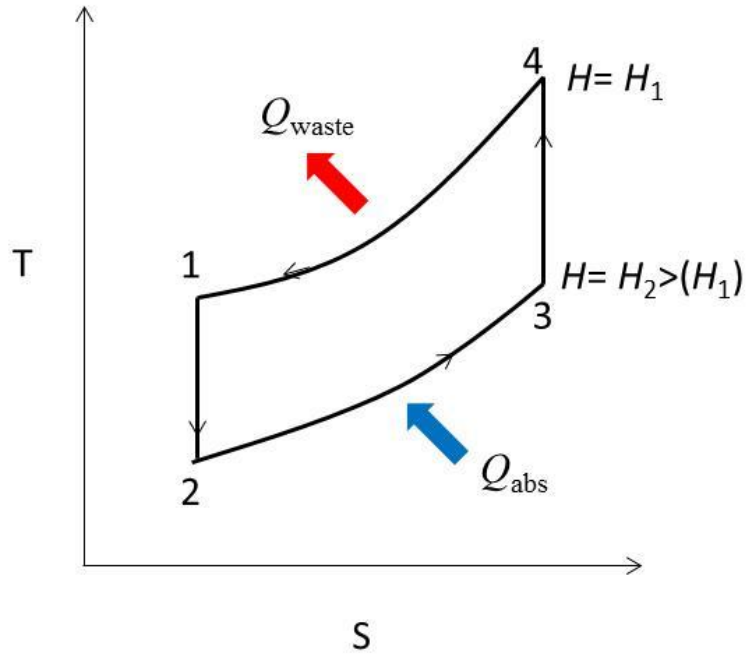

Fig. 4. The Brayton cycle using an IMCM.

1.2 Aim of the present work

1.2.1 Choice of FeRh

In particular, FeRh has a first order AFM-FM phase transition at $T_{tr} \approx 320 \sim 370$ K without a magnetic field and a FM-PM phase transition occuring at $T_c \approx 670$ K. Fig. 5 shows the phase diagram of FeRh alloy from Ref. 18. If the atomic concentration of Fe is several percent more than 50%, the AFM-FM phase transition disappears. The transition temperature increases with increasing Rh concentration from 48% to 55% and then decreases sharply.

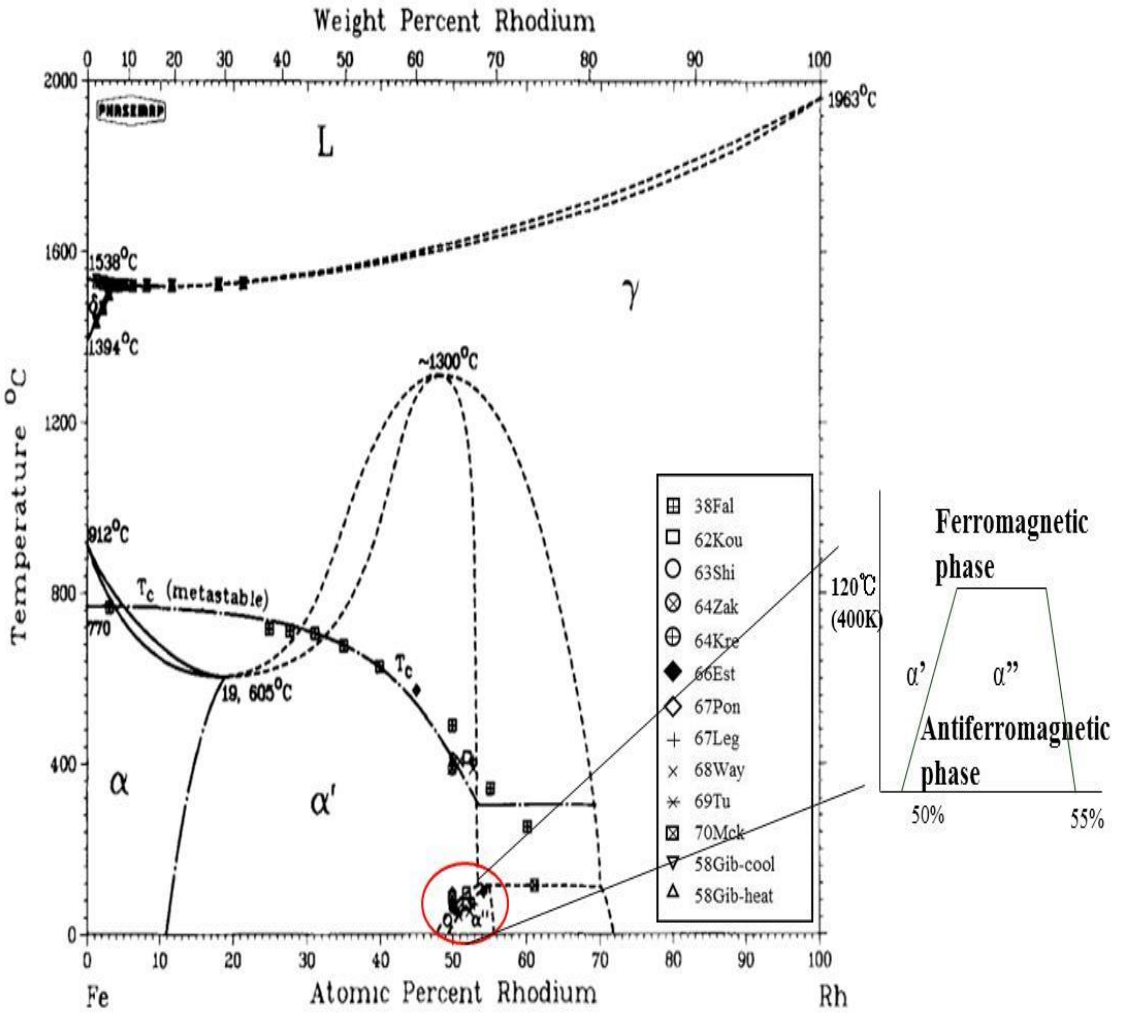

Fig. 5. The phase diagram of FeRh alloy. The diagram on the left is reproduced from Ref. 18.

FeRh exhibits a giant temperature change in an adiabatic process ($|\Delta T_{ad}|$) (ΔT_{ad} = –13 K under 1.95 T, i. e., –6.5 K per T) which is much larger than those of other MCMs ($|\Delta T_{ad}| < 7$ K under 2 T). It also shows a large entropy change in an isothermal process ($|\Delta S_{iso}|$) ($\Delta S_{iso} > 20$ J/(kg K) under 1.95 T) which is similar to that of $La(Fe_xSi_{1-x})_{13}H_y$ and MnFe(P,Si). $|\Delta T_{ad}|$ versus $|\Delta S_{iso}|$ for FeRh and other MCMs is summaried in Fig. 6. ΔT_{ad} and ΔS_{iso} for MCMs and IMCMs are indicated in Fig. 7 (pressure P is constant). In Fig. 7(a), ΔT_{ad} and ΔS_{iso} for MCMs have positive and negative values, respectively, while those for IMCMs, shown in Fig. 7(b), have negative and positive values, respectively.

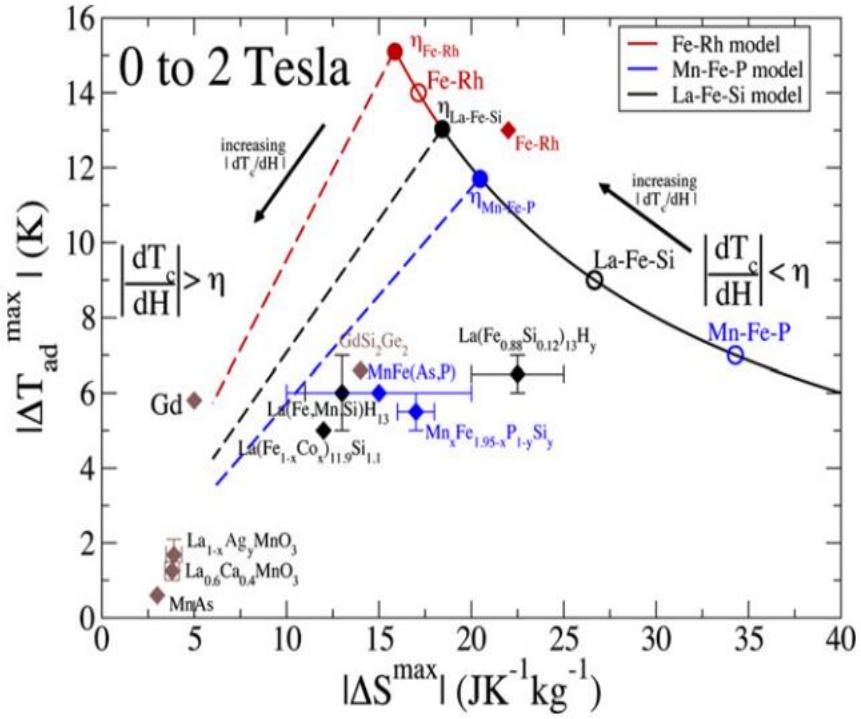

Fig. 6. $|\Delta T_{ad}|$ versus $|\Delta S_{iso}|$ for representative room-temperature MCMs and an IMCM cited from Ref. 5.

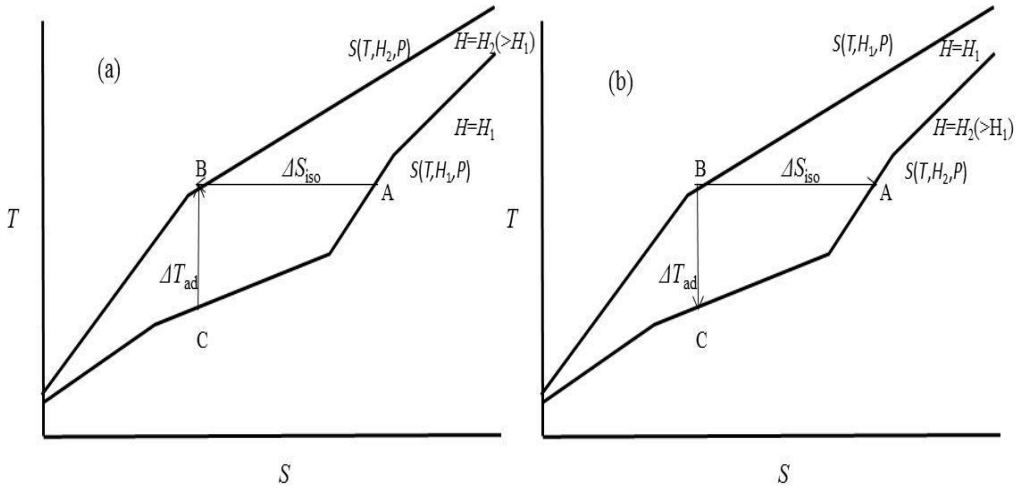

Fig. 7. ΔT_{ad} and ΔS_{iso} for (a) MCE and (b) IMCE are shown on the *T*-*S* diagram.

However, the magnitude of $|\Delta T_{ad}|$ of FeRh is still lower than that needed to realize large $|\Delta T_{exh}|$ (for example, about 20K is needed for an air-conditioner). Although recent studies suggest that $|\Delta T_{ad}|$ can be increased up to 18 K per T,[19,20] new MCMs

and IMCMs with superior performance to FeRh have yet to be found. Therefore, it is important to clarify the origin of the IMCE in FeRh.

The experimental and theoretical research reported to date including the origin of the AFM-FM phase transition and the electronic and magnetic structures of the materials, which are the foundation for this phase transition as well as the origin of the IMCE, are summarized in the following.

1.2.2 Experiments on FeRh

Since the discovery of FeRh by Fallot in 1938,[21] various experiments [22-45,58] to determine the following physical quantities have been made.

(i) The lattice constant of the AFM and FM states (a_{AFM}, a_{FM}) (for, example, 2.981 Å for a_{AFM} and 2.999 Å for a_{FM} from Ref. 22),[22,23]

(ii) the difference between the minimum total energies of the FM and AFM states (ΔE), which is related to T_{tr} (2.80 meV)[24],

(iii) the magnetic moments of Fe and Rh atoms in the AFM and FM states (m_{Fe}, m_{Rh}) (for example, m_{Fe} = 3.30μ_B for the AFM state and 3.17μ_B for the FM state ; m_{Rh} = 0μ_B for the AFM state and 0.97μ_B for the FM state from Ref. 26),[25,26,27]

(iv) the applied field necessary for the AFM-FM phase transition, which is equal to the critical magnetic field at 0 K ($H_c(0)$)) (for example, 21.2 T from Ref. 30),[28,29,30]

(v) the Sommerfeld coefficient, γ, of the AFM and FM states (γ_{AFM}, γ_{FM}) (for example, 10.5 mJ/(kg K^2) for γ_{AFM} and 62.5 mJ/(kg K^2) for γ_{FM} from Ref. 38),[37,38]

(vi) the bulk modulus of the AFM and FM states (B_{AFM}, B_{FM}) (for example, 142 Gpa for B_{AFM} and 158 Gpa for B_{FM} from Ref. 58),[24,58]

(vii) Young's modulus of the AFM and FM states (E_{YAFM}, E_{YFM}) (for example, 170 Gpa for E_{YAFM} and 190 Gpa for E_{YFM} from Ref. 58),[24,43,58]

(viii) the isothermal entropy change (ΔS_{iso})(21.0 J/(kg K) at 307 K from Ref.

12)[12,13,14,30] under an applied magnetic field, and

(ix) the entropy change (ΔS = 13.6 ~ 19.7 J/(kg K))[23,24,29,37,44,45] without an applied magnetic field.

From the reported experimental results, it turns out that the electronic and magnetic structures of the AFM-FM states change drastically and changes in the various physical quantities, such as the magnetic moments of the Fe and Rh atoms, the Sommerfeld coefficient γ, the bulk modulus and Young's modulus, occur, which contribute to the origin of the AFM-FM phase transition. It has been found that the magnetoresistance,[31] magnetorestriction[33,34] and electrical resistivity[31,39,40,41,42] change with the AFM-FM phase transition. However, the mechanisms for these have not yet been adequately explained. In addition, the reason why the values of $|\Delta S|$ are large is not clearly understood. From the above experiments on the IMCE, some detailed features have been revealed. However, the reason why the values of $|\Delta T_{ad}|$ are large are also not clearly understood.

Moreover, recently, the coexistence of AFM and FM domains near T_{tr} has been observed. The mechanism of formation of these domains and the influence of them on the physical properties has been investigated using various experimental methods.[46-56] However, this mechanism has also not been adequately understood.

1.2.3 Reported theoretical research on FeRh

Various theoretical investigations into the origins of the AFM-FM phase transition and the IMCE have also been made.[56-84] For example, Kittel proposed the exchange inversion model for the AFM-FM phase transition.[57] One of the exchange constants is linear passing through zero near a critical value of the lattice coordinate that characterizes this transition. In order to gain an understanding of the AFM-FM phase transition, various theories have been proposed by investigating the electronic and magnetic structures using first principles calculations and model Hamiltonian calculations, and the phase transition with free energy calculations.[58-84] The origin of

the AFM-FM phase transition is summarized in the following. The AFM state is stable at low temperature because the Helmholtz free energy of the AFM state (F_{AFM}) is less than the Helmholtz free energy of the FM state (F_{FM}). The AFM state coexists with the FM state at T_{tr} because $F_{AFM} = F_{FM}$. The FM state is stable at high temperature because $F_{AFM} > F_{FM}$. The influence of the difference between the combined electronic, magnetic and lattice entropies of the AFM and FM states triggers this phase transition. However, the magnitudes and the ratios of these reported entropies are different. All of these currently remain the subject of debate.

In particular, research with first principles calculations has increased since 1980, For example, the following theoretical investigations have been reported.

Moruzzi and Marcus[65-68] calculated the electronic and magnetic structures in the PM state, two kinds of AFM state and the FM state using first principles calculations based on the augmented spherical method (ASW) and the fixed-spin-moment procedure. The density of states (DOS), total energies and magnetic moments were investigated in detail. However, ΔE was calculated to be about 2 mRy/atom, and was larger near the observed lattice constant than the experimentally measured one. Moreover, they assumed that if the zero point energy correction of the AF state was larger than that of the FM state, ΔE would be reduced to 0.3 mRy/atom.

Szajek and Morkowski[69,70] investigated the electronic and magnetic structures in the AFM and FM states using first principles calculations based on the self-consistent spin-polarized linear muffin-tin orbital atomic-sphere approximation (LMTO-ASA) in order to discover the origins of the AFM-FM and FM-PM phase transitions. However, ΔE was about 2.2 mRy/atom and was larger near the observed lattice constant than the experimentally measured one.

Kaneta et al.[77] calculated the electronic and magnetic structures using first principles calculations based on the generalized gradient approximation (GGA) in order to clarify the relationship between the magnetic properties and structural defects in a FeRh inter-metallic compound. Although the AFM state is stable at low temperature in defect-free FeRh, it becomes unstable as the site-exchange defect density increases. They obtained a value for ΔE of 2.66 mRy/atom in the case of

defect-free FeRh.

Sandratskii and Mavropoulos[78] calculated the electronic and magnetic structures in the AFM and FM states using density functional theory (DFT) within the ASW method. ΔE was 1 mRy/atom and was inconsistent with the experimental results. They performed Monte Carlo simulations of a Heisenberg-like model based on the above data on the exchange interactions and obtained the dependencies on temperature of the magnetization of the system, the magnetic moments of the Fe and Rh atoms and the magnetic susceptibilities.

Deák et al.[83] investigated the AFM-FM phase transition using a self-consistent relativistic disordered local moment scheme. The obtained T_{tr} (= 461 K at lattice constant a = 3.08 Å) was inconsistent with the experimental value. Moreover, ΔE was 3.91 mRy/formula unit and disagreed with the experimental reports.

There are a few examples of detailed theoretical investigations on the origin of the IMCE.[56,82] Staunton et al.[82] calculated the isothermal entropy change ΔS_{iso} of $Fe_{1-x}Rh_x$-$Rh_{1-y}Fe_y$ under an applied magnetic field using *ab initio* disordered local moment theory for a magnetic material in an external magnetic field at finite temperature for applications to systems with quenched disorder. The value they obtained for T_{tr} in the case of FeRh was 495 K and ΔS_{iso} under an applied magnetic field of 2 T near T_{tr} was 21.1 J/(kg K) which were consistent with the experimentally obtained values. They did not show the detailed electronic and magnetic structures of FeRh.

1.2.4 Problems of previous studies and approach of the present work

The advanced first principles calculations mentioned in the above reports cannot reproduce important physical quantities such as ΔE. In particular, if the calculations of ΔE are inconsistent with the experimentally measured values, the Helmholtz free energy difference between the AFM and FM states can not be calculated. Therefore, the origins of the AFM-FM phase transition and the IMCE cannot be clarified.

Generally, in alloys containing 3d and 4d transition metals, it is important to take into account the electronic correlation. However, this is not considered in any of the reported calculations. The problems cited above occur because this electronic correlation is not adequately taken into account. Therefore, in this work, we use first principles calculations including the on-site Coulomb interaction (U) to determine the electronic and magnetic structures of FeRh, so that we have, for the first time, the data needed to understand the origins of the AFM-FM phase transition and the IMCE.

1.3 Outline of this dissertation

The structure of this dissertation is as follows. In chapter 2, before describing the method used for the first principles calculations, we provide a summary of the basic elements needed to carry out these calculations, including calculation theories, approximations and algorithms, in order that we are able to fully understand the results of the calculations. In chapter 3, details of the calculation model and the computational method for the first principles calculations including U of FeRh are described. In order to give an indication of the validity of the first principles calculations including U for determining the electronic and magnetic structures of FeRh, the influence of U on these structures for Fe and Rh crystals is investigated. Various physical quantities of Fe and Rh crystals are calculated and are compared with experimental results. Moreover, the bulk modulus and Young's modulus of FeRh for the AFM and FM states are also calculated and compared with experimental results. In chapter 4, physical quantities such as ΔE and $H_c(0)$, the lattice constant, the magnetization, DOS, the band structures and the wavefunctions are calculated and compared with experimental results. From the results obtained, the microscopic origin of the change in the electronic and magnetic structures leading to the AFM-FM phase transition is discussed. The change in electrical conductivity in the AFM-FM phase transition is investigated using the physical quantities obtained above and solid state

physics. The origin of this change is discussed and compared with other publications. In chapter 5, the results obtained in this work are summarized. In the appendices, complementary information that helps provide a deeper understanding of the results of the present work is presented.

Chapter 2

Theoretical background to first principles calculations

In this chapter, the method for calculating the electronic structure of a many-body system based on first principles calculations is explained in detail.

2.1 Born-Oppenheimer approximation

The electronic structure of a many-body system can be investigated using the following Schrödinger equation. The Hamiltonian operator is given by,

$$\hat{H} = -\frac{\hbar^2}{2m_e}\sum_{\mu=1}^{N_e}\nabla_\mu^2 - \frac{\hbar^2}{2}\sum_{k=1}^{N_n}\frac{\nabla_k^2}{M_k} - \sum_{\mu=1}^{N_e}\sum_{k=1}^{N_n}\frac{Z_k e^2}{|\mathbf{r}_\mu - \mathbf{R}_k|} + \sum_{\mu=1}^{N_e}\sum_{\nu>\mu}^{N_e}\frac{e^2}{|\mathbf{r}_\mu - \mathbf{r}_\nu|} + \sum_{j=1}^{N_n}\sum_{k>j}^{N_n}\frac{Z_k Z_j e^2}{|\mathbf{R}_j - \mathbf{R}_k|}, \quad (2.1.1)$$

where m_e and M_k are the masses of the electron and the k-th nuclei, respectively, Z_k is the atomic number of the k-th nucleus, e is the electric charge, $\hbar$ (= $h/2\pi$. h is the planck constant) is the reduced Planck constant, $\mathbf{r}_1,\mathbf{r}_2,\ldots,\mathbf{r}_{Ne}$ represent the coordinates of the N_e electrons in the solid state matter, and $\mathbf{R}_1,\ldots,\mathbf{R}_{Nn}$ are the nuclear coordinates of the N_n nuclei. The first and second terms are the kinetic energies of the N_e electrons and the N_n nuclei, respectively. The third term is the potential energy between the N_e electrons and the N_n nuclei. The fourth term is the potential energy between the N_e electrons. The fifth term is the potential energy between the N_n nuclei.

When the Born-Oppenheimer approximation[85], which assumes that the positions of nuclei can be fixed because the nuclei are much heavier than the electrons, is used, the second term can be neglected. Since the fifth term does not influence the electronic structure, this term can also be neglected. The Schrödinger equation using this approximation for the Hamiltonian operator is as follows.

$$\hat{H}_{el}\varphi(\mathbf{r}) = \varepsilon_{el}\varphi(\mathbf{r}), \tag{2.1.2}$$

$$\hat{H}_{el} = -\frac{\hbar^2}{2m_e}\sum_{i=1}^{N_e}\nabla_i^2 - \sum_{\mu=1}^{N_e}\sum_{k=1}^{N_n}\frac{Z_k e^2}{|\mathbf{r}_\mu - \mathbf{R}_k|} + \sum_{\mu=1}^{N_e}\sum_{\nu>\mu}^{N_e}\frac{e^2}{|\mathbf{r}_\mu - \mathbf{r}_\nu|}, \tag{2.1.3}$$

where $\varphi(\mathbf{r})$ is the wavefunction of the system.

The methods for solving the electronic structure of a many-body system using this Hamiltonian are detailed in the following.

2.2 Thomas-Fermi method

Thomas[86] and Fermi[87] proposed a model for determining the electronic structures of many-body systems using semi-classical theory. This method is formulated using the electronic density *n* instead of solving the wavefunction of the Schrödinger equation. It can be thought of as a precursor to DFT.

The Thomas-Fermi method is described in the following. The energy functional $E_{TF}[n]$ contains three terms, i. e., the kinetic energy $T[n]$, the interaction with the external potential $V_{ext}[n]$ and the electron-electron interaction $V_{ee}[n]$.

$$E_{TF}[n] = T[n] + V_{ext}[n] + V_{ee}[n], \tag{2.2.1}$$

$$T[n] = C_F\int n(\mathbf{r})^{\frac{5}{3}}d\mathbf{r}, \tag{2.2.2}$$

where $C_F = \frac{3h^2}{10m_e}\left(\frac{3}{8\pi}\right)^{2/3}$,

$$V_{ext}[n] = e\int v_{ext}\,n(\mathbf{r})d\mathbf{r}, \tag{2.2.3}$$

$$V_{ee} = \frac{e^2}{2}\iint\frac{n(\mathbf{r}_1)n(\mathbf{r}_2)}{|\mathbf{r}_1 - \mathbf{r}_2|}d\mathbf{r}_1 d\mathbf{r}_2. \tag{2.2.4}$$

The Lagrange multiplier μ is introduced to impose the condition that *n* is given by

$$\int n(\mathbf{r})d\mathbf{r} = N_e . \tag{2.2.5}$$

Minimization with respect to n is carried out.

$$\frac{\delta}{\delta n}\{E_{TF}(n) - \mu[\int n(\mathbf{r})d\mathbf{r} - N_e]\} = 0 , \tag{2.2.6}$$

$$\mu = \frac{5}{3} C_F [n(\mathbf{r})]^{2/3} + ev_{ext}(\mathbf{r}) + e^2 \int \frac{n(\mathbf{r}')}{|\mathbf{r} - \mathbf{r}'|} d\mathbf{r}' , \tag{2.2.7}$$

$$\phi(\mathbf{r}) = e\int \frac{n(\mathbf{r}')}{|\mathbf{r} - \mathbf{r}'|} d\mathbf{r}' . \tag{2.2.8}$$

Using Poisson's equation,

$$-\nabla^2 \phi(\mathbf{r}) = 4\pi e n(\mathbf{r}), \tag{2.2.9}$$

and the electron density

$$n(\mathbf{r}) = \left(\frac{3}{5C_F}\right)^{3/2} [\mu - ev_{ext}(\mathbf{r}) - e\phi(\mathbf{r})]^{3/2} \tag{2.2.10}$$

extracted from (2.2.7), one obtains the differential equation:

$$\nabla^2 \phi = -4\pi e \left(\frac{3}{5C_F}\right)^{3/2} [\mu - ev_{ext}(\mathbf{r}) - e\phi(\mathbf{r})]^{3/2} . \tag{2.2.11}$$

This is the Thomas-Fermi equation.

2.3 Density functional theory

2.3.1 Hohenberg and Kohn theorem

The Schrödinger equation for the many body problem is solved using DFT proposed by Hohenberg and Kohn in 1964.[88] We consider a collection of an arbitrary number of electrons, enclosed in a large box and moving under the influence of an external potential $v(\mathbf{r})$ and the mutual Coulomb repulsion. The Hamiltonian of the system is given by

$$\hat{H} = T + V + U, \tag{2.3.1}$$

$$T = \frac{\hbar^2}{2m_e} \int \nabla\phi^*(\mathbf{r}) \nabla\phi(\mathbf{r}) d\mathbf{r}, \tag{2.3.2}$$

$$V = \int v(\mathbf{r}) \phi^*(\mathbf{r}) \phi(\mathbf{r}) d\mathbf{r}, \tag{2.3.3}$$

$$U = \frac{e^2}{2} \int \frac{\phi^*(\mathbf{r}) \phi^*(\mathbf{r}') \phi(\mathbf{r}') \phi(\mathbf{r})}{|\mathbf{r} - \mathbf{r}'|} d\mathbf{r} d\mathbf{r}'. \tag{2.3.4}$$

We assume for simplicity that the ground state of the system is nondegenerate. The electron density in the ground state ψ is given by

$$n(\mathbf{r}) \equiv \left(\Psi, \phi(\mathbf{r}^*) \phi(\mathbf{r}) \Psi\right). \tag{2.3.5}$$

We will show that $v(\mathbf{r})$ is a unique function of $n(\mathbf{r})$, apart from a trivial constant. We have the minimal property of the ground state,

$$E' = \left(\Psi', \hat{H}' \Psi'\right) < \left(\Psi, \hat{H}' \Psi\right) = \left(\Psi, \left(\hat{H} + V' - V\right) \Psi\right),$$

so that

$$E' < E + \int \left[v'(\mathbf{r}) - v(\mathbf{r})\right] n(\mathbf{r}) d\mathbf{r}. \tag{2.3.6}$$

Interchanging the primed and unprimed quantities, we find

$$E < E' + \int \left[v(\mathbf{r}) - v'(\mathbf{r})\right] n(\mathbf{r}) d\mathbf{r}. \tag{2.3.7}$$

Addition of (2.3.6) and (2.3.7) leads to the inconsistency

$$E + E' < E + E'. \tag{2.3.8}$$

Thus $v(\mathbf{r})$ is a unique functional of $n(\mathbf{r})$. If H is fixed by $v(\mathbf{r})$, the many particle ground state is a unique functional of $n(\mathbf{r})$.

Since ψ is a functional of $n(\mathbf{r})$, so evidently is the kinetic and interaction energy. We define

$$F[n(r)] \equiv (\Psi, (T+U)\Psi). \tag{2.3.9}$$

The energy functional is

$$E_v[n] \equiv \int v(\mathbf{r}) n(\mathbf{r}) d\mathbf{r} + F[n]. \tag{2.3.10}$$

For the correct $n(\mathbf{r})$, $E_v[n]$ equals the ground state energy E. We impose the following restriction:

$$\int n(\mathbf{r}) d\mathbf{r} = N. \tag{2.3.11}$$

The energy functional of ψ'

$$E_v[\Psi'] \equiv (\Psi', V\Psi') + (\Psi', (T+U)\Psi') \tag{2.3.12}$$

has a minimum in the ground state ψ, relative to the arbitrary variation in the state ψ', in which the number of particles is kept constant. We let ψ' be the ground state associated with a different external potential v'(r). Using (2.3.9) and (2.3.12)

$$E_v[\Psi'] = \int v(\mathbf{r})n'(\mathbf{r})d\mathbf{r} + F[n'],$$

$$> E_v[\Psi] = \int v(\mathbf{r})n(\mathbf{r})d\mathbf{r} + F[n]. \quad (2.3.13)$$

Thus, the minimal property of the energy functional (2.3.10) is established relative to all densities $n'(\mathbf{r})$ which are associated with some external potential $v'(\mathbf{r})$.

2.3.2 Kohn and Sham equation

This was basically formulated by Kohn and Sham in 1965.[89] The Hohenberg-Kohn theorem states that the total energy of the ground-state of the system can be expressed by a function of the electron density $n(r)$. The ground state energy can be variationally obtained. The density that minimizes the total energy is the exact ground-state density. The energy functional can also be expressed by

$$E[n] = T_s[n] + V_{ext}[n] + V_H[n] + E_{XC}[n], \quad (2.3.14)$$

$$V_{ext}[n] = \int v_{ext} n(\mathbf{r})d\mathbf{r}, \quad (2.3.15)$$

$$V_H = \frac{e^2}{2}\iint \frac{n(\mathbf{r}_1)n(\mathbf{r}_2)}{|\mathbf{r}_1 - \mathbf{r}_2|} d\mathbf{r}_1 d\mathbf{r}_2, \quad (2.3.16)$$

where T_s[n] is the kinetic energy of a system of noninteracting electrons with density $n(\mathbf{r})$, V_{ext} is the electron-nucleus interaction, V_H is the electron-electron Coulomb repulsion, and E_{XC}[n] is the exchange-correlation energy of an interacting system with density n($\mathbf{r}$). If $n(\mathbf{r})$ is sufficiently slowly varing, one can show that

$$E_{XC} = \int n(\mathbf{r})\varepsilon_{XC}(n(\mathbf{r}))d\mathbf{r}, \quad (2.3.17)$$

where ε_{XC} ($n(\mathbf{r})$)is the exchange-correlation energy per particle of an homogeneous electron gas of density n (this approximation is called as local density approximations (LDA) detailed below).

From the stationary property of equation (2.3.14), we obtain, subject to the condition

$$\int \delta n(\mathbf{r}) d\mathbf{r} = 0. \tag{2.3.18}$$

the equation

$$\int \delta n(\mathbf{r}) \left\{ \varphi(\mathbf{r}) + \frac{\delta T_s[n]}{\delta n(\mathbf{r})} + \mu_{XC}[n(\mathbf{r})] \right\} d\mathbf{r} = 0, \tag{2.3.19}$$

where

$$\varphi(\mathbf{r}) = v_{ext} + e^2 \int \frac{n(\mathbf{r}')}{|\mathbf{r} - \mathbf{r}'|} d\mathbf{r}', \tag{2.3.20}$$

and

$$\mu_{XC}[n(\mathbf{r})] = \frac{d(n\varepsilon_{XC}(n))}{dn} \tag{2.3.21}$$

is the exchange and correlation contributions to the chemical potential of a uniform gas of density n(r).

For a given $\varphi(r)$, one obtains the n(r) which satisfies these equations from

$$\left[-\frac{\hbar^2}{2m_e} \nabla^2 + \varphi(\mathbf{r}) + \mu_{XC}[n(\mathbf{r})] \right] \phi_i = \varepsilon_i \phi_i, \tag{2.3.22}$$

and setting

$$n[\mathbf{r}] = \sum_i^N |\phi_i|^2, \tag{2.3.23}$$

where N is the number of electrons.

Equations (2.3.20)-(2.3.23) have to be solved self-consistently. One begins with an assumed n(r), constructs $\varphi(r)$ from (2.3.20) and μ_{XC} from (2.3.21), and finds a new n(r) from (2.3.22)-(2.3.23). The total energy E is given by

$$E = \sum_{i}^{N} \varepsilon_i - \frac{e^2}{2} \iint \frac{n(\mathbf{r}_1) n(\mathbf{r}_2)}{|\mathbf{r}_1 - \mathbf{r}_2|} d\mathbf{r}_1 d\mathbf{r}_2 + \int n(\mathbf{r}) [\varepsilon_{XC}(n(\mathbf{r})) - \mu_{XC}(n(\mathbf{r}))] d\mathbf{r} . \quad (2.3.24)$$

2.4 Local density approximation

LDA are a class of approximations to the exchange–correlation (XC) energy functional E_{XC} in DFT that depends solely upon the value of the electron density at each point in space given by (2.3.17).

Moreover, we can separate E_{XC} into the exchange energy functional (E_X) and correlation energy functional (E_C).

$$E_{XC} = E_X + E_C . \quad (2.4.1)$$

$$E_X = \int n(\mathbf{r}) \varepsilon_X(n(\mathbf{r})) d\mathbf{r} , \quad (2.4.2)$$

$$E_C = \int n(\mathbf{r}) \varepsilon_C(n(\mathbf{r})) d\mathbf{r} , \quad (2.4.3)$$

where ε_X ($n(\mathbf{r})$) and ε_C ($n(\mathbf{r})$) are the exchange and correlation energies per particle of an homogeneous electron gas of density n, respectively. Energies are expressed in Hartree units.

For example, according to Dirac [90)]

$$E_X = -C_X \int n(\mathbf{r})^{4/3} d\mathbf{r} ,$$

$$C_X = \frac{3}{4} \left(\frac{3}{\pi} \right)^{1/3} . \quad (2.4.4)$$

Using the following r_s.

$$\varepsilon_X(r_s) = -\frac{3}{4\pi} \left(\frac{9\pi}{4} \right)^{1/3} \frac{1}{r_s} , \quad (2.4.5)$$

$$r_s = \left(\frac{3}{4\pi n}\right)^{1/3}. \tag{2.4.6}$$

Similarly, several kinds of E_C have been proposed by various researchers using the following r_s.

From Gell-Mann and Brueckner,[91] and Carr and Maradudin.[92]

$$\varepsilon_C(r_s) = A\ln r_s + B + r_s(C\ln r_s + D), \tag{2.4.7}$$

A=0.0311, B=–0.048,

C=0.009, D=–0.018.

The ε_{XC} was calculated by Ceperley and Alder[93] using Monte Carlo methods and was parameterized by Perdew and Zunger.[94]

$$\varepsilon_C(r_s) = \frac{\gamma}{1+\beta_1 r_s^{1/2} + \beta_2 r_s} \qquad \text{if } r_s \geq 1, \tag{2.4.8}$$

$$\varepsilon_C(r_s) = A\ln r_s + B + r_s(C\ln r_s + D) \quad \text{if } r_s < 1, \tag{2.4.9}$$

where γ, β_1, β_2,A, B, C *and* D are parameters.

The local spin-density approximation (LSDA) is a straightforward generalization of the LDA to include electron spin. The exchange-correlation energy regarding the spin polarization $E_{XC}^{LSDA}(n_\uparrow, n_\downarrow)$ is given by

$$E_{XC}^{LSDA}(n_\uparrow, n_\downarrow) = \int n(\mathbf{r})\varepsilon_{XC}(n_\uparrow(\mathbf{r}), n_\downarrow(\mathbf{r}))d\mathbf{r}, \tag{2.4.10}$$

where $\varepsilon_{XC}(n_\uparrow, n_\downarrow)$ is the exchange-correlation energy per particle.

$$E_X[n_\uparrow, n_\downarrow] = \frac{1}{2}\left(E_X[2n_\uparrow(\mathbf{r})] + E_X[2n_\downarrow(\mathbf{r})]\right), \tag{2.4.11}$$

$$\varepsilon_C(r_s,\zeta) = \varepsilon_C(r_s,0) + \left[\varepsilon_C(r_s,1) - \varepsilon_C(r_s,0)\right] f(\zeta), \tag{2.4.12}$$

where $f(\zeta)=\frac{1}{2}\frac{\left[(1+\zeta)^{4/3}+(1-\zeta)^{4/3}-2\right]}{\left(2^{1/3}-1\right)}$, (2.4.13)

and

$$\zeta=(n_\uparrow-n_\downarrow)/n\,. \tag{2.4.14}$$

2.5 Generalized gradient approximation

GGA goes beyond LDA. The typical form of GGA functionals [95,96] is expressed by

$$E_{XC}(n_\uparrow,n_\downarrow)=\int n(\mathbf{r})\varepsilon_{XC}(n_\uparrow,n_\downarrow,\nabla n_\uparrow,\nabla n_\downarrow)d\mathbf{r}\,. \tag{2.5.1}$$

For example, the Perdew-Burke-Ernzerhof (PBE) exchange-correlation energy functional ($E_{XC}^{PBE-GGA}$) is separated into the exchange energy functional ($E_X^{PBE-GGA}$) and the correlation energy functional ($E_C^{PBE-GGA}$).

$$E_{XC}^{PBE-GGA}=E_X^{PBE-GGA}+E_C^{PBE-GGA}. \tag{2.5.2}$$

$E_C^{PBE-GGA}$ is given by

$$E_C^{PBE-GGA}=\int d\mathbf{r}n(\mathbf{r})\left(\varepsilon_C^{hom}(r_s,\zeta)+H(r_s,\zeta,\tau)\right), \tag{2.5.3}$$

where $\varepsilon_C^{hom}(r_s,\zeta)$ is the exchange energy of a homogeneous electron gas.

$$\varepsilon_C^{hom}(r_s,\zeta)=\left(e^2/a_0\right)\phi^3\left[\gamma\, ln(r_s/a_0)-\varpi\right],$$

$$H(r_s,\zeta,\tau)=\frac{e^2}{a_0}\gamma\phi^3\left(1+\frac{\beta}{\gamma}\tau^2\frac{1+A\tau^2}{1+A\tau^2+A^2\tau^4}\right). \tag{2.5.4}$$

where e is the elementary electric charge,

a_0 is the Bohr radius,

$\beta = 0.066725$,

$\gamma = (1-ln2)/\pi^2 = 0.031091$,

$\varpi = 0.046644$,

$\phi = \left((1+\zeta)^{2/3} + (1-\zeta)^{2/3}\right)/2$,

$\tau = |\nabla n|/2\phi k_s n$,

$k_s = \sqrt{4k_F/\pi a_0}$, k_s is the Thomas-Fermi screening wavenumber

$k_F = (3\pi^2 n)^{1/3}$, and

$$A = \frac{\beta}{\gamma}\left[exp\left(\frac{-\varepsilon_c^{hom}}{\left(\gamma\phi^3 \frac{e^2}{a_0}\right)}\right) - 1\right]^{-1}. \qquad (2.5.5)$$

where the energies are expressed in Hartree units.

$E_X^{PBE-GGA}$ is given by

$$E_X^{PBE-GGA} = \int d\mathbf{r}\,\varepsilon_X^{hom}(n) F_X(s), \qquad (2.5.6)$$

$$\varepsilon_X^{hom}(n) = -3e^2 k_F/4\pi, \qquad (2.5.7)$$

$$F_X(s) = 1 + \kappa - \frac{\kappa}{\left(1 + \mu s^2/\kappa\right)}, \qquad (2.5.8)$$

where $s = \nabla n/2k_F n$,

κ = 0.804 and μ = 0.21951.

where the energies are also expressed in Hartree units.

2.6 LSDA + *U* method and GGA + *U* method

LDA and GGA are insufficient to describe the physical properties of strongly correlated materials. This is ascribed to the tendency of E_{XC} to over-delocalize the valence electrons and to over-stabilization of the metallic ground state. This over-delocalization attributed to E_{XC} is because it fails to cancel out the self-interaction contained in the Hartree term.

In order to overcome the above problem, the LDA plus Hubbard *U* method including *U* for each atomic orbital in the material is proposed.

$$E_{LDA+U} = E_{LDA} + \frac{1}{2}U\sum_{i\neq j} n_i n_j - \frac{UN(N-1)}{2}, \tag{2.6.1}$$

where n_i are d or f orbital occupancies and *N* is the number of d or f electrons.

$\frac{1}{2}U\sum_{i\neq j} n_i n_j$ is a Hubbard-type term (neglecting exchange parameters(*J*)).

The orbital energies are given by

$$\varepsilon_i = \frac{\partial E}{\partial n_i} = \varepsilon^{LDA} + U\left(\frac{1}{2} - n_i\right). \tag{2.6.2}$$

This formula gives the shift of the LDA orbital energy as $-U/2$ for occupied orbitals (n_i = 1) and $+U/2$ for unoccupied orbitals (n_i = 0)

Here we describe the LSDA plus Hubbard *U* (LSDA + *U*) method including *U* and *J* for each atomic orbital in the material. The LSDA + *U* functional[97,98] is expressed as

$$E_{LSDA+U} = E_{LSDA} + E_{HF}[n] - E_{dc}[n], \tag{2.6.3}$$

where E_{LSDA} is the total energy functional based on LSDA, E_{HF} is a term for electron-electron interactions to model correlated states and E_{dc} is the double-counting term.

$$E_{HF} = \frac{1}{2}\sum_{\{m\},\sigma}\left\{ < m,m'' \left| V_{ee} \right| m',m''' > \rho^{\sigma}_{mm'}\rho^{-\sigma}_{m''m'''} + \left(< m,m'' \left| V_{ee} \right| m',m''' > - < m,m'' \left| V_{ee} \right| m''',m' > \rho^{\sigma}_{mm'}\rho^{\sigma}_{m''m'''} \right) \right\},$$

(2.6.4)

$$E_{dc}[n]=\frac{U}{2}N(N-1)-\frac{J}{2}\left(N_{\downarrow}(N_{\downarrow}-1)+N_{\uparrow}(N_{\uparrow}-1)\right), \tag{2.6.5}$$

$$N_{\sigma}=\mathrm{Tr}\left(\boldsymbol{\rho}^{\sigma}_{\mathrm{mm}'}\right), \tag{2.6.6}$$

$$N=N_{\uparrow}+N_{\downarrow}, \tag{2.6.7}$$

where $\rho^{\sigma}_{m,m'}$ is the density matrix. The V_{ee} integral is the electron-electron interaction, which is expressed using the wavefunctions of the atomic states, labeled by the index m:

$$<m,m''|V_{ee}|m',m'''>=\iint d\mathbf{r}d\mathbf{r}'\varphi^{*}_{lm}(\mathbf{r})\varphi_{lm'}(\mathbf{r})\frac{\mathrm{e}^2}{|\mathbf{r}-\mathbf{r}'|}\varphi^{*}_{lm''}(\mathbf{r}')\varphi_{lm'''}(\mathbf{r}'). \tag{2.6.8}$$

Assuming that the atomic states are chosen on a localized basis, this integral can be factorized into radial and angular contributions. The matrix elements can be expressed in terms of complex spherical harmonics and effective Slater integrals F^k as

$$<m,m'|V_{ee}|m',m'''>=\sum_{k}a_k\left(m,m',m'',m'''\right)F^k, \tag{2.6.9}$$

where $0\le k\le 2l$ and

$$a_k\left(m,m',m'',m'''\right)=\frac{4\pi}{2k+1}\sum_{q=-k}^{k}<lm|Y_{kq}|lm'><lm''|Y^{*}_{kq}|lm'''>, \tag{2.6.10}$$

$$F^k=e^2\int dr\int dr'r^2r'^2R^2_{nl}(\mathbf{r})\frac{r^k_{<}}{r^{k+1}_{>}}R^2_{nl}(\mathbf{r}'), \tag{2.6.11}$$

where $R_{nl}(\mathbf{r})$ is the radial part of the atomic wavefunction and, $r_{<}$ and $r_{>}$ indicate the shorter and larger radial distance between r and r'.

In the case of $m=m$', and m''$=m$''',

$$E_{HF}=\frac{1}{2}\sum_{\sigma,\sigma}\left\{\sum_{m\neq m'}\left((U-J)\rho^{\sigma}_{mm}\rho^{\sigma}_{m'm'}\right)+\sum_{m,m',\sigma}U\rho^{\sigma}_{mm'}\rho^{-\sigma}_{m'm}\right\}. \tag{2.6.12}$$

For d orbitals,

$$U = \frac{1}{(2l+1)^2} \sum_{m,m'} < m.,m' \,|V_{ee}\,| \, m,m' > = F^0, \tag{2.6.13}$$

$$J = \frac{1}{2l(2l+1)} \sum_{m \neq m',m'} < m.,m' \,|V_{ee}\,| \, m',m > = \frac{F^2 + F^4}{14}. \tag{2.6.14}$$

The LSDA + *U* functional given by Dudarev et al.[99] is expressed as

$$E_{LSDA+U} = E_{LSDA} + \frac{(U-J)}{2} \sum_{\sigma} \left[\left(\sum_j \rho_{jj}^{\sigma} \right) - \left(\sum_{j,l} \rho_{jl}^{\sigma} \rho_{lj}^{\sigma} \right) \right], \tag{2.6.15}$$

The matrix of the one-electron potential is given by

$$V_{jl}^{\sigma} = \frac{\delta E_{LSDA+U}}{\delta \rho_{lj}^{\sigma}} = \frac{\delta E_{LSDA}}{\delta \rho_{lj}^{\sigma}} + (U-J) \left[\frac{1}{2} \delta_{jl} - \rho_{jl}^{\sigma} \right]. \tag{2.6.16}$$

The total energy is expressed in term of Kohn-Sham eigenvalues $\{\varepsilon_i\}$as

$$E_{LSDA+U} = E_{LSDA}[\{\varepsilon_i\}] + \frac{(U-J)}{2} \sum_{l,j,\sigma} \rho_{lj}^{\sigma} \rho_{jl}^{\sigma}, \tag{2.6.17}$$

where the last term represents the double counting correction.

The GGA plus Hubbard *U* (GGA + *U*) method including *U* and *J* for each atomic orbital in the material is also proposed. The GGA + *U* functional is expressed as

$$E_{GGA+U} = E_{GGA} + \frac{(U-J)}{2} \sum_{\sigma} \left[\left(\sum_j \rho_{jj}^{\sigma} \right) - \left(\sum_{j,l} \rho_{jl}^{\sigma} \rho_{lj}^{\sigma} \right) \right]. \tag{2.6.18}$$

Recently, attempts to estimate *U* and *J* have been made using various methods.[98] For example, *U* was calculated from the variation of the total energy *E* on changing the population of the localized states of a single atom by one electron.

$$U = E\left(\frac{n}{2}+1;\frac{n}{2}\right) - E\left(\frac{n}{2};\frac{n}{2}\right) - E\left(\frac{n}{2}+1;\frac{n}{2}-1\right) + E\left(\frac{n}{2};\frac{n}{2}-1\right), \tag{2.6.19}$$

where the two numbers in the parentheses represent the population of the two spin manifolds, and the original configuration is spin unpolarized with *n* electrons on the d

shell of each atom. Generally speaking, the above quantity is estimated from the difference between the 3d energy levels:

$$U = \tilde{\varepsilon}_{3d}\left(\frac{n}{2}+\frac{1}{2};\frac{n}{2}\right)-\tilde{\varepsilon}_{3d}\left(\frac{n}{2}+\frac{1}{2};\frac{n}{2}-1\right), \qquad (2.6.20)$$

where $\tilde{\varepsilon}_{3d}(x,y)=\varepsilon(x,y)-E_F(x,y)$ (E_F is the Fermi level). In the expression of equation (2.6.20), the screening from the other states is automatically included by letting their population reorganize when changing the number of electrons on d states.

Moreover, there are several studies to calculate *U* and *J* in thefollowing.

i) *U* and *J* are estimated by projecting unrestricted HF molecular orbitals onto atomic orbitals and retaining on-site terms from HF interactions, averaged over the states of the same atom. However, the obtained *U* and *J* are somewhat higher than those obtained from other methods.

ii) The effective screened *U* is evaluated by the constrained random approximation which is popular with DFT + dynamical mean field theory (DMFT). This method gives frequency-dependent interaction parameter.

However, the above methods are insufficient to adopt for real materials such as FeRh that consist of two kinds of transition metals including complex electronic correlations.

2.7 Projector augmented wave method

Various efficient methods have been developed to calculate the one-particle Schrödinger equation for the LDA. The widely used methods are divided into two groups. One group contains all-electron methods, such as the linear augmented-plane-wave method[100]. The other group contains pseudopotential methods. In the latter, valence electron states are only taken into account while core electron states are eliminated. For example, representative pseudopotentials are norm-conserving pseudopotentials[101] and ultrasoft pseudopotentials.[102] In recent

years, the projector augmented wave (PAW) method, which is a generalization of the pseudopotential method and the linear augmented-plane-wave method,[103,104] has often been used. We present details of this method in the following.

The wavefuctions of materials have different features in different regions of space. Near the nucleus, the wavefunction oscillates rapidly due to the large attractive potential of the nucleus. In the bonding region, it is smooth. Therefore, it is very difficult to deal with the electronic structure in the bonding region while trying to accurately render the wavefunction in the vicinity of the nucleus. The scheme of the augmented wave method is to divide the wavefunction into two parts, i. e., a partial wave function within an atom-centered sphere and an envelope function outside the sphere. The envelope function is expanded by the plane wave. The envelope function and the partial wave expansions are then matched in value and derivative at the boundary of the sphere. Using PAW, rapidly oscillating valence wavefunctions near ion cores can be transformed into smooth ones. The all-electron properties can be calculated from these smooth wavefunctions. The all-electron wavefunction $|\Psi>$ can be obtained from the pseudo wavefunction $|\tilde{\Psi}>$, the all-electron partial waves (φ_i), the pseudo partial waves ($\tilde{\varphi}_i$) and the projector functions ($\tilde{p}_i$).

(i) $|\Psi>$ is equal to $|\tilde{\Psi}>$ outside some augmentation region Ω near the ion cores .

$$|\Psi>=|\tilde{\Psi}> \quad \text{outside} \quad \Omega, \tag{2.7.1}$$

(ii) $|\Psi>$ and $|\tilde{\Psi}>$ are different within Ω.

$$|\tilde{\Psi}>=\sum_i |\tilde{\varphi}_i> c_i \quad \text{within} \quad \Omega, \tag{2.7.2}$$

$$|\Psi>=\sum_i |\varphi_i> c_i \quad \text{within} \quad \Omega, \tag{2.7.3}$$

$$c_i =< \tilde{p}_i |\tilde{\Psi}>. \tag{2.7.4}$$

In summary, $|\Psi>$ can be given by

$$|\Psi> = |\tilde{\Psi}> + \sum_i \left(|\varphi_i> - |\tilde{\varphi}_i> \right) < \tilde{p}_i | \tilde{\Psi}> . \qquad (2.7.5)$$

$$< \tilde{p}_i | \tilde{\varphi}_j > = \delta_{ij} . \qquad (2.7.6)$$

The all-electron wavefunction $|\Psi>$ can be built as shown in Fig. 8.

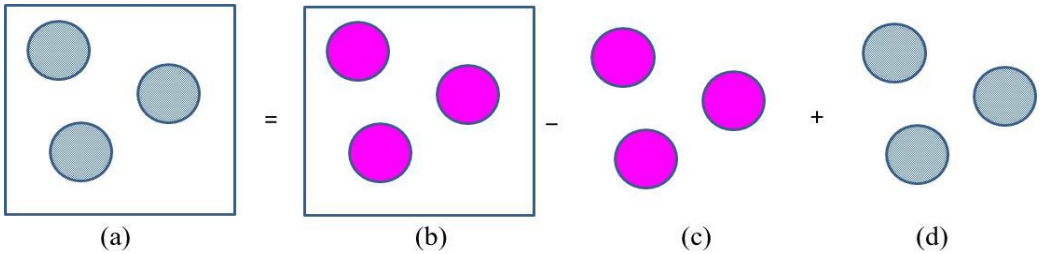

Fig. 8. Character of the wavefunction. (a) all-electron wavefunction $|\Psi>$, (b) pseudo wavefunction $|\tilde{\Psi}>$, (c) $\sum_i |\tilde{\varphi}_i> < \tilde{p}_i | \tilde{\Psi}>$ and (d) $\sum_i |\varphi_i> < \tilde{p}_i | \tilde{\Psi}>$.

2.7.1 Charge density

Using the PAW method, the all-electron charge density is given by

$$n(\mathbf{r}) = \tilde{n}(\mathbf{r}) + n^1(\mathbf{r}) - \tilde{n}^1(\mathbf{r}) . \qquad (2.7.7)$$

The soft pseudo charge density $\tilde{n}(\mathbf{r})$ is the expectation value for the real space projection operator $|\mathbf{r}><\mathbf{r}|$ operating on the pseudo wavefunction:

$$\tilde{n}(\mathbf{r}) = \sum_n f_n < \tilde{\Psi}_n | \mathbf{r} >< \mathbf{r} | \tilde{\Psi}_n > . \qquad (2.7.8)$$

where n is the band index and f_n denotes the occupancy of the state.

The on-site charge densities $n^1(\mathbf{r})$ and $\tilde{n}^1(\mathbf{r})$ are treated on a radial support grid.

$$n^1(\mathbf{r}) = \sum_{(i,j)} \rho_{ij} < \varphi_i | \mathbf{r} >< \mathbf{r} | \varphi_j > , \qquad (2.7.9)$$

and

$$\tilde{n}^1(\mathbf{r}) = \sum_{(i,j)} \rho_{ij} < \tilde{\varphi}_i | \mathbf{r} >< \mathbf{r} | \tilde{\varphi}_j > , \qquad (2.7.10)$$

where ρ_{ij} are the occupancies of each augmentation channel (i, j) and are calculated from the pseudo wavefunction applying the projector functions:

$$\rho_{ij} = \sum_n f_n < \tilde{\Psi}_n | \overline{p_i} >< \overline{p}_j | \tilde{\Psi}_n > . \qquad (2.7.11)$$

We concentrate on the frozen core case. In addition, we introduce four quantities that will be used to describe the core charge density: n_c, $\tilde{n}_c$, $n_{Zc}, \tilde{n}_{Zc}$. n_c is the charge density of the frozen core all-electron wavefunction in the reference atom. The partial electronic core density $\tilde{n}_c$ is equivalent to the frozen core all-electron charge density outside a certain radius r_{pc}. r_{pc} lies inside the augmentation region.

n_{Zc} is the point charge density of the nuclei n_Z plus the frozen core all-electron charge density n_c:

$$n_{Zc} = n_Z + n_c . \qquad (2.7.12)$$

The pseudized core density $\tilde{n}_{Zc}$ is a charge distribution that is equivalent to n_{Zc} outside the core radius and has the same moment as n_{Zc} inside the core region:

$$\int_{\Omega_r} n_{Zc}(\mathbf{r}) d^3\mathbf{r} = \int_{\Omega_r} \tilde{n}_{Zc}(\mathbf{r}) d^3\mathbf{r} , \qquad (2.7.13)$$

where $\int_{\Omega_r}$ represents integration over the radial support grid. The total moment of n_{Zc} and $\tilde{n}_{Zc}$ is equivalent to the ionic net charge $-Z_{\text{ion}}$.

The total charge density n_T is decomposed into three terms:

$$n_T = n + n_{Zc} = (\tilde{n} + \hat{n} + \tilde{n}_{Zc}) +$$

$$(n^1 + n_{Zc}) - (\tilde{n}^1 + \hat{n} + \tilde{n}_{Zc})$$

$$= \tilde{n}_T + n_T^1 - \tilde{n}_T^1 . \qquad (2.7.14)$$

The crucial step is the introduction of a compensation charge $\hat{n}$, which is added to the soft charge densities $\tilde{n} + \tilde{n}_{Zc}$ and $\tilde{n}^1 + \tilde{n}_{Zc}$ in order to reproduce the correct multipole moments of the all-electron charge density $n^1 + n_{Zc}$ located in each augmentation region. Because n_{Zc} and $\tilde{n}_{Zc}$ have exactly the same monopole (-Z_{ion}) and vanishing multipoles, $\hat{n}$ must be chosen so that $\tilde{n}^1 + \hat{n}$ has the same moment as the all-electron valence charge density n^1 within each sphere.

2.7.2 Total energy

The expression for the total energy is given by

$$E = \tilde{E} + E^1 - \tilde{E}^1, \qquad (2.7.15)$$

$$\tilde{E} = \sum_n f_n < \tilde{\Psi}_n | -\frac{1}{2}\Delta | \tilde{\Psi}_n > + E_{XC}[\tilde{n} + \hat{n} + \tilde{n}_c] + E_H[\tilde{n} + \hat{n}] +$$
$$\int_{\Omega_R} v_H[\tilde{n}_{Zc}][\tilde{n}(\mathbf{r}) + \hat{n}(\mathbf{r})]dr + U(\mathbf{R}, Z_{ion}), \qquad (2.7.16)$$

$$\tilde{E}^1 = \sum_{i,j} \rho_{ij} < \tilde{\varphi}_i | -\frac{1}{2}\Delta | \tilde{\varphi}_j > + \overline{E_{XC}(\tilde{n}^1 + \hat{n} + \tilde{n}_c)} + \overline{E_H(\tilde{n}^1 + \hat{n})} + \int_{\Omega_R} v_H[\tilde{n}_{Zc}][\tilde{n}^1(\mathbf{r}) + \hat{n}(\mathbf{r})]d\mathbf{r},$$

(2.7.17)

$$E^1 = \sum_{i,j} \rho_{ij} < \varphi_i | -\frac{1}{2}\Delta | \varphi_j > + \overline{E_{XC}(n^1 + n_c)} + \overline{E_H(n^1)} + \int_{\Omega_R} v_H[n_{Zc}] n^1(\mathbf{r}) d\mathbf{r} ,$$

(2.7.18)

where the overbar signifies that the corresponding quantity is evaluated on the radial grid within the augmentation region.

v_H is the electrostatic potential of the charge density n:

$$v_H[n](\mathbf{r}) = e^2 \int \frac{n(\mathbf{r}')}{|\mathbf{r} - \mathbf{r}'|} d\mathbf{r}' , \qquad (2.7.19)$$

and $E_H[n]$ is its electrostatic energy, which is given by

$$E_H[n] = \frac{1}{2} e^2 \int d\mathbf{r} \int \frac{n(\mathbf{r}) n(\mathbf{r}')}{|\mathbf{r} - \mathbf{r}'|} d\mathbf{r}' . \qquad (2.7.20)$$

$U(\mathbf{R}, Z_{ion})$ is the electronic energy of the point charges Z_{ion} in the uniform electronic background (an Ewald summation). $\tilde{E}$ is evaluated on a regular grid. E^1 and $\tilde{E}^1$ are evaluated for each sphere individually on a radial support grid.

2.8 Algorithms for calculating the ground-state energy

Various algorithms are used in simulation programs using first principles calculations. Especially, we think that the calculation of the Kohn and Sham ground state is important. Thus, as an example, the calculation flow of this state using the Vienna ab initio simulation package (VASP)[105,106] shown in Fig.9 is explained in the following.

(i) At the beginning of the calculation, a reasonable trial charge ρ_{in} and a trial wave vector ϕ_n are chosen.

(ii) Energies necessary to set up the Hamiltonian, such as the Hartree energy and the

exchange–correlation energy mentioned in section 2.3-2.7 are calculated from the input charge density.

(iii) The Hamiltonian spanned by the trial wavefunctions is diagonalized. A unitary transformation of the wavefunctions ϕ_n is performed, so that the Hamiltonian is diagonal in the subspace spanned by the transformed wavefunctions. This step is sub-space diagonalization:

$$< \phi_j \mid \hat{H} \mid \phi_i >= H_{ij}, \tag{2.8.1}$$

$$H_{ij} U_{jk} = \varepsilon_k U_{ik}, \tag{2.8.2}$$

$$\phi_j \leftarrow U_{jk} \phi_k. \tag{2.8.3}$$

The above diagonalization can be performed before or after the conjugate gradient or the residual minimization scheme. All the iterative algorithms are very similar. The core quantity is the residual vector R_n

$$| R_n >= \left(\hat{H} - E\right) | \phi_n > \quad \text{with} \quad E = \frac{< \phi_n \mid \hat{H} \mid \phi_n >}{< \phi_n \mid \phi_n >}. \tag{2.8.4}$$

R_n is added to ϕ_n.

(iv) The total energy of the system is calculated.

(v) From the optimized wavefunctions, a new charge density mixed with the old input-charge density (Broyden/Pulay mixing scheme) is calculated.

(vi) A judgment is made as to whether the magnitude of the total energy converges or not. When not converging, the above calculation is repeated until the magnitude of the energy converges.

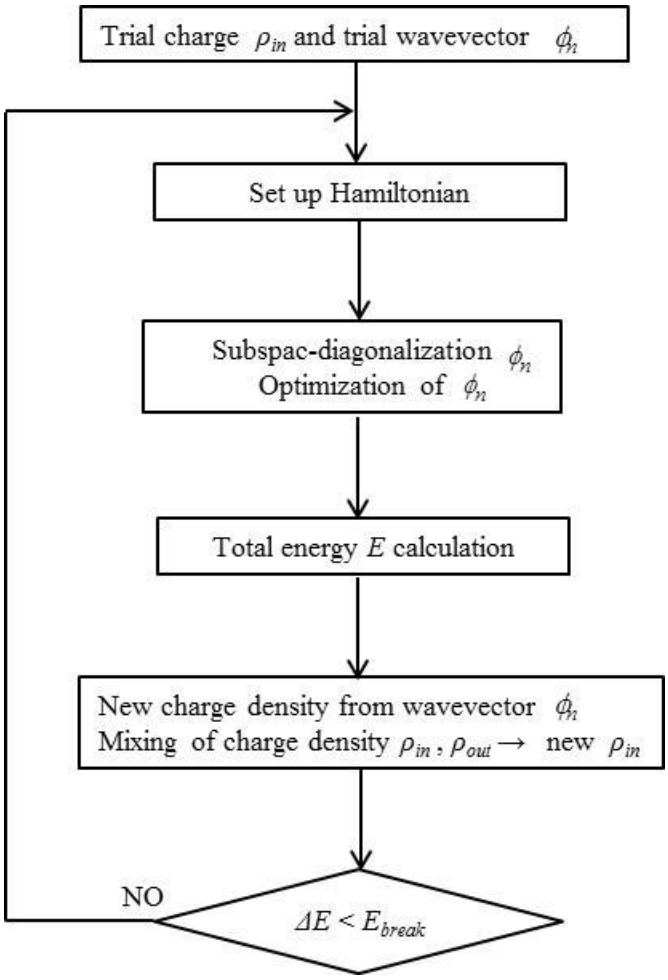

Fig. 9. Calculation flow of Kohn and Sham ground state.

Chapter 3

Method used to calculate the electronic and magnetic structures

3.1 Model

The magnetic structures in the AFM and FM states of FeRh, which has a simple cubic structure like the CsCl crystal lattice, are shown in Fig. 10. With increasing temperature, bulk FeRh undergoes a rapid isotropic lattice expansion and becomes FM for temperatures $T_{tr} < T < T_C$. The magnetic anisotropy in bulk FeRh is small because the spin-orbit coupling is weak (however, thin films of FeRh exhibit an in-plane easy axis of magnetization with no measureable magnetocrystalline anisotropy).[32] The direction of the magnetic moment is chosen as the *c* axis. The Fe_2Rh_2 model is used in order to treat FeRh in both the AFM and FM states. The lattice structure of the crystal is considered to be face centered cubic (FCC) with lattice constant $a' = 2a$, where a is the lattice constant in the case of a simple cubic structure. The atomic positions of the two Fe atoms are (0.0, 0.0, 0.0) and (0.5a', 0.5 a', 0.5 a'). The atomic positions of the two Rh atoms are (0.25 a', 0.25 a', 0.25 a') and (0.75 a', 0.75 a', 0.75 a'). The magnetic spin states at the 2 atomic positions of (0.0, 0.0, 0.0) and (0.5a', 0.5 a', 0.5 a') in the AFM state are ↑ and ↓ (↑ signifies that the spin is up and ↓ that it is down), respectively, while in the FM state they are both ↑. The initial magnitudes of the spin states are $3.0\mu_B$. The initial magnitude of the magnetic moments at the 2 atomic positions of Rh is $0\mu_B$.

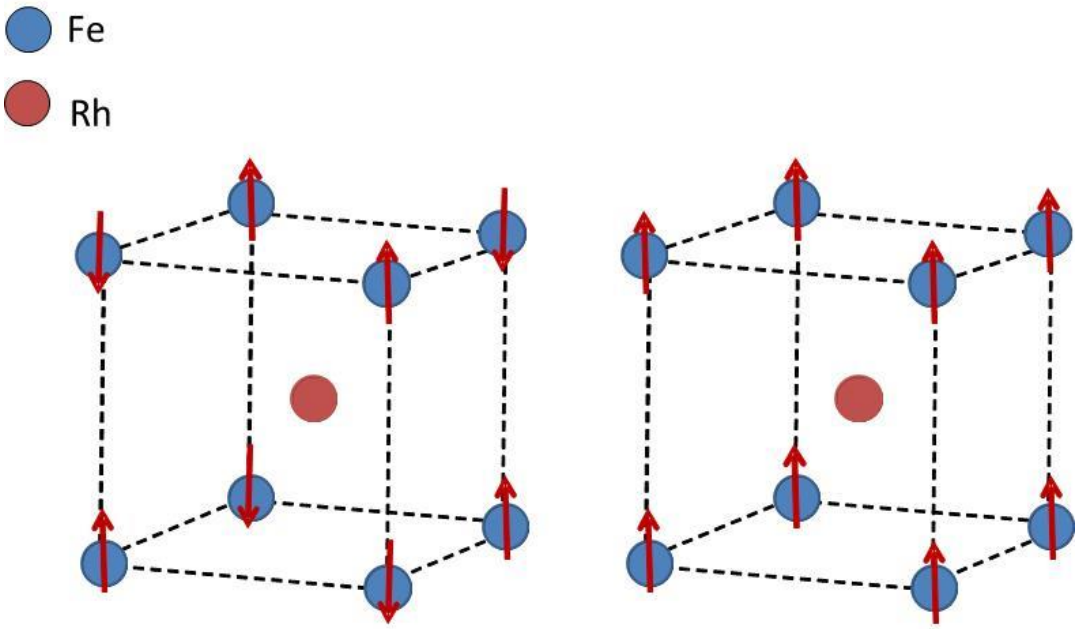

Fig. 10. Magnetic structure of the (a) AFM and (b) FM states of FeRh. The blue and violet circles indicate Fe and Rh atoms, respectively. ↑ and ↓ indicate the directions of the magnetic moments.

In the present work, the lattice constant *a* is varied between 2.8 and 3.2 Å which encompass the actual observed values.

3.2 Method and calculation conditions

Calculations were done using the following methods and conditions.

i) VASP, mentioned in section 2.8, was utilized for performing first principles calculations.

ii) The PAW method, mentioned in section 2.7, was used.

iii) The GGA + *U* method with the PBE exchange-correlation functional including *U* and *J* for each atomic orbital in the material, mentioned in section 2.6, was used, because the results of our GGA calculations, such as ΔE (= 31.5 meV/atom) and

the magnitude of the relationship between the Fe magnetic moments of the AFM and FM states ($3.12\mu_B$, $3.18\mu_B$) were inconsistent with experimental results. In the calculations, the Dudarev approach, which depends only on $U_{eff} = U - J$, was adopted. U for the Fe_{3d} electrons (U_{Fe}) and U for the Rh_{4d} electrons (U_{Rh}) were 2.0 eV and 1.95 eV, respectively In general, J for Fe_{3d} electrons (J_{Fe}) is from 0.8 to 0.9 eV,[107,108,109] whereas J for Rh_{4d} electrons (J_{Rh}) is around 0.6 eV.[110,111] These values are different in the reported calculations. For both the Fe_{3d} and Rh_{4d} electrons, the values of J_{Fe} and J_{Rh} were set to 1.0 eV for simplicity.

iv) A plane-wave basis set was used.

From Bloch's theorem, the solutions of Schrödinger equation for a computational cell is of the form

$$\varphi_k(\mathbf{r}) = e^{ikr} u_k(\mathbf{r}). \qquad (3.2.1)$$

where $u_k(\mathbf{r})$ is a periodic function. By the plane wave expansion, we obtain

$$u_k(\mathbf{r}) = \sum_G c_{\mathbf{G}} e^{\mathbf{iGr}}, \qquad (3.2.2)$$

where the summation is over all of the reciprocal lattice vectors **G**. Substituting (3.2.2) for (3.2.1) leads to

$$\phi_k(\mathbf{r}) = \sum_G c_{\mathbf{k+G}} e^{i(\mathbf{k+G})\mathbf{r}}. \qquad (3.2.3)$$

The plane wave $e^{i(\mathbf{k+G})\mathbf{r}}$ is the solution to the free electron Schrödinger equation with the energy

$$E = \frac{\hbar^2}{2m}|\mathbf{k}+\mathbf{G}|^2. \qquad (3.2.4)$$

The summation is made over the reciprocal lattice vectors with energies less than a cut-off energy E_{cut}.

$$E_{cut} = \frac{\hbar^2}{2m} G_{cut}^2 . \qquad (3.2.5)$$

Equation (3.2.3) becomes

$$\phi_k(\mathbf{r}) = \sum_{|k+G|<G_{cut}} c_{\mathbf{k}+\mathbf{G}} e^{i(\mathbf{k}+\mathbf{G})\mathbf{r}} . \qquad (3.2.6)$$

The cutoff energy (E_{cut}) used was 830 eV.

v) An 11×11×11 Monkhorst-Pack k-mesh was used for the Brillouin zone integration [112].

The construction rule for Monkhorst-Pack is

$$\mathbf{k}_{i,j,k} = u_i \mathbf{b}_1 + u_j \mathbf{b}_2 + u_k \mathbf{b}_3, \qquad (3.2.7)$$

$$u_i \frac{2r - N_i - 1}{2N_i}, \qquad r=1, 2, \ldots..\mathrm{N_i}, \qquad (3.2.8)$$

where $\mathbf{b}_1$, $\mathbf{b}_2$ and $\mathbf{b}_3$ are the reciprocal lattice vectors, and N_i is the number of the subdivision which determines the number of k points in the i direction.

vi) The convergence condition for the electronic self-consistent loops was 10^{-7} eV.

vii) The method of Methfessel-Paxton of order N[113] was adopted in order to calculate the density of states consistent with the experiments.

Using this method, the DOS of real metallic materials can be obtained by multiplying it by the following step function $S(x)$. It is given by

$$S_N(x) = 1 - \int_{-\infty}^{x} D_N(t) dt , \qquad (3.2.9)$$

where $D_N(x) = \sum_{n=0}^{N} A_n H_{2n}(x) e^{-x^2}$, and H_{n} is the Hermite polynomial. From (3.2.9), the following results are obtained.

$$S_0(x) = \frac{1}{2}(1 - erf(x)), \qquad (3.2.10)$$

$$S_N(x) = S_0(x) + \sum_{n=1}^{N} A_n H_{2n-1}(x) e^{-x^2}, \quad (3.2.11)$$

with

$$x = \frac{\varepsilon - E_F}{\Delta\sigma}, \quad (3.2.12)$$

where *erf*(*x*) is the error function, ε is the energy, and $\Delta\sigma$ is the width of the smearing. In the present work, N=1 and $\Delta\sigma$= 0.05 eV were chosen.

3.3 Validation of calculation parameters

3.3.1 Fe and Rh crystals

In order to validate our choices of U and J, first principles calculations of Fe and Rh crystals using U_{Fe} = 2 eV and J_{Fe} = 1.0 eV, and U_{Rh} = 1.95 eV and J_{Rh} = 1.0 eV were performed (U_{eff} for an Fe atom (= $U_{Fe} - J_{Fe}$) is almost equal to U_{eff} for an Rh atom (= $U_{Rh} - J_{Rh}$) according to Ref.114).

The electronic and magnetic structures of the Fe crystal are detailed. Fe crystals have various structures such as body-centered cubic (BCC), FCC, and hexagonal close packed structures. The electronic configuration for the isolated atom is $3d^6 4s^2\ {}^5D_4$.[115] In the present work, a FM BCC structure was chosen. The obtained physical quantities of the Fe crystal, such as a_{FM}, B_{FM} and E_{YFM} (refer to equations (3.3.1) and (3.3.2) with respect to the calculation method), and experimental values[116,117,118] are listed in Table I, which shows that the calculated physical quantities are consistent with the experimental ones.

The DOS of a FM BCC Fe crystal in the case of U_{Fe} = 2.0 eV for the obtained stable a_{FM} (=2.88 Å, which is consistent with the experimental value from Ref. 116 (2.87 Å)), is shown in Fig. 11(a), and the DOS for the majority and minority spin states are shown in Fig. 11(b), both of which are consistent with the spectra given in

experimental reports.[120,121,122] The positions of the four peaks of the obtained DOS below E_F are around –0.5 eV, –1.2 eV, –3.4 eV, and –4.2 eV, respectively. From Fig. 11(b), since the DOS below E_F of the majority spin band moves to a lower position than that of the reported calculations without taking into account U[123, 124, 125], the magnitude of the obtained m_{Fe} is 2.64 μ_B and is larger than the experimental value of 2.22 μ_B.[119] Nevertheless, it is similar to that of the reported calculation[126] using the LSDA + U method. However, the obtained shape and width of the DOS near E_F shown in Fig. 11(a) is consistent with the above reported calculations.

The electronic and magnetic structures of the Rh crystal are detailed. The electronic configuration for the isolated atom is $4d^8 5s^1\ {}^4F_{9/2}$.[115] Here, the FCC structure was chosen. The obtained physical quantities of the Rh crystal, such as a_{PM}, B_{PM} and E_{YPM}, and the experimental values[127,128,129] are listed in Table II, which shows that the physical quantities are consistent with the experimental ones.

The DOS of the PM FCC Rh crystal with U_{Rh} = 1.95 eV (U_{eff} = 0.95 eV is a reasonable value because the nonmagnetic state of the Rh crystal is stable in the case of $U_{eff} = U_{Rh} - J \leq 1.0$ eV[111]) is shown in Fig. 11(c) for the obtained stable a_{PM} (=3.81 Å, which is in good agreement with the experimentally reported value of 3.80 Å), and is consistent with the spectra obtained by experiment [131-134] and those given in reports of calculations for the Rh crystal[135, 136] in which U is not taken into account. The DOS below E_F obtained which covers the region from -6 eV to 0 eV is consistent with the experimental reports and reported calculations. The magnetization of the Rh crystal is 0μ_B. This is consistent with the fact that the Rh magnetic moments in the case of the PM state are randomly distributed.[130]

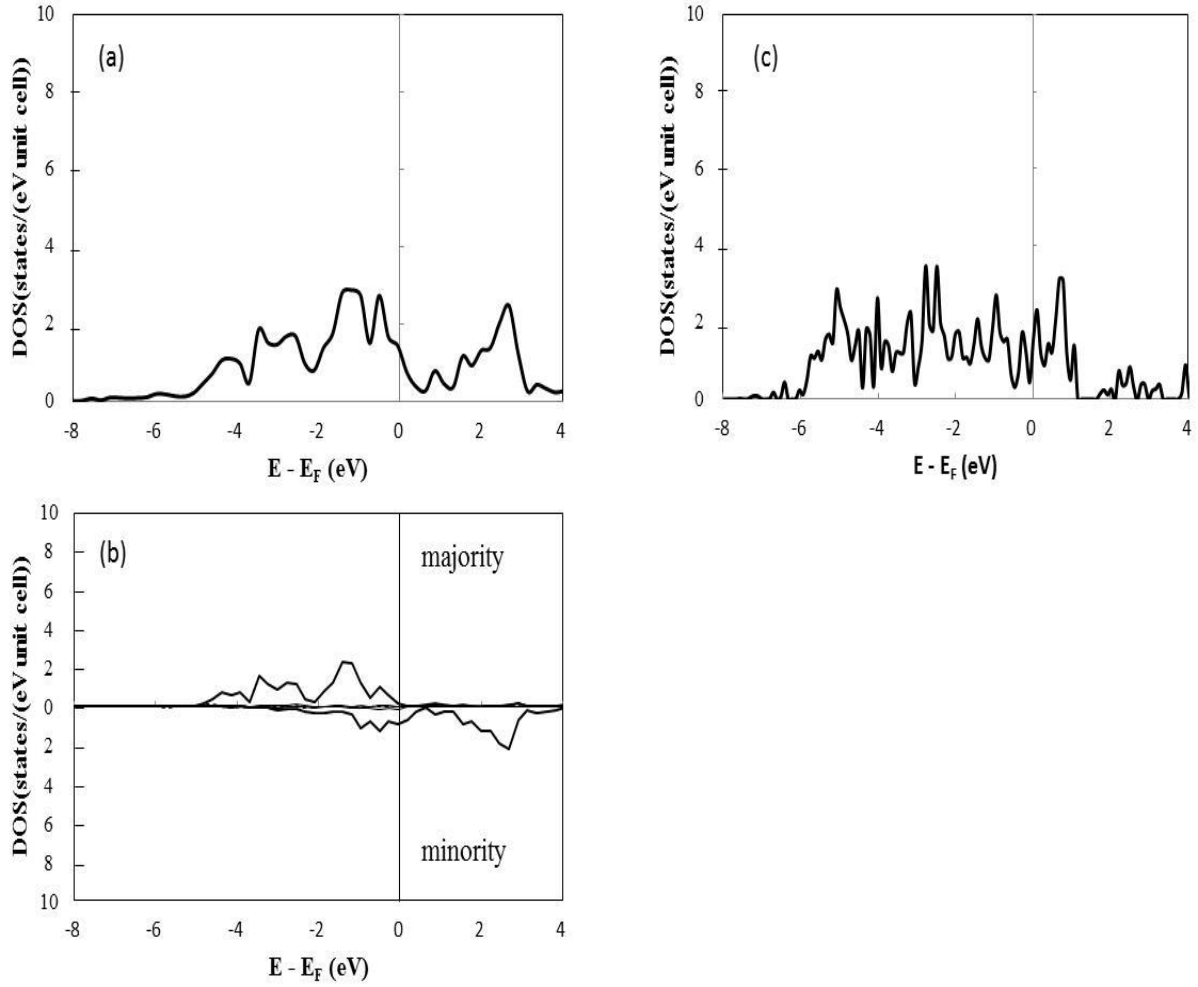

Fig. 11. (a) DOS of an Fe crystal in the FM state where U_{Fe} = 2.0 eV, (b) for the majority and minority spin states, and (c) of a Rh crystal in the PM state where U_{Rh} = 1.95 eV using the GGA + U method.

Table I. Comparison between the results obtained in this work and experimental results for an Fe crystal.

	a_{FM}	B_{FM}	E_{YFM}	m_{Fe}
	Å	GPa	GPa	μ_B
Present work	2.88	171	221	2.6
Ref.116	2.87			
Ref.117		168		
Ref.118			210	
Ref.119				2.22

Table II. Comparison between the results obtained and experimental results for a Rh crystal.

	a_{PM}	B_{PM}	E_{YPM}	Magnetization
	Å	GPa	GPa	μ_B
Present work	3.81	263	385	0
Ref.127	3.80			
Ref. 128		267		
Ref. 129			384	
Ref. 130				0

3.3.2 FeRh crystal

In order to validate the choice of *U*, the effect, in detail, of the magnitude of the relationship between *U* and *J* on the electronic and magnetic structures of FeRh is discussed in A.1.1. Moreover, a comparison between the results of calculations using the GGA + *U* method with U_{Fe} = 2.0 eV and those with U_{Fe} = 1.0 eV and 4.0 eV are

discussed in A.2. Comparisons between the values of U_{Fe} and U_{Rh} used in the present work and those used in other reports are made in A.3. We also used LSDA +U. The results of calculations using this are discussed in A.1.2.

We validated our choices of E_{cut}, the size of the k-mesh used for the Brillouin zone integration and the convergence condition as follows.

(i) ΔE obtained with E_{cut} = 830 eV was compared with that obtained with E_{cut} = 680 eV. The difference of ΔE between the two conditions was less than 0.01 meV.

(ii) ΔE obtained with an 11×11×11 k-mesh used for the Brillouin zone integration was compared with that obtained with a 15×15×15 k-mesh. The difference in ΔE between these two conditions was about 0.1 meV.

(iii) ΔE obtained with the convergence condition 10^{-7} eV was compared with that obtained with the convergence condition 10^{-9} eV. The difference of ΔE between these two conditions was less than 0.001 meV.

The bulk modulus and Young's modulus were investigated in order to validate our choice of U and J (U_{Fe} = 2.0 eV and J_{Fe} = 1.0 eV, and U_{Rh} = 1.95 eV and J_{Rh} = 1.0 eV).

B_{AFM} and B_{FM} were calculated using a formula reported in the literature.[137] Comparisons between the obtained B_{AFM} and B_{FM}, and those given in experimental reports are listed in Table III. The obtained B_{FM} is larger than B_{AFM}.

$$B = V_0 \frac{\partial^2 E}{\partial V^2}, \tag{3.3.1}$$

where B is the bulk modulus, V and V_0 are the atomic volume and the equilibrium atomic volume, respectively and $\frac{\partial^2 E}{\partial V^2}$ is the second derivative of the total energy with respect to V. B_{FM} and B_{AFM} were investigated and the following results were obtained. The value of B_{FM} (= 210.6 GPa) is larger than that of B_{AFM} (= 195.7 GPa), and the difference between B_{FM} and B_{AFM} is 14 GPa, which is consistent with the experimental value reported (B_{FM} - B_{AFM} = 16 GPa).[58]

Table III. Comparisons between the values of B_{AFM}, B_{FM}, E_{YAFM} and E_{YFM} used in the present work and those in experimental reports.

	AFM		FM	
	B_{AFM}	E_{YAFM}	B_{FM}	E_{YFM}
	GPa	GPa	GPa	GPa
Present work	195.7	232	210.6	251
Ref. 24	142±14	153±14	133±20	197±25
Ref. 43		245		260
Ref. 58	142	170	158	190

E_{YAFM} and E_{YFM} were calculated using the following formula.[138)]

$$E = \frac{1}{V} \times \frac{\partial^2 E}{\partial e^2} \quad \text{at } V_{0,} \tag{3.3.2}$$

where E is Young's modulus, V and V_0 are the atomic volume and the equilibrium atomic volume, respectively, and $\frac{\partial^2 E}{\partial e^2}$ is the second derivative of the total energy with respect to the strain e. Comparisons between the obtained E_{YAFM} and E_{YFM}, and those given in experimental reports are listed in Table III. The results obtained are consistent with the experimental reports[24,43,58)] (the Young modulus increases near T_{tr} when changing from the AFM to FM state).

From the results obtained for the changes in the bulk modulus and Young's modulus when changing from the AF to FM phase, it was found that they largely increase. That is to say, stiffening of the material occurs. In the experimental reports, except for Ref. 24, this stiffening with the AF to FM phase transition has not been given due attention. We think that this stiffening is important in order to fully understand the origin of the AFM-FM phase transition.

The above results confirm the validity of our choices of U and J. Therefore, we think that it is appropriate to calculate other physical quantities of FeRh using these values of U and J. The results obtained are shown in the next section.

Chapter 4

Results of calculations and discussion

4.1 ΔE and the lattice constant

The relationship between the total energies of the AFM and FM states and the lattice constant (in the case of the PM state, the results of calculations are discussed in A.5) is investigated by choosing appropriate values of U_{Fe} and U_{Rh} to estimate ΔE. The relationship obtained in the case of U_{Fe} = 2.0 eV and U_{Rh} = 1.95 eV is shown in Fig. 12. A comparison between the values of a_{AFM} and a_{FM} obtained here and those in experimental reports are listed in Table IV. A comparison between the the value of ΔE obtained here and that in an experimental report is given in Table V. When the lattice constant is small, the AFM state is stable. The total energy of the AFM state has a minimum at a_{AFM} = 2.99 Å (strictly speaking, 2.992 Å) and the total energy difference between the AFM and FM states becomes smaller with increasing lattice constant. The total energy of the FM state has a minimum at a_{FM} = 3.01 Å (strictly speaking, 3.008 Å). The FM state becomes stable as the lattice constant increases above 3.01 Å. The values for a_{AFM} and a_{FM} obtained are consistent with experiment (a_{AFM} = 2.981 Å and a_{FM} = 2.999 Å).[22)] It is noted that the value obtained for ΔE (= 2.71 meV/atom) is consistent with the experimental value (= 2.80 meV/atom, which was estimated from the latent heat obtained using the difference, ΔS, between AFM and FM samples and the enthalpy difference obtained using the difference in specific heat capacity between them).[24)]

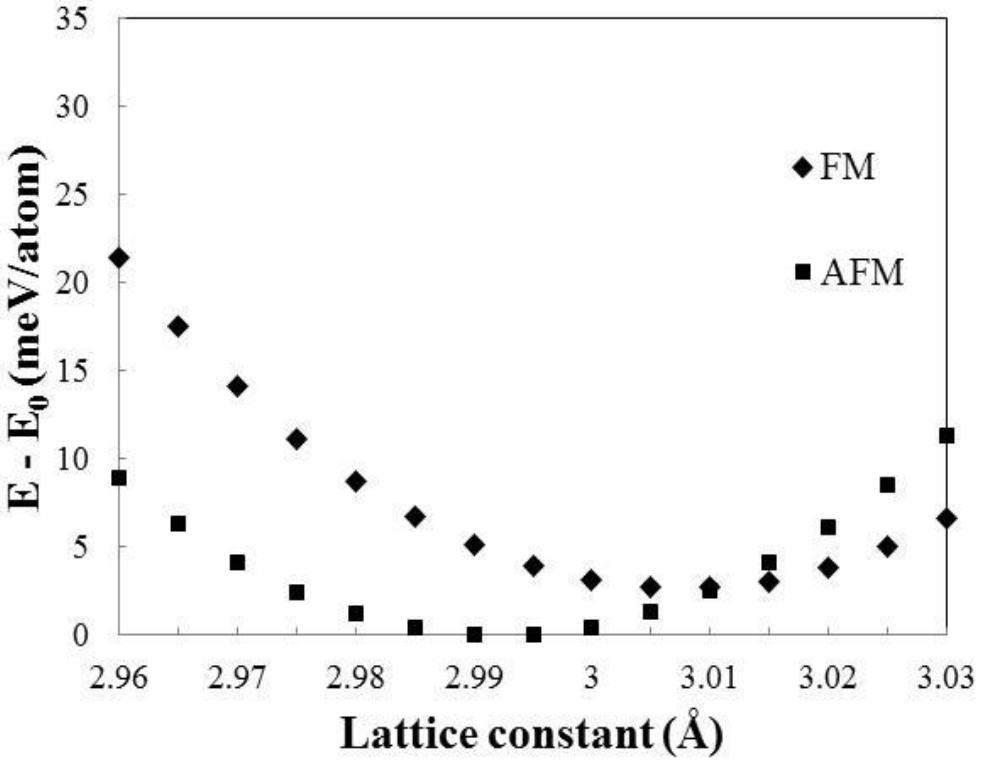

Fig. 12. Total energy versus the lattice constant. The minimum of the AFM state is set to zero. The closed squares and the diamonds show the total energies of the AFM and FM states, respectively.

Table IV. Comparison between the values of a_{AFM} and a_{FM} used in this work and reported experimentally measured values.

	AFM	FM
	a_{AFM}	a_{FM}
	Å	Å
Present work	2.99	3.01
Ref. 22	2.981	2.999
Ref. 23	2.987	2.997

Table V. Comparisons between the values of ΔE and the strength of $H_c(0)$ used here and those given in experimental reports.

	ΔE	$H_c(0)$
	meV	T
Present work	2.71	21.6
Ref. 24	2.80	
Ref. 28		23.4
Ref. 29		29.7
Ref. 30		21.2

4.2 Magnetization

The magnetic moment **m** is given by

$$\mathbf{m} = \mu_B(\mathbf{L} + g\mathbf{S}), \qquad (4.2.1)$$

where μ_B is the Bohr magneton, g is the gyromagnetic ratio, which is about 2, **L** is the orbital angular momentum and **S** is the spin angular momentum. In general, **L** is zero in 3d metals and 3d metal alloys due to the quenching of **L**.[139] Similarly, **L** is near zero in 4d metals. Therefore, we assume that this quenching occurs in FeRh, so that **m** = $2\mathbf{S}\mu_B$. Because **S** = (0, 0, S_z) in the present work, $m = 2S\mu_B$.

The other physical quantities obtained are given below. We consider the magnetic moments, m_{Fe} and m_{Rh}, of FeRh in the AFM and FM states. A comparison between the values of m_{Fe} and m_{Rh} in the AFM and FM states and those in an experimental report are given in Table VI. The magnetic moments obtained in this work are almost identical to those measured in the experiment.[26] The value of m_{Fe} in the AFM state (= $3.31\mu_B$) is equal to that of m_{Fe} in the FM state (= $3.31\mu_B$), which is slightly different to the result obtained from the experiment (m_{Fe} of the AFM state > m_{Fe} of the FM state).

Table VI. Comparison between the magnitude of m_{Fe} and m_{Rh} obtained in the present work and those in an experimental report.

	AFM		FM	
	m_{Fe}	m_{Rh}	m_{Fe}	m_{Rh}
	μ_B	μ_B	μ_B	μ_B
Present work	3.31	0	3.31	1.04
Ref. 26	3.30	0	3.17	0.97

Reports of the calculations of m_{Fe} are listed in Table VII, which shows that, in every case, and in contrast to the experimental report, m_{Fe} of FeRh in the AFM state

< m_{Fe} of FeRh in the FM state. However, in the present work, the relationship between the obtained m_{Fe} values of the AFM and FM states approaches that of the experiment.

Table VII. Summary of the calculated values of m_{Fe} and m_{Rh} of FeRh in the AFM and FM states published in various reports.

	AFM		FM	
	m_{Fe} μ_B	m_{Rh} μ_B	m_{Fe} μ_B	m_{Rh} μ_B
Ref. 65	2.98	0	3.15	1.02
Ref. 70	3.13	0	3.20	1.02
Ref. 73	3.18	0	3.23	1.0
Ref. 74	3.28	0	3.31	1.02
Ref. 77	3.07	0	3.13	1.04
Ref. 78	2.99	0	3.11	1.07
Ref. 83	3.11	0	3.22	1.03
Ref. 84	2.96	0	3.02	1.18

The relationships between m_{Fe} and m_{Rh} in the AFM and FM states and the lattice constant were calculated and these are shown in Fig. 13. With increasing lattice constant,

(i) the change in m_{Fe} is much larger than that in m_{Rh},

(ii) the change in m_{Fe} in the AFM state is larger than that in the FM state, and

(iii) the magnitude relation of m_{Fe} values between the AFM and FM states is reversed near the observed lattice constant.

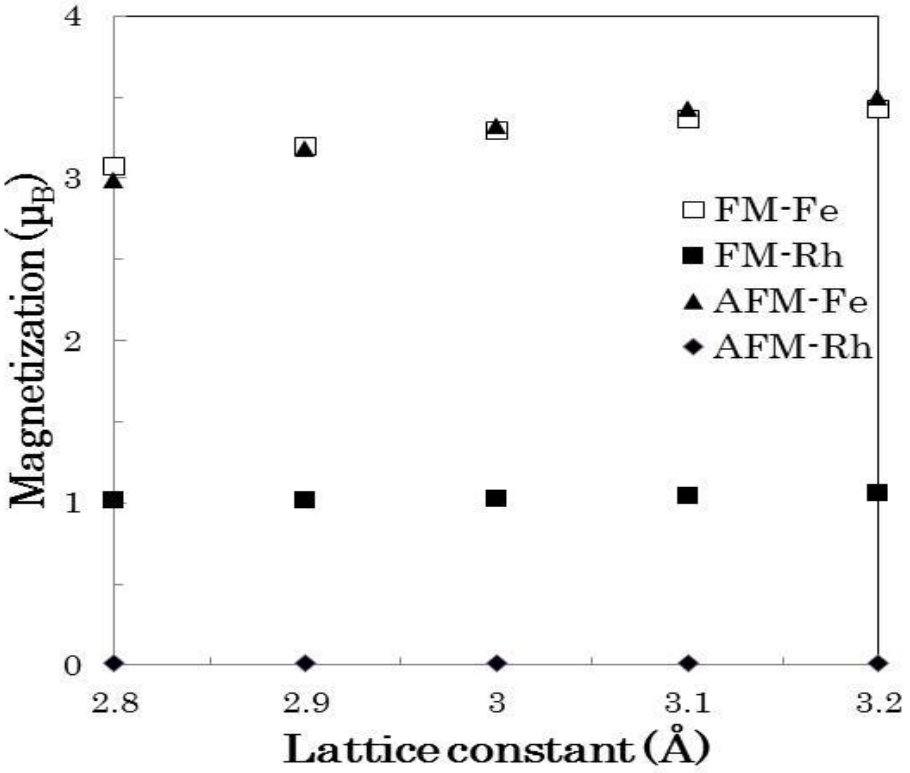

Fig. 13. m_{Fe} and m_{Rh} of FeRh in the AFM and FM states versus lattice constant.

4.3 Critical magnetic field

$H_c(0)$, which can provide us with useful information to understand the IMCE of FeRh, can be obtained using the following formula, [66)]

$$H_c\,(0) = \Delta E\,/\,(M_{FM} - M_{AFM}), \qquad (4.3.1)$$

where M_{FM} and M_{AFM} (= $0\mu_B$) are the average magnetization per atom of the FM and AFM states, respectively. A comparison between the obtained $H_c(0)$ and those given in experimental reports is presented in Table V. The obtained $H_c(0)$ (= 21.6 T) is consistent with the experimental values (= 21.2 T ~ 29.7 T).[28,29,30)]

4.4 DOS and PDOS

The DOS and the partial density of states (PDOS) near E_F of the Fe and Rh atoms in the FM and AFM states were investigated and are shown in Figs. 14(a)-14(d) and Figs. 15(a)-15(d), respectively. The distribution of the DOS near E_F of the FM state shown in Figs. 14(a) and 14(b) and of the AFM state shown in Figs. 14(c) and 14(d) are similar to the reported photoemission spectra.[35,36] In particular, the main peak positions of the DOS near E_F are around –5.0 eV to –4.0 eV and around –3.0 eV to –2.0 eV.

A comparison between $D(E_F)$ and the Sommerfeld coefficient, γ, calculated in the this work and those published in experimental reports was investigated. γ is obtained using the following formula.[64]

$$\gamma = D(E_F)\frac{\pi^2 k_B^2}{3}, \qquad (4.4.1)$$

where k_B is the Boltzmann constant. Comparisons between the obtained $D(E_F)$ and γ, and those published in the experimental reports are given in Table VIII.

The ratio of γ for the FM state to that of the AFM state (γ_{FM}/γ_{AFM})(= 4.72), which is also the ratio of $D(E_F)$ of the FM state to that of the AFM state ($D(E_F)_{FM}$ / $D(E_F)_{AFM}$), is consistent with the experimental values (from measurements of the specific heat capacity at low temperature for $Fe_{49}Rh_{51}$ in the AFM state and $Fe_{53}Rh_{47}$ and $Fe_{51}Rh_{49}$ in the FM state,[37] and for $Fe_{49.1}Rh_{50.9}$ in the AFM state and $Fe_{51.8}Rh_{48.2}$ in the FM state [38]).

The magnitudes of the obtained γ_{FM} and γ_{AFM} (32.9 mJ/(kg K^2), 6.97 mJ/(kg K^2)) are smaller than the experimental ones ((60 mJ/(kg K^2), 16 mJ/(kg K^2)),[37] (62.5 mJ/(kg K^2), 10.5 mJ/(kg K^2))[38]) because the electron-phonon coupling λ is neglected in the present work. In general, the relationship between the experimental γ (γ_{exp}) and the calculated γ (γ_{cal}) without the electron-phonon coupling λ is as follows.[70]

$$\gamma_{exp} = \gamma_{cal} \cdot (1+\lambda). \qquad (4.4.2)$$

The ratios for the experimental γ_{FM} and the γ_{FM} calculated here are 1.82 and 1.90, respectively. The equivalent ratios for the AFM state are 2.30 and 1.51, respectiveley. Therefore, λ for the FM state is 0.82 - 0.90 and that for the AFM state is 0.51 - 1.30. These values are quite large, suggesting that the electron-phonon coupling in FeRh is strong, which is consistent with the results of Szajek and Morkowski.[69,70)]

The reason that the obtained value of $D(E_F)_{FM}$ / $D(E_F)_{AFM}$ is large is examined using the PDOS, as shown in Figs. 15(a)-15(d). The PDOS at E_F ($PD(E_F)$) of Fe atoms in the FM state for the minority spin state is much higher than that in the AFM state for the minority spin state, while $PD(E_F)$ of Fe atoms for both the AFM and FM states for the majority spin state is low and $PD(E_F)$ of Rh atoms in both the AFM and FM states for both the majority spin and minority spin states are also low. Therefore, $D(E_F)_{FM}$ / $D(E_F)_{AFM}$ is large due to the large change in the contribution of the Fe_{3d} electrons to $D(E_F)$ in the AFM-FM phase transition.

The information gained from the obtained DOS is used in order to understand the reason why the change in m_{Fe} is much larger than that in m_{Rh} as mentioned in section 4.2. In the DOS below E_F, the distribution of Rh_{4d} orbitals is broader than in that of Fe_{3d} orbitals. Rh_{4d} electrons exist near the lower region, compared with Fe_{3d} electrons. Since the main component of $D(E_F)$ is due to Fe_{3d} in the minority spin state, it is thought that the change in lattice constant strongly influences m_{Fe}.

The effect of U on ΔE and m_{Fe} in the AFM and FM states, as mentioned in sections 4.1 and 4.2, was investigated using the obtained PDOS. Comparing Fig. 15(b) with Fig. 15(d), the magnetic states of Rh for the AFM and FM states are nonmagnetic and FM, respectively. When the magnitude of U_{Rh} is increased to 1.95 eV, the nonmagnetic state becomes unstable and the FM state becomes energetically advantageous. As a result, ΔE is smaller compared with the results of the GGA calculation. Moreover, the influence of the variation of the magnitude of U_{Rh} on the magnetic stability is investigated in A.1.1. From Figs. 15(a) and 15(c), we can see that the Fe_{3d} band in the majority spin state for the AFM and FM states is almost filled, while that in the minority spin state for the AFM and FM states is inadequately filled. Similar results (not shown) were obtained by the GGA calculations. When the magnitude of U_{Fe} is

increased to 2.0 eV, the Fe_{3d} band at E_F in the minority spin state moves to the upper energy side, which results in a decrease of the occupied Fe_{3d} PDOS in the minority spin state. This leads to an increase of m_{Fe} in the AFM and FM states and an improvement in the magnitude of the relationship between the values of m_{Fe} in the AFM and FM states.

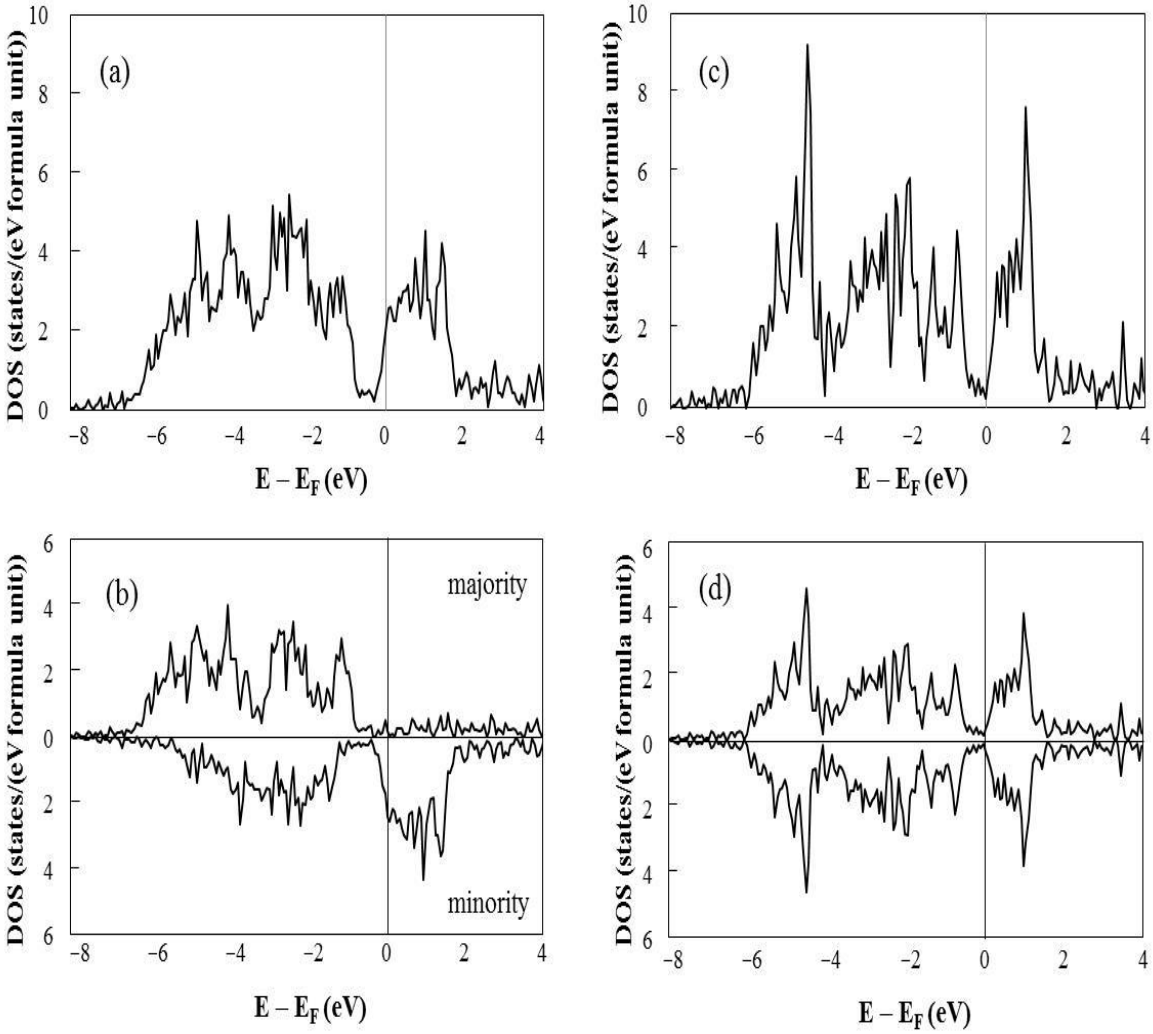

Fig. 14. DOS near E_F of (a) the FM state, (b) the FM state for both the majority and minority spin states, (c) the AFM state, and (d) the AFM state for each of the majority and minority spin states.

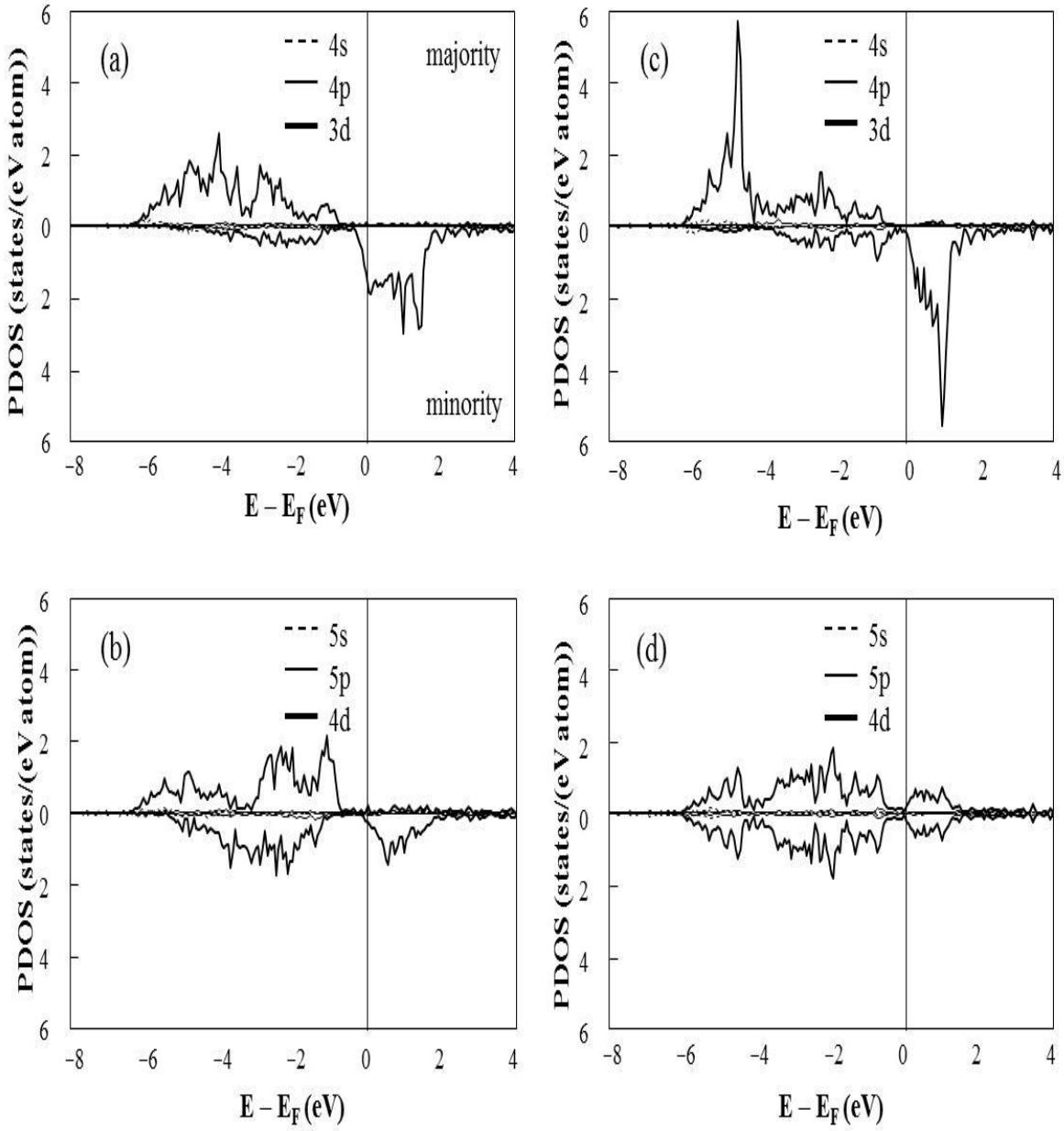

Fig. 15. PDOS near E_F of (a) an Fe atom in the FM state, (b) a Rh atom in the FM state, (c) an Fe atom in the AFM state and (d) a Rh atom in the AFM state.

Table VIII. Comparisons between $D(E_F)$ and the Sommerfeld coefficient, γ, in the present work and those from experimental reports.

	AFM		FM			
	$D(E_F)_{AFM}$ states/ (eV formula unit)	γ_{AFM} mJ/ (kg K^2)	$D(E_F)_{FM}$ states/ (eV formula unit)	γ_{FM} mJ/ (kg K^2)	$D(E_F)_{FM}$ / $D(E_F)_{AFM}$	γ_{FM} / γ_{AFM}
Present work	0.47	6.97	2.22	32.9	4.72	4.72
Ref. 37		16		60		3.75
Ref. 38		10.5		62.5		5.95

4.5 Band structures

4.5.1 Features of the band structures

The band structures of the AFM and FM states were investigated and are shown in Figs. 16(a)-16(c), respectively. The obtained band structures are shown using the symmetry points of the FCC structure. The two band structures are very different. In particular, in the FM state, the number of branches crossing the Fermi surface in the minority spin state is higher than that in the majority spin state. In the AFM state, a hole pocket appears at the center of the Γ point. In the case of the FM state, flat bands near -1 eV between Γ- X and between K - Γ in Fig. 16(a) contribute to the peak around -1 eV in the PDOS of the Rh atom for the majority spin state. In the case of the AFM state, a flat band near –0.3 eV to –0.2 eV between Γ - X in Fig. 16(c) contributes to the PDOS of the Rh atom immediately below E_F for both the majority and minority spin states.

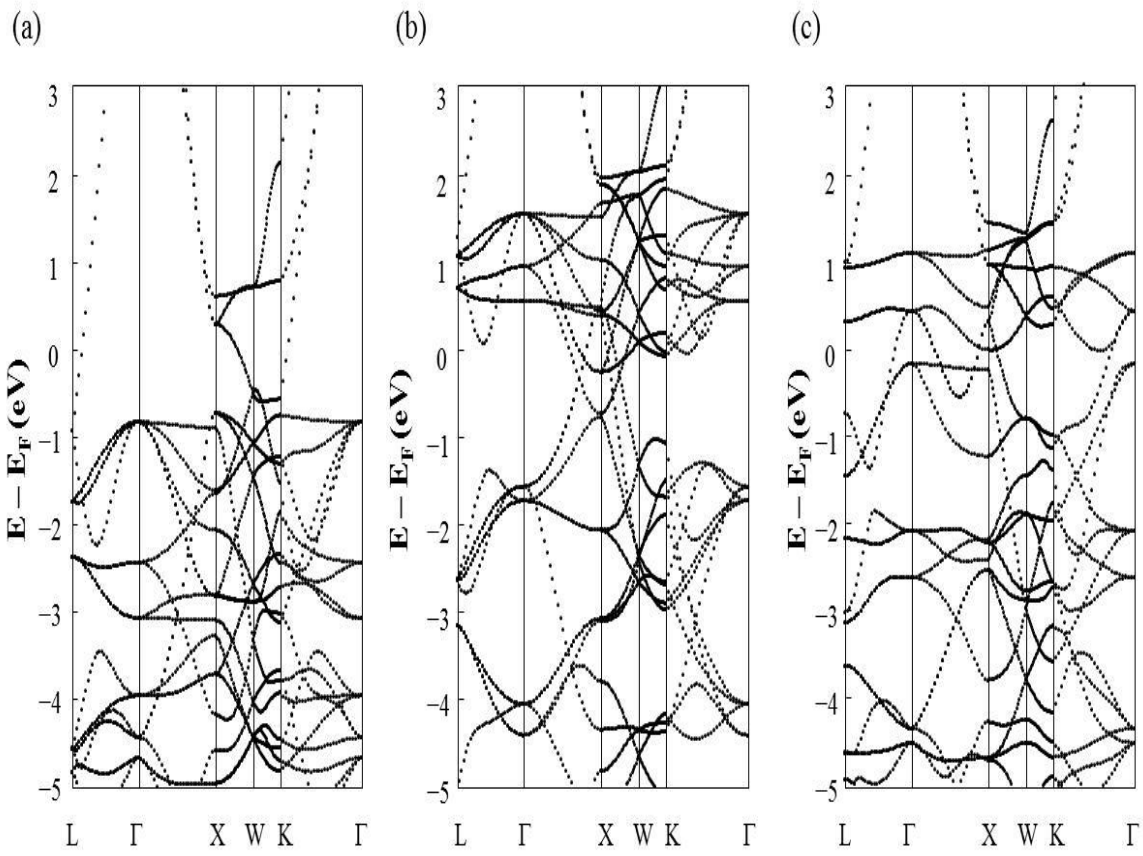

Fig. 16. Obtained band structures of (a) the FM state for the majority spin state, (b) the FM state for the minority spin state, and (c) the AFM state.

4.5.2 Electrical conductivity

The electrical conductivity (σ) of FeRh is investigated in this section. From Ref. 140, σ of an isotropic metal such as FeRh is obtained using the formula derived from the Boltzmann equation. Consider the case in which there is just a temperature gradient causing the electrons to diffuse with velocity $\mathbf{v_k}$. Since the electrons travel a distance $\mathbf{v_k} \cdot \Delta t$ in time Δt, the electron distribution $f(\mathbf{r},\mathbf{k},t)$ at the position $(\mathbf{r},\mathbf{k})$ in phase space at time t is equal to that at the position $(\mathbf{r}\text{-}\mathbf{v_k}\,\Delta t,\mathbf{k})$ at time $t\text{-}\Delta t$. Thus, the relationship $f(\mathbf{r},\mathbf{k},t) = f(\mathbf{r}-\mathbf{v_k}\cdot\Delta t,\mathbf{k},t-\Delta t)$ is satisfied. In contrast to a temperature

gradient, the change with time t of the electron distribution $f(\mathbf{r},\mathbf{k},t)$ at position $(\mathbf{r},\mathbf{k})$ in phase space is given by

$$\left(\frac{\partial f(\mathbf{r},\mathbf{k})}{\partial t}\right)_{diffusion} = \frac{f(\mathbf{r},\mathbf{k},t) - f(\mathbf{r},\mathbf{k},t-\Delta t)}{\Delta t} = \frac{f(\mathbf{r}-\mathbf{v}_{\mathbf{k}}\Delta t,\mathbf{k},t-\Delta t) - f(\mathbf{r},\mathbf{k},t-\Delta t)}{\Delta t}$$

$$= -\mathbf{v}_{\mathbf{k}} \cdot \frac{\partial f(\mathbf{r},\mathbf{k})}{\partial r} = -\mathbf{v}_{\mathbf{k}} \cdot \nabla f(\mathbf{r},\mathbf{k}), \qquad (4.5.1)$$

Both the electric and magnetic fields cause the wave vector $\mathbf{k}$ to change in accordance with the equation.

$$\frac{d\mathbf{k}}{dt} = -\frac{(-e)}{\hbar}(\mathbf{E} + \mathbf{v} \times \mathbf{B}). \qquad (4.5.2)$$

In the same manner as discussed above, the electron distribution $f(\mathbf{r},\mathbf{k},t)$ at position $(\mathbf{r},\mathbf{k})$ in phase space at time t is equal to that at position $(\mathbf{r},\mathbf{k}-(\partial\mathbf{k}/\partial t)\Delta t, t-\Delta t)$ at time t-Δt. The relationship $f(\mathbf{r},\mathbf{k},t) = f(\mathbf{r},\mathbf{k}-(\partial\mathbf{k}/\partial t)\cdot\Delta t,\mathbf{k},t-\Delta t)$ is satisfied.

$$\left(\frac{\partial f(\mathbf{r},\mathbf{k})}{\partial t}\right)_{field} = \frac{f(\mathbf{r},\mathbf{k},t) - f(\mathbf{r},\mathbf{k},t-\Delta t)}{\Delta t} = \frac{f\left(\mathbf{r},\mathbf{k}-\frac{\partial\mathbf{k}}{\partial t}\Delta t, t-\Delta t\right) - f(\mathbf{r},\mathbf{k},t-\Delta t)}{\Delta t}$$

$$= -\left(\frac{\partial\mathbf{k}}{\partial t}\right)_{field} \cdot \frac{\partial f(\mathbf{r},\mathbf{k})}{\partial\mathbf{k}} = -\frac{(-e)}{\hbar}(\mathbf{E} + \mathbf{v}_{\mathbf{k}} \times \mathbf{B}) \cdot \frac{\partial f_k}{\partial\mathbf{k}}. \qquad (4.5.3)$$

The change in the electron distribution caused by the external field and/or the temperature gradient is added to that of the scattering process, so that df/dt is given by;

$$\frac{df}{dt} = \left(\frac{\partial f}{\partial t}\right)_{diffusin} + \left(\frac{\partial f}{\partial t}\right)_{field} + \left(\frac{\partial f}{\partial t}\right)_{scatter}, \qquad (4.5.4)$$

In the steady state, $df/dt = 0$. Thus, the Boltzmann equation is given by

$$-\mathbf{v_k}\cdot\nabla f(\mathbf{r},\mathbf{k})-\frac{(-e)}{\hbar}(\mathbf{E}+\mathbf{v_k}\times\mathbf{B})\cdot\frac{\partial f_k}{\partial\mathbf{k}}=-\left(\frac{\partial f}{\partial t}\right)_{scatter}. \qquad (4.5.5)$$

The deviation of the steady state electron distribution function $f(\mathbf{r},\mathbf{k})$ in the presence of an external field from the Fermi-Dirac distribution function $f_0(E_k,T)$ is given by

$$\phi(\mathbf{r},\mathbf{k})=f(\mathbf{r},\mathbf{k})-f_0(E_k,T), \qquad (4.5.6)$$

where E_k is the energy and T is the temperature.

We assume $\phi(\mathbf{r},\mathbf{k})$ to be small. Equation (4.5.5) can be rewritten as

$$-\mathbf{v_k}\cdot\frac{\partial f_0}{\partial T}\nabla T-\frac{(-e)}{\hbar}(\mathbf{E}+\mathbf{v_k}\times\mathbf{B})\cdot\frac{\partial f_0}{\partial\mathbf{k}}=-\left(\frac{\partial f}{\partial t}\right)_{scatter}+\mathbf{v_k}\cdot\frac{\partial\phi}{\partial\mathbf{r}}+\frac{(-e)}{\hbar}(\mathbf{E}+\mathbf{v_k}\times\mathbf{B})\cdot\frac{\partial\phi}{\partial\mathbf{k}}. \qquad (4.5.7)$$

The term involving the magnetic field on the left hand side is zero, since

$$\mathbf{v_k}\times\mathbf{B}\cdot\frac{\partial f_0}{\partial\mathbf{k}}=\mathbf{v_k}\times\mathbf{B}\cdot\frac{\partial f_0}{\partial E_\mathbf{k}}\frac{\partial E_k}{\partial\mathbf{k}}=(\mathbf{v_k}\times\mathbf{B}\cdot\mathbf{v_k})\cdot\hbar\frac{\partial f_0}{\partial E_\mathbf{k}}=0. \qquad (4.5.8)$$

The term $\mathbf{E}\cdot\frac{\partial\phi}{\partial\mathbf{k}}$ on the right hand side is shown to be of the order of E^2 from equation (4.5.13), and is neglected, because of the deviation from Ohm's law.

By taking both the temperature and energy derivatives of the Fermi-Dirac distribution function, the following relation is satisfied.

$$\frac{\partial f_0}{\partial T}=-\left(\frac{\partial f_0}{\partial E}\right)\left[\left(\frac{E(\mathbf{k})-\varsigma}{T}\right)+\frac{\partial\varsigma}{\partial T}\right], \qquad (4.5.9)$$

where $f_0(E_k,T)=1/\{exp[(E_k-\varsigma)/k_BT]+1\}$ and ζ is the chemical potential.

Equation (4.5.5) can be rewritten as

$$\left(-\frac{\partial f_0}{\partial E}\right)\mathbf{v_k}\cdot\left[-\left(\frac{E(\mathbf{k})-\varsigma}{T}\right)\nabla T+(-e)\left(\mathbf{E}-\frac{\nabla\zeta}{(-e)}\right)\right]=-\left(\frac{\partial f}{\partial t}\right)_{scatter}+\mathbf{v_k}\cdot\frac{\partial\phi}{\partial\mathbf{r}}+\frac{(-e)}{\hbar}(\mathbf{v_k}\times\mathbf{B})\cdot\frac{\partial\phi}{\partial\mathbf{k}}.$$

(4.5.10)

The calculation of $\left(\frac{\partial f}{\partial t}\right)_{scatter}$ is given by

$$-\left(\frac{\partial f}{\partial t}\right)_{scatter}=\frac{f(\mathbf{r},\mathbf{k})-f_0(\varepsilon_k,T)}{\tau}=\frac{\phi(\mathbf{r},\mathbf{k})}{\tau},\qquad(4.5.11)$$

where τ is the relaxation time.

In the presence of just an electric field, equation (4.5.10) for a metal at constant temperature becomes

$$-\left(\frac{\partial f}{\partial t}\right)_{scatter}=\left(-\frac{\partial f_0}{\partial E_k}\right)\mathbf{v_k}\cdot(-e)\mathbf{E}.\qquad(4.5.12)$$

The term $\mathbf{v_k}\cdot\frac{\partial\phi}{\partial\mathbf{r}}$ in the right hand side of equation (4.5.10) vanishes because $\phi(\mathbf{r})$ is independent of the position **r** at a constant temperature. Using equation (4.5.11), equation (4.5.12) can be rewritten as

$$\frac{\phi(\mathbf{r},\boldsymbol{\kappa})}{\tau}=\left(-\frac{\partial f_0}{\partial E_k}\right)\mathbf{v_k}\cdot(-e)\mathbf{E}.\qquad(4.5.13)$$

Using the relationship $n=\frac{1}{4\pi^3}\iiint f_0(\mathbf{k})d\mathbf{k}$, where *n* is the number of electrons per unit volume, the current density is given by

$$\mathbf{J}=\frac{(-e)}{4\pi^3}\iiint\mathbf{v_k}f(\mathbf{k})d\mathbf{k}=\frac{(-e)}{4\pi^3}\iiint\mathbf{v_k}[f(\mathbf{k})-f_0(\mathbf{k})]d\mathbf{k}=\frac{(-e)}{4\pi^3}\iiint\mathbf{v_k}\phi(\mathbf{k})d\mathbf{k},\qquad(4.5.14)$$

where $\iiint\mathbf{v_k}f_0(\mathbf{k})d\mathbf{k}$ is zero.

Equation (4.5.14) can be rewritten using equation (4.5.13).

$$\mathbf{J}=\frac{e^2}{4\pi^3}\iiint\tau\mathbf{v_k}(\mathbf{v_k}\cdot\mathbf{E})\left(-\frac{\partial f_0}{\partial E_k}\right)d\mathbf{k}=\frac{e^2}{4\pi^3}\iiint\tau\mathbf{v_k}(\mathbf{v_k}\cdot\mathbf{E})\left(-\frac{\partial f_0}{\partial E_k}\right)\frac{dSdE_k}{|\nabla_k E_k|}.\qquad(4.5.15)$$

The following relationship is used.

$$\iiint d\mathbf{k} = \iint dS \int dk_{\perp} = \iint dS \int \frac{dE_k}{\left| \partial E_k / \partial k_{\perp} \right|} = \iint dS \int \frac{dE_k}{\left| \nabla_{k_{\perp}} E_k \right|}, \tag{4.5.16}$$

where $\iint dS$ is the integral over a constant energy surface and $\int dk_{\perp}$ is the integral in the normal direction.

The term $-\frac{\partial f_0}{\partial E_k}$ is finite only in close proximity to E_F and can be treated as the delta function.

Equation (4.5.15) is rewritten as

$$\mathbf{J} = \frac{e^2}{4\pi^3 \hbar} \iiint \frac{\tau \mathbf{v_k} \mathbf{v_k} dS_F}{v_{k\perp}} \cdot \mathbf{E}, \tag{4.5.17}$$

where S_F is the area of the Fermi surface.

The electrical conductivity tensor is defined as $\mathbf{J} = \boldsymbol{\sigma} \mathbf{E}$, where

$$\sigma_{ij} = \frac{e^2}{4\pi^3 \hbar} \int \frac{\tau v_i v_j dS_F}{v_{k\perp}}. \tag{4.5.18}$$

For an isotropic metal, the diagonal and off-diagonal elements of the conductivity tensor satisfy the relationships $\sigma_{ij} = \sigma$ and $\sigma_{ij} = 0$ with $i \neq j$. $v_{k\perp} = v_F$ holds on the Fermi surface.

$$\boldsymbol{\sigma} = \frac{e^2}{4\pi^3 \hbar} \int \frac{\tau \mathbf{v_k} \mathbf{v_k} dS_F}{v_{k\perp}} = \frac{e^2 \tau v_F S_F}{12\pi^3 \hbar}, \tag{4.5.19}$$

where $v_F^2 = \sum_{i=x,y,z} v_i^2 = 3v_i^2$ is used.

D(E) is given by

$$D(E)dE = \frac{1}{4\pi^3}\iint \frac{dSdE_k}{|\nabla_{k\perp}E_k|}. \quad (4.5.20)$$

Equation (4.5.19) can be rewritten as

$$\sigma = \frac{e^2}{3}\Lambda_F v_F D(E_F), \quad (4.5.21)$$

where e is the elementary charge, v_F is the Fermi velocity, and Λ_F is the mean free path given by $\Lambda_F = \tau v_F$ (τ is the relaxation time).

$$\frac{1}{\tau} = \frac{1}{\tau_{el-ph}} + \frac{1}{\tau_{im}}, \quad (4.5.22)$$

where $\tau_{el\text{-}ph}$ is the relaxation time related to electron-phonon scattering and τ_{im} is the relaxation time related to the scattering of electrons at impurities. In FeRh, at room temperature, we assume that

$$\tau \approx \tau_{el-ph}. \quad (4.5.23)$$

The v_F of FeRh is investigated in the following. Comparing Fig. 16(a) with Fig. 16(c), the gradient of the energy dispersion in k-space in the case of the AFM state is smaller than that in the case of the FM state. Since v_F is proportional to dE_F/dk at the Fermi wave number (k_F) as in the following equation,[140)]

$$v_F = \frac{d\varpi}{dk} = \frac{1}{\hbar}\frac{dE}{dk} \quad \text{at } k_F. \quad (4.5.24)$$

v_F for the AFM state is similar to that for the FM state, because the gradient of the energy dispersion in k-space for the FM state shown in Fig. 16(b) is small. Therefore, we assume that v_F is constant for both the AFM and FM states.

Here, in order to understand the mechanism of σ near T_{tr} in detail, we investigate the relationship between the electrical resistivity (ρ_e), which is in inverse proportion to σ, and T shown in Fig. 17 using equation (4.5.21) and the above assumptions. The results are detailed in the following.

(i) Below T_{tr}, Λ_F decreases with increasing T because τ (= $\tau_{el\text{-}ph}$) is inversely

proportional to T for the following reason.

The rate of the electron-phonon scattering increases in proportion with the number of phonons involved. This number increases linearly with T. ρ_e gradually increases in proportion with T following the Bloch–Grüneisen law at high temperature[140] as the temperature approaches T_{tr}.

(ii) As temperature approaches T_{tr} further, ρ_e increases slowly due to the occurrence of the coexistence of the AFM and FM states[46-56] (because the FM state which has high $D(E_F)$ begins to appear).

(iii) Finally, ρ_e no longer increases, and then begins to decrease sharply in the immediate vicinity of T_{tr}. At T_{tr}, ρ_e becomes approximately 50% of the maximum of ρ_e in the AFM state. However, since Λ_F in the FM state at high temperature is smaller than that in the AFM state at low temperature, the magnitude of the decrease in ρ_e is smaller than that predicted from the ratio $D(E_F)_{FM}/D(E_F)_{AFM}$ (= 4.72).

(iv) Above T_{tr}, ρ_e gradually increases in proportion with T again. The gradient of the graph is smaller than that in the case of (i). However, we can not understand it using equation (4.5.21). Using the Bloch–Grüneisen law at high temperature (ρ_e is almost inversely proportional to the square of the Debye temperature[140]), it can be understood because it seems that the Debye temperature of the FM state is larger than that of the AFM state using the obtained calculation results that B_{FM} is larger than B_{AFM} and E_{YFM} is larger than E_{YAFM}.

(v) There is the hysteresis in ρ_e from 350K to 390K. It is due to the difference in the temperature range of the coexisting phase of the AFM and FM states between the AFM-FM phase transition upon heating and that on cooling.

From the above results, we can theoretically reproduce the tendency of temperature dependence of ρ_e near $T_{tr,}$ especially the abrupt decrease of the magnitude of ρ_e below T_{tr} with increasing temperature.

Moreover, we can understand the behavior of σ of FeRh from the obtained DOS. The DOS between –0.5 and 0.0 eV for the AFM state and between -0.8 and -0.2 eV for the FM state are low as shown in Fig. 14(c) and Fig. 14(a), respectively. Therefore, the

AFM state is not like a normal metal, whereas the FM state is like that of Fe. This result is consistent with the indication of Schinkel et al.[40] who suggested that FeRh is a semimetal. From the above discussion, the main mechanism of σ near T_{tr} can be reasonably understood through electron transport theory using the physical quantities obtained for the AFM and FM states, such as DOS and the band structures.

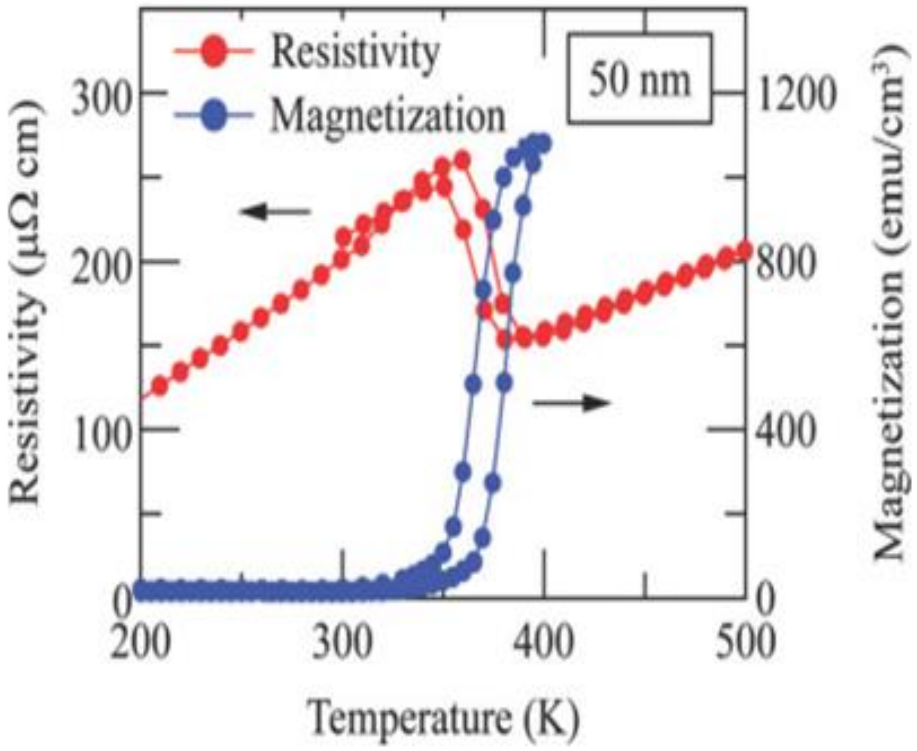

Fig. 17. Electrical resistivity (ρ_e) vs temperature (T) cited from Ref. 31.

4.6 Wavefunctions

In order to understand the state of the hybridization of the Fe and Rh orbitals in more detail, we investigated the decomposition of the wavefunction of the valence band near the Γ point for the majority and minority spin states of the FM and AFM

states, respectively, which are listed in Table IX(a), Table IX(b), Table X(a) and Table X(b), respectively. From these, we see that the wavefunctions comprise the following.

(i) Strongly hybridized Fe_{3d} and Rh_{4d} orbitals.

(ii) Fe_{3d} or Rh_{4d} orbitals only.

(iii) Strongly hybridized Fe_{3d}, Rh_{4d} and Rh_{5p} orbitals.

Our findings are as follows.

i) In both the AFM and FM states, a strong interaction between Fe_{3d} and Rh_{4d} electrons as well as interactions between Fe_{3d} electrons and between Rh_{4d} electrons occurs.

ii) In the case of the AFM state, there are localized wavefunctions consisting of strongly hybridized Fe_{3d}, Rh_{4d} and Rh_{5p} orbitals characterized by the result that the contribution of the Fe_{3d} electrons of Fe_1 is very much different from that of Fe_2 (the contribution of Fe_{3d} electrons of Fe_1 or Fe_2 is negligible), while the contribution of the Rh_{4d} and Rh_{5p} electrons of Rh_1 is the same as that of Rh_2. The superexchange-like interaction, such as the interaction discussed in A.4 may occur due to this strong hybridization because the following magnetic interaction between Fe atoms via an Rh atom shown in Fig. 10(a) can be explained in terms of the Goodenough-Kanamori rules which can be applied to the system that the superexchange interaction works. 1) With two Fe atoms on the diagonal line of the cubic crystal structure and the angle of Fe-Rh-Fe being 180°, the interaction between two Fe atoms is AFM. 2) With two Fe atoms on the diagonal line of the face of the cubic crystal structure and the angle of Fe-Rh-Fe being 109.5° (about 90°), the interaction between them is FM.

iii) In the case of the FM state, there are delocalized wavefunctions comprising the strongly hybridized Fe_{3d} and Rh_{4d} orbitals characterized by the result that the contribution of the Fe_{3d} electrons of Fe_1 is the same as that of Fe_2 and the contribution of the Rh_{4d} electrons of Rh_1 is the same as that of Rh_2. This indicates the occurrence of an itinerant-electron FM interaction between Fe atoms via an Rh atom, which is consistent with the itinerant magnetism based on the Stoner mechanism discussed in A.6.

These results almost concur with those of Vries et al.[39] They suggested that the orbital-selective Mott transition concerning the Fe_{3d} electrons is unaffected by the presence of other bands crossing E_F, such as Fe_{4s}, Fe_{4p}, Rh_{5s}, Rh_{5p} and Rh_{4d}, occurring in FeRh. In the AFM state, Fe_{3d} electrons have the characteristics of localized electrons at low temperature, while with increasing temperature, the effect of U between the electrons can give rise to ferromagnetism by the Stoner mechanism.

Table IX. Decomposition of the obtained wavefunctions of the valence band near E_F in the FM state. The data is ordered such that the energies of the wavefunctions are from low to high.

(a) Majority spin state.

Energy level 0	Ion number	Fe_{4s}	Rh_{5s}	Fe_{4p}	Rh_{5p}	Fe_{3d}	Rh_{4d}	Sum
	Fe_1	0	-	0	-	0.128	-	0.128
	Fe_2	0	-	0	-	0.128	-	0.128
	Rh_3	-	0	-	0	-	0.367	0.367
	Rh_4	-	0	-	0	-	0.367	0.367
	Sum	0	0	0	0	0.256	0.734	0.99

Energy level 1	Ion number	Fe_{4s}	Rh_{5s}	Fe_{4p}	Rh_{5p}	Fe_{3d}	Rh_{4d}	Sum
	Fe_1	0	-	0	-	0	-	0
	Fe_2	0	-	0	-	0	-	0
	Rh_3	-	0	-	0	-	0.495	0.495
	Rh_4	-	0	-	0	-	0.495	0.495
	Sum	0	0	0	0	0	0.99	0.99

Energy level 2	Ion number	Fe_{4s}	Rh_{5s}	Fe_{4p}	Rh_{5p}	Fe_{3d}	Rh_{4d}	Sum
	Fe_1	0	-	0	-	0.243	-	0.243
	Fe_2	0	-	0	-	0.243	-	0.243
	Rh_3	-	0	-	0	-	0.241	0.241
	Rh_4	-	0	-	0	-	0.241	0.241
	Sum	0	0	0	0	0.486	0.482	0.969

Energy level 3	Ion number	Fe_{4s}	Rh_{5s}	Fe_{4p}	Rh_{5p}	Fe_{3d}	Rh_{4d}	Sum
	Fe_1	0	-	0	-	0.491	-	0.491
	Fe_2	0	-	0	-	0.491	-	0.491
	Rh_3	-	0	-	0	-	0	0
	Rh_4	-	0	-	0	-	0	0
	Sum	0	0	0	0	0.982	0	0.982

(b) Minority spin state.

Energy level 0	Ion number	Fe_{4s}	Rh_{5s}	Fe_{4p}	Rh_{5p}	Fe_{3d}	Rh_{4d}	Sum
	Fe_1	0	-	0	-	0.376	-	0.376
	Fe_2	0	-	0	-	0.376	-	0.376
	Rh_3	-	0.074	-	0	-	0	0.074
	Rh_4	-	0.074	-	0	-	0	0.074
	Sum	0	0.148	0	0	0.752	0	0.9

Energy level 1	Ion number	Fe_{4s}	Rh_{5s}	Fe_{4p}	Rh_{5p}	Fe_{3d}	Rh_{4d}	Sum
	Fe_1	0	-	0	-	0.147	-	0.147
	Fe_2	0	-	0	-	0.147	-	0.147
	Rh_3	-	0	-	0	-	0.343	0.343
	Rh_4	-	0	-	0	-	0.343	0.343
	Sum	0	0	0	0	0.294	0.686	0.98

Table X. Decomposition of the obtained wavefunctions of the valence band near E_F in the AFM state.

(a) Majority spin state.

Energy level 0	Ion number	Fe_{4s}	Rh_{5s}	Fe_{4p}	Rh_{5p}	Fe_{3d}	Rh_{4d}	Sum
	Fe_1	0	-	0	-	0	-	0
	Fe_2	0	-	0	-	0	-	0
	Rh_3	-	0	-	0	-	0.495	0.495
	Rh_4	-	0	-	0	-	0.495	0.495
	Sum	0	0	0	0	0	0.99	0.99

Energy level 1	Ion number	Fe_{4s}	Rh_{5s}	Fe_{4p}	Rh_{5p}	Fe_{3d}	Rh_{4d}	Sum
	Fe_1	0	-	0	-	0.003	-	0.003
	Fe_2	0	-	0	-	0.397	-	0.397
	Rh_3	-	0	-	0.022	-	0.259	0.281
	Rh_4	-	0	-	0.022	-	0.259	0.281
	Sum	0	0	0	0.044	0.4	0.518	0.962

Energy level 2	Ion number	Fe_{4s}	Rh_{5s}	Fe_{4p}	Rh_{5p}	Fe_{3d}	Rh_{4d}	Sum
	Fe_1	0	-	0	-	0.571	-	0.571
	Fe_2	0	-	0	-	0.019	-	0.019
	Rh_3	-	0	-	0	-	0.19	0.19
	Rh_4	-	0	-	0	-	0.19	0.19
	Sum	0	0	0	0	0.59	0.38	0.97

(b) Minority spin state.

Energy level 0	Ion number	Fe_{4s}	Rh_{5s}	Fe_{4p}	Rh_{5p}	Fe_{3d}	Rh_{4d}	Sum
	Fe_1	0	-	0	-	0	-	0
	Fe_2	0	-	0	-	0	-	0
	Rh_3	-	0	-	0	-	0.495	0.495
	Rh_4	-	0	-	0	-	0.495	0.495
	Sum	0	0	0	0	0.752	0	0.99

Energy level 1	Ion number	Fe_{4s}	Rh_{5s}	Fe_{4p}	Rh_{5p}	Fe_{3d}	Rh_{4d}	Sum
	Fe_1	0	-	0	-	0.397	-	0.397
	Fe_2	0	-	0	-	0.003	-	0.003
	Rh_3	-	0	-	0.022	-	0.259	0.281
	Rh_4	-	0	-	0.022	-	0.259	0.281
	Sum	0	0	0	0.044	0.4	0.518	0.962

Energy level 2	Ion number	Fe_{4s}	Rh_{5s}	Fe_{4p}	Rh_{5p}	Fe_{3d}	Rh_{4d}	Sum
	Fe_1	0	-	0	-	0.019	-	0.019
	Fe_2	0	-	0	-	0.57	-	0.57
	Rh_3	-	0	-	0	-	0.19	0.19
	Rh_4	-	0	-	0	-	0.19	0.19
	Sum	0	0	0	0	0.589	0.38	0.969

Chapter 5

Conclusion

We investigated the electronic and magnetic structures of FeRh using first principles calculations with the GGA + U method. By choosing appropriate values of U_{Fe} and U_{Rh}, we succeeded in reproducing the AFM-FM phase transition quantitatively for the first time. Physical quantities, including ΔE, the lattice constant, the bulk modulus, Young's modulus, the magnetization, $H_c(0)$, the DOS, the band structures and the wavefunctions are consistent with the experimental reports. In particular, the following important effects on the physical quantities obtained in the present work were found.

(i) U strongly influences ΔE, $H_c(0)$ and m_{Fe}. As the magnitude of U_{Rh} increases, the FM state gradually becomes more energetically advantageous than the AFM state. The m_{Fe} of the AFM state gradually approaches and then becomes equal to the m_{Fe} of the FM state as the magnitude of U_{Fe} increases, while the m_{Fe} of the AFM state < m_{Fe} of the FM state if the magnitude of U_{Fe} = 0.

(ii) Changes in lattice constant more strongly influence m_{Fe} than m_{Rh}. Especially, the magnitude relation of m_{Fe} values between the AFM and FM states is reversed near the observed lattice constant.

(iii) $D(E_F)_{FM}$ / $D(E_F)_{AFM}$ is large because $PD(E_F)$ of an Fe atom (especially Fe_{3d} electrons) changes when changing from the AFM to the FM state.

(iv) Strong hybridization of the orbitals of Fe and Rh atoms (especially, the Fe_{3d} and Rh_{4d} orbitals for the AFM and FM states, and the Fe_{3d}, Rh_{5p} and Rh_{4d} orbitals for the AFM state) comprising the wavefunctions of the valence band near E_F appears. Hybridization for the AFM state is different from that for the FM state, which reflects the difference between the interactions in the AFM and FM states. The interaction between Fe atoms via an Rh atom generated by this hybridization plays an important role in determining the magnetic state.

The above results help us understand the microscopic mechanisms that give rise to the changes in the electronic, magnetic and mechanical properties taking place as a result of the phase transition from the AFM to the FM state. In particular, changes in physical properties, such as the electrical conductivity, occurring when going from the AFM to the FM state can be understood through electron transport theory using the physical quantities obtained for the AFM and FM states, such as $D(E_F)_{FM}$ / $D(E_F)_{AFM}$ and the band structures. Consequently, we were able to provide further clarification to the electronic and magnetic structures and understand them more fully, thereby helping us to clarify the origin of the AFM-FM phase transition and the IMCE of FeRh.

Our plans for the near future are to investigate the origins of the AFM-FM phase transition and the IMCE of FeRh in more detail according to the following steps.

i) The origin of the AFM-FM phase transition is investigated. A calculation of ΔS (= electronic entropy change (ΔS_{ele}) + magnetic entropy change (ΔS_{mag}) + lattice entropy change (ΔS_{lat})) is performed.[141] In particular, (ΔS_{mag}) ($= \int_0^T \Delta C_{mag}(T) \mathrm{d}T/T$) is calculated by using the magnetic specific heat capacity difference between the AFM and FM states ($\Delta C_{mag}(T)$) ($=C_{mag}^{FM}(T) - C_{mag}^{AFM}(T)$) derived from the Monte Carlo calculation of the Heisenberg model based on the band calculation results for some configurations of magnetic moments. The Helmholtz free energy difference between the AFM-FM states ($\Delta F(T)$) based on results of this work is calculated and T_{tr} corresponding to the condition that $\Delta F(T_{tr}) = 0$ is solved.

ii) The origin of the IMCE is investigated. Calculations of $\Delta S_{iso}(T,\Delta H)$ (= isothermal electronic entropy change ($\Delta S_{iso}^{ele}(T,\Delta H)$) + isothermal magnetic entropy change ($\Delta S_{iso}^{mag}(T,\Delta H)$)) and specific heat capacity ($C(T,H)$) (= electronic specific heat capacity ($C_{ele}(T,H)$) + magnetic specific heat capacity ($C_{mag}(T,H)$) + lattice specific heat capacity ($C_{lat}(T,H)$)) are performed.[141,142] Especially, $\Delta S_{iso}^{mag}(T,\Delta H)$ ($= \int_0^T \Delta C_{mag}(T,\Delta H) \mathrm{d}T/T$) is calculated by using the magnetic specific heat capacity difference ($\Delta C_{mag}(T, \Delta H)$) (= $C_{mag}(T,H_2)$ -

$C_{\mathrm{mag}}(T,H_1)$) derived from the Monte Carlo calculation of the above Heisenberg model containing the term with respect to the Zeeman effect. ΔT_{ad} is calculated from the formula: $\Delta T_{ad}(T,\Delta H) = -\int_{H_1}^{H_2} \frac{T}{C(T,H)} \left[\frac{\partial S(T,H)}{\partial H}\right]_T dH$.

Moreover, detailed comparisons between FeRh and other materials showing IMCE, such as $Mn_{2-x}Cr_xSb$, will be made (however, a simple discussion can be found in A.7).

Finally, we hope that the findings in this work will prove useful for creating new high-performance MCMs and IMCMs.

Appendices

A.1 Comparison between computational results using the GGA + *U* method and those using the LSDA + *U* method

A.1.1 Choice of *U*

First principles calculations of the electronic and magnetic structures were performed using two kinds of approximations, i. e., the LSDA+*U* method and the GGA+*U* method. If the values of *U* and *J* (in the present work, both J_{Fe} and J_{Rh} were set to 1.0 eV as mentioned above) used in the two methods are chosen appropriately to realize the experimentally observed data, such as the value of ΔE found in the experimental reports, we can obtain a relationship between the total energies of the AFM and FM states and the lattice constant, which is shown in Fig. 12 for the GGA+*U* method and in Fig.19 for the LSDA+*U* method. The difference in total energies in both cases is small and is almost equal near a_{FM}. In order to satisfy the relationships between the total energies of the AFM and FM states shown in Fig. 12 and Fig. 19, the relationships between U_{Fe} and U_{Rh} shown in Fig. 18 were obtained for the cases of the LSDA+*U* and the GGA+*U* methods. For constant U_{Fe}, the FM state becomes more stable with increasing U_{Rh}, and the AFM state becomes more stable with decreasing U_{Rh}. The reason for this is as follows. As U_{Rh} increases, it becomes more difficult for two electrons within an Rh atom to go into the same electron orbital and it is easy for them to be in separate orbitals within the same Rh atom. The Rh atoms will be in the FM state. On the contrary, as U_{Rh} becomes smaller, two electrons can easily go into the same electron orbital. The Rh atoms will then be in a nonmagnetic state.

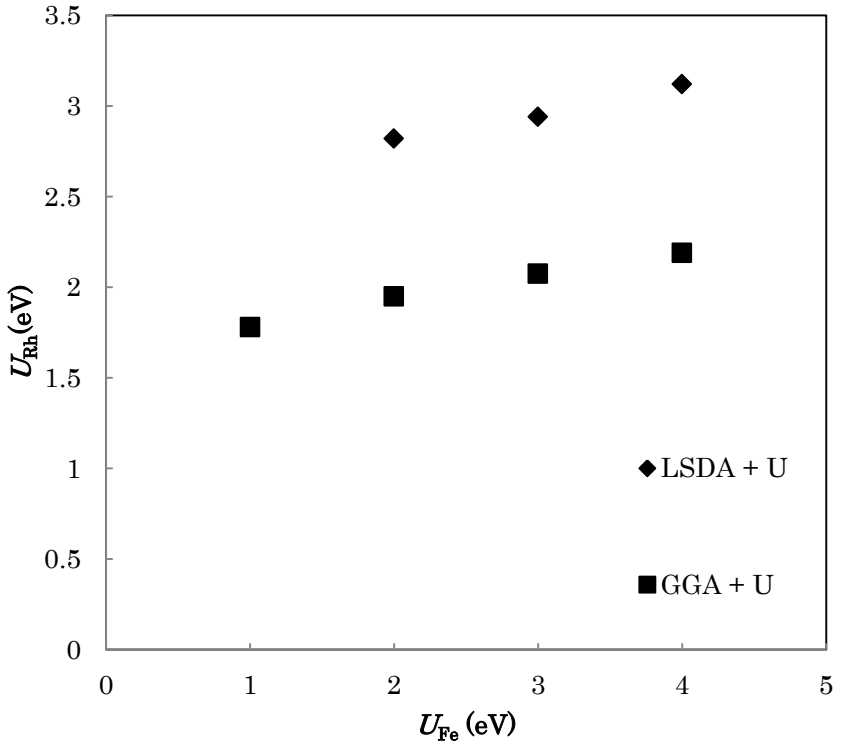

Fig. 18. U_{Fe} versus U_{Rh} in the case of the coexistence of the AFM and FM states. The closed squares and diamonds show the data using the GGA+*U* method and those using the LSDA + *U* method, respectively.

A.1.2 Results of calculations using the LSDA +*U* method

The electronic and magnetic structures of FeRh were investigated using the LSDA+*U* method. Using the same value of U_{Fe} as for the GGA+*U* method, the value of U_{Rh} used for the LSDA+*U* method is larger than that used for the GGA+*U* method. For the LSDA+*U* method, the lattice constants corresponding to the AFM and FM states are smaller (nearly 0.1 Å) compared with the experimental reports. With U_{Fe} = 2.0 eV and U_{Rh} = 2.82 eV, the relationships between the total energies in the FM and AFM states and the lattice constant are shown in Fig.19. The DOS of the FM and AFM states are shown in Figs.20(a) and 20(b).

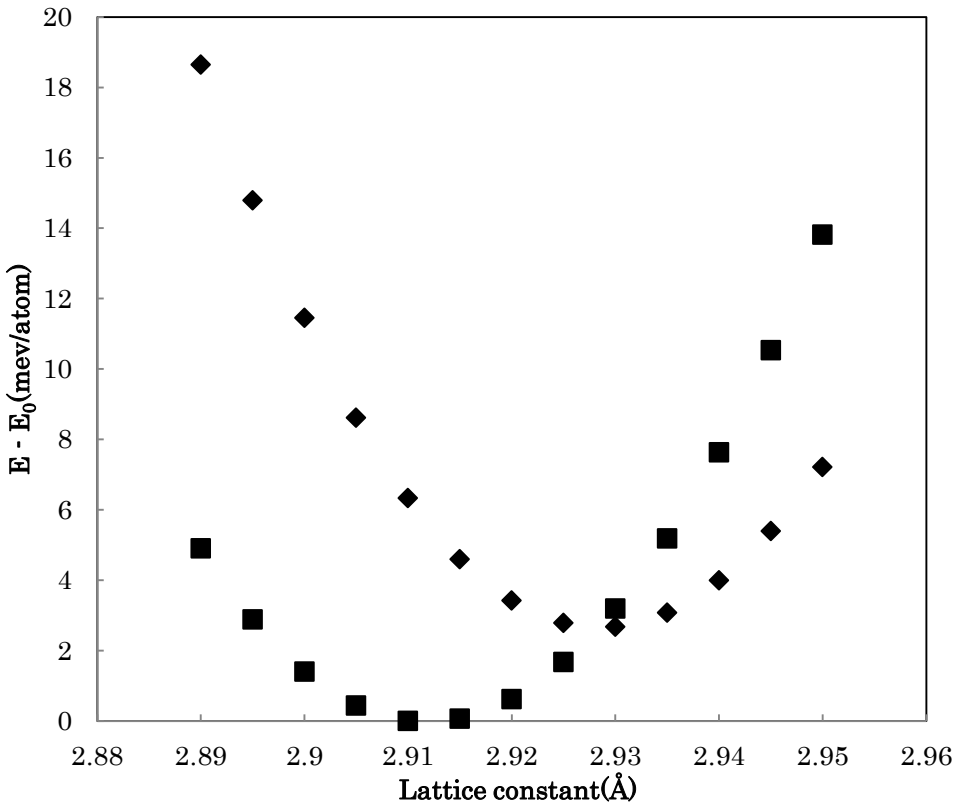

Fig. 19. Total energy versus lattice constant using the LSDA +U method where U_{Fe} = 2.0 eV and U_{Rh} = 2.82 eV and the minimum of the AFM state is set to zero. The closed squares and diamonds show the total energies of the AFM and FM states, respectively.

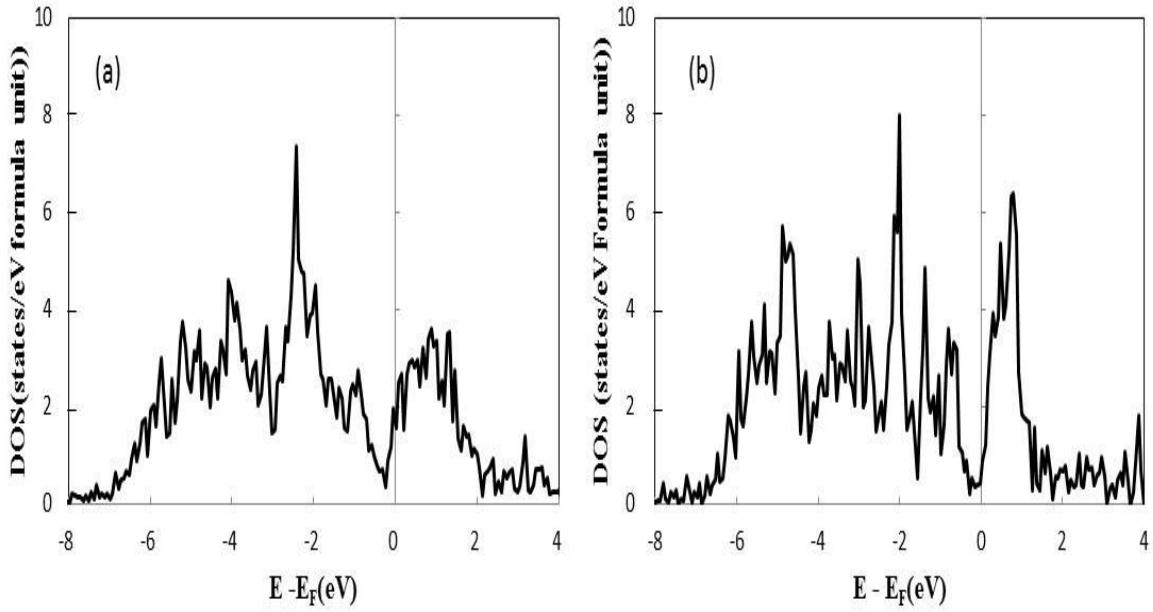

Fig. 20. DOS near E_F for (a) the FM state and (b) the AFM state using LSDA+U where U_{Fe} = 2.0 eV and U_{Rh} = 2.82 eV.

The bulk modulus obtained using the LSDA+U method is larger (about 20 GPa) than that obtained using the GGA+U method because the energy curve obtained using the LSDA+U method is sharper than that obtained using the GGA+U method. For this reason, the results obtained using the GGA+U method are more appropriate than those obtained using the LSDA + U method for investigating the electronic and magnetic structures of FeRh.

A.2 Comparison between the results of calculations using the GGA+U method with U_{Fe}=2.0 eV and those with U_{Fe} = 1.0 eV and 4.0 eV

The influence of U_{Fe} and U_{Rh} on a_{AFM} and a_{FM} was investigated. The values of a_{AFM} and a_{FM} with U_{Fe}=1.0 eV and U_{Rh} = 1.85 eV, U_{Fe}=2.0 eV and U_{Rh} = 1.95 eV, and

U_{Fe}=4.0 eV and U_{Rh}= 2.19 eV are 2.985 Å and 3.0 Å, 2.99 Å and 3.01 Å, and 3.00 Å and 3.02 Å, respectively. a_{AFM} and a_{FM} increase as the values of U_{Fe} and U_{Rh} are increased.

The influence of U_{Fe} on m_{Fe} in the AFM state was investigated. The values of m_{Fe} with U_{Fe} = 1.0 eV and U_{Rh} = 1.85 eV, U_{Fe}=2.0 eV and U_{Rh} = 1.95 eV, and U_{Fe}=4.0 eV and U_{Rh} = 2.19 eV are 3.14 μ_B, 3.31 μ_B, and 3.58 μ_B, respectively. The influence of U_{Fe} on the values of m_{Fe} and m_{Rh} in the FM state was also investigated. The values of m_{Fe} and m_{Rh} for U_{Fe} = 1.0 eV and U_{Rh} = 1.85 eV, U_{Fe}=2.0 eV and U_{Rh} = 1.95 eV, and U_{Fe}=4.0 eV and U_{Rh} = 2.19 eV are 3.17 μ_B and 1.06 μ_B, 3.31 μ_B and 1.04 μ_B, and 3.51 μ_B and 0.95 μ_B, respectively. These results reveal the following tendencies. When U_{Fe} and U_{Rh} are small, m_{Fe} in the FM state is larger than that in the AFM state. On the other hand, when they are large, m_{Fe} in the FM state is smaller than in the AFM state. On increasing U_{Fe} and U_{Rh}, m_{Fe} increases significantly, whereas m_{Rh} decreases slightly.

The influence of U_{Fe} on the values of $D(E_F)_{FM}$ and $D(E_F)_{AFM}$ was investigated. The ratio of $D(E_F)_{FM}/D(E_F)_{AFM}$ for U_{Fe}= 1.0 eV and U_{Rh} = 1.85 eV, U_{Fe}=2.0 eV and U_{Rh} = 1.95 eV, U_{Fe}=4.0 eV and U_{Rh} = 2.19 eV are 3.04, 4.72, and 7.35, respectively. The value of U strongly influences $D(E_F)$.

In order to reproduce the DOS obtained from the experimental reports, we calculated DOS using the GGA+U method. The obtained DOSs for the FM and AFM states where U_{Fe}= 1.0 eV are shown in Figs. 21(a) and 21(b), respectively and are consistent with the experimental reports. However, since U_{Rh} is 1.85 eV, it almost twice the value of U_{Fe}, which is, therefore, thought to be too small. Moreover, the result that U_{eff} = 0 for Fe atoms where U_{eff} = U_{Fe} – J disagrees with the reported calculations that give the value of U_{eff} to be between 0.5 and 6.0 eV.[126,143-145] The obtained DOSs for the FM and AFM states where U_{Fe}= 4.0 eV and U_{Rh}= 2.19 eV are shown in Figs. 21(c) and 21(d), respectively. These are inconsistent with those of spectral measurements using photoemission spectroscopy because the large width of the valence band makes the Fe_{3d} electrons excessively stable. From the above results, the DOSs with U_{Fe}= 2.0 eV are better at reproducing real FeRh spectra than those with either U_{Fe}= 1.0 eV or 4.0 eV.

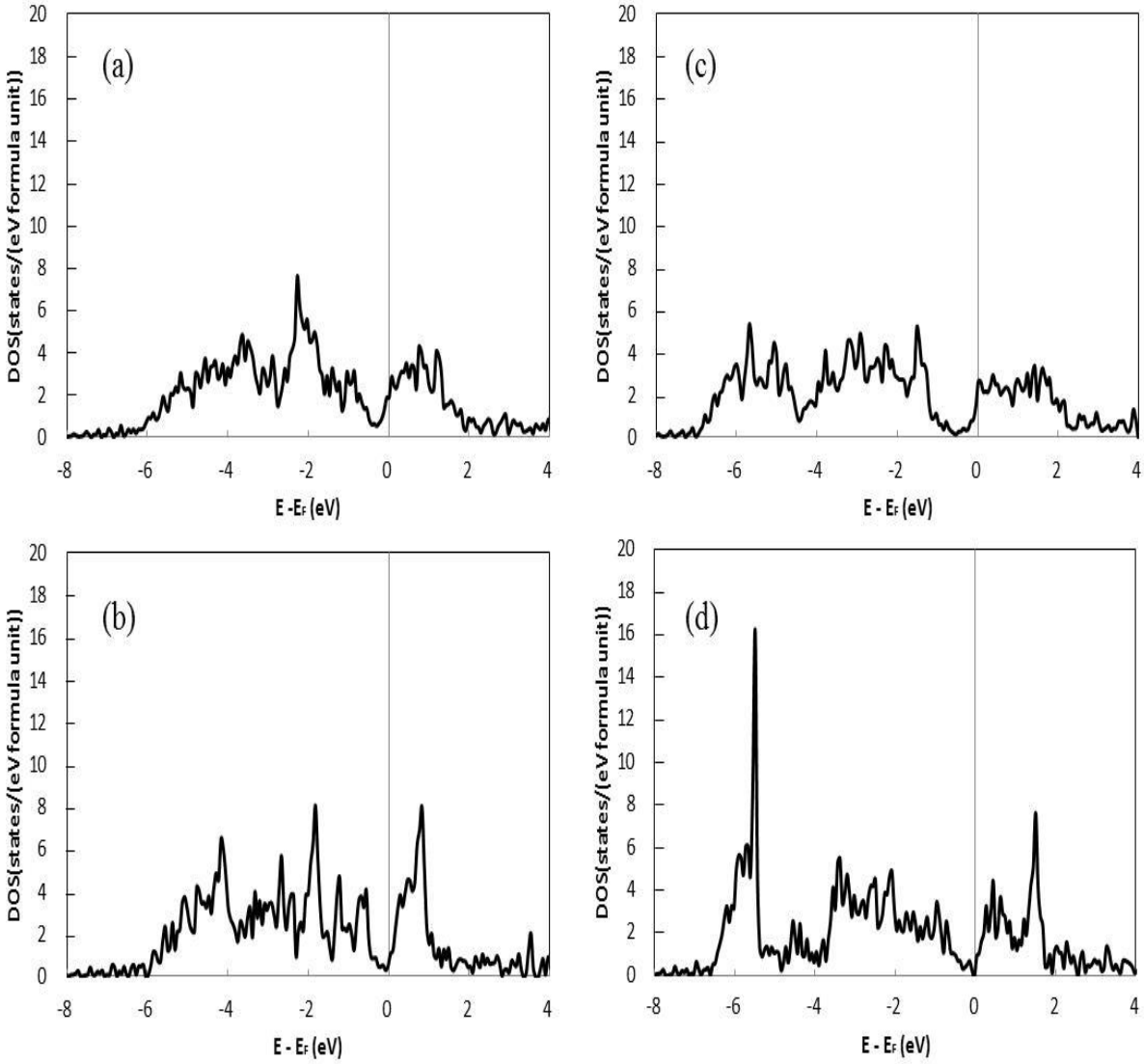

Fig. 21. DOS of (a) the FM state, (b) the AFM state of FeRh where U_{Fe}= 1.0 eV and U_{Rh}= 1.78 eV, (c) the FM state, and (d) the AFM state of FeRh where U_{Fe}= 4.0 eV and U_{Rh}= 2.19 eV using the GGA + U method.

A.3 Comparison between the values of U_{Fe} and U_{Rh} used in this work and those used in other publications

The reported value of U_{eff} used in calculations for Fe oxides based on the GGA+U method is 3.2 eV (U_{Fe} = 4.0 eV, J_{Fe}= 0.8eV)[146] and that for FeS[147] is 2.0 eV. In the case of Fe-pnictides, U_{eff} is about 1 eV ($U_{Fe}\leq$ 2.0 eV, J_{Fe} = 0.8 eV) using the effective Hamiltonian model.[148] In the case of FeNi, it is 0.9 eV (U_{Fe}= 1.8 eV, J_{Fe}= 0.9 eV) using the LSDA + U method.[149] The screening effect in an Fe alloy may be enhanced compared with that in an insulator, which is consistent with the value of U_{eff} (= 1 eV) used in this work.

The value of U_{eff} used in calculations based on the LSDA+U method reported for $ZnRh_2O_4$ is 2.8 eV (U_{Rh} = 3.4 eV, J_{Rh}= 0.6 eV)[150] and that used in calculations based on the GGA +U method for $LaCo_{1-x}Rh_xO_3$ oxides is 2.7 eV (U_{Rh} = 2.7 eV, J_{Rh}= 0 eV).[151] Similarly, the screening effect in Rh alloys may be enhanced compared with that in insulators, which is consistent with the value of U_{eff} (= 0.95 eV) used in this work.

A.4 Superexchange

The superexchange interaction[152, 153] acts between two magnetic ions through a shared nonmagnetic ion (anion). This interaction can occur as a result of virtual electron transfers from the shared anion to the interacting magnetic ions. The magnetic interaction between the magnetic moments of ions is determined on the basis of the Goodenough-Kanamori rules.[154), 155] These rules indicate that the state of the magnetic ions is determined by the relationship between the d electron state of the ions and the angle between the magnetic ion (cation)-nonmagnetic ion (anion)-magnetic ion (cation) as illustrated in Fig. 22. For example, with the same kind of magnetic ions and

the angle being 180°, the superexchange interaction is AFM, while if the angle is 90° (except for the electronic configuration d^5), the superexchange interaction is FM.

We refer to Fig. 23, to explain the origin of the superexchange interaction. There is an anion *b* between two magnetic ion, *a* and *c*. In the ground state Ψ^A, there is one electron in each magnetic ion with orbitals ϕ_a and ϕ_c, respectively. There are two electrons in the orbital ϕ_b of the anion *b*. In the excited state Ψ^B, one electron of the anion in Ψ^A transfers to ϕ_c. In the excited state Ψ^C, one electron of an anion in Ψ^A transfers to ϕ_a. Ψ^A, Ψ^B and Ψ^C are expressed by means of electron orbitals as (i) $\phi_a(3)\phi_b(1)\phi_b(2)\phi_c(4)$, (ii) $\phi_a(3)\phi_b(4)\phi_c(1)\phi_c(2)$ and (iii) $\phi_a(1)\phi_a(2)\phi_b(3)\phi_c(4)$ where electrons in the same orbital are numbered 1 and 2. The above four-electron problem is treated.

In order to calculate the matrix element, for example, we calculate H_{14}^{AB}.

$$H_{14}^{AB} = \int \psi^{A*} H P_{14}^{r} \psi^{B*} d\mathbf{r}$$

$$= \int \phi_b^*(1)\phi_b^*(2)\phi_a^*(3)\phi_c^*(4) H \phi_b(1)\phi_c(2)\phi_a(3)\phi_c(4) d\mathbf{r} \equiv b, \qquad \text{(A4.1)}$$

where P_{14} is the permutation matrix between 1 and 4 and *H* is the Hamiltonian.

$$H_{13}^{AC} = H_{23}^{AC} = \pm b. \qquad \text{(A4.2)}$$

The following exchange integrals *J* and *J*' are given by

$$H_{34}^{BB} = J = \int \phi_a^*(3)\phi_b^*(4)\frac{e^2}{r_{34}}\phi_b(3)\phi_a(4) d\mathbf{r_3} d\mathbf{r_4}, \qquad \text{(A4.3)}$$

$$H_{13,24}^{BC} = J' = \int \phi_c^*(1)\phi_b^*(4)\frac{e^2}{r_{14}}\phi_b(1)\phi_a(4) d\mathbf{r}_1 d\mathbf{r_4}. \qquad \text{(A4.4)}$$

Finally, the energy can be solved using a secular equation regarding the configuration interaction consisting of Ψ^A $\Psi^{even} = \frac{1}{\sqrt{2}}\left(\Psi^B \pm \Psi^C\right)$ and $\Psi^{odd} = \frac{1}{\sqrt{2}}\left(\Psi^B \mp \Psi^C\right)$. We solve the following secular equation (the detailed derivation is omitted and refer to Ref. 156).

$$\begin{vmatrix} -E & -\sqrt{2}b & 0 \\ -\sqrt{2}b & \Delta E \pm J' - \left(J \pm J'\right)P_{34}^{\sigma} - E & 0 \\ 0 & 0 & \Delta E \mp J' - \left(J \mp J'\right)P_{34}^{\sigma} - E \end{vmatrix} = 0, \qquad \text{(A4.5)}$$

where ΔE is the energy difference between the excited and ground configurations.

The obtained E is given by

$$E \cong -J_{eff}\left(\mathbf{S_3} \cdot \mathbf{S_4}\right),$$

$$J_{eff} = \frac{4b^2}{\left(\Delta E\right)^2}\left(J + J'\right). \qquad \text{(A.4.6)}$$

The sign of J_{eff} depends on $J + J'$.

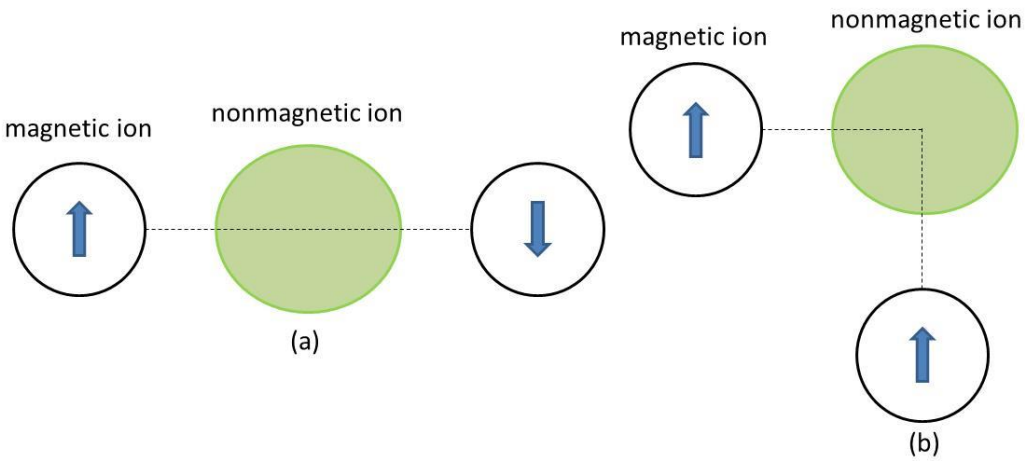

Fig. 22. Example of the superexchange interaction. (a) The angle between the magnetic ion-nonmagnetic ion-magnetic ion=180° and (b) the angle between the magnetic ion-nonmagnetic ion-magnetic ion=90°.

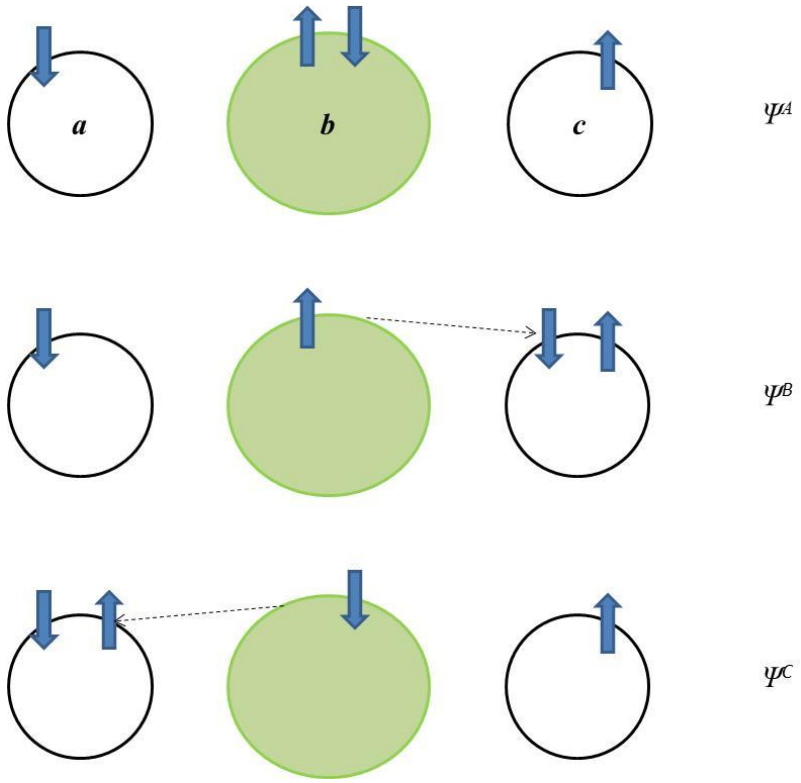

Fig. 23. The possible electronic states in the case of the superexchange interaction. Ψ^A is the ground state, and Ψ^B and Ψ^C are excited states. The arrows represent the directions of the spin.

A.5 PM state

The electronic structures of FeRh in the PM state were investigated. In the case of the PM state, the initial magnitudes of the magnetic moments at the two positions of the Fe and Rh atoms are both $0\mu_B$. The relationship between the total energy of the PM state and the lattice constant was investigated and is shown in Fig. 24. In this case, the energy of the PM state has its minimum at a_{PM} = 2.915 Å, which is much less than both a_{AFM} and a_{FM}. The obtained a_{PM} is unreasonable, because the FM-PM phase transition is a second order phase transition. The energy difference between the PM and AFM states, and the energy difference between the PM and FM states are very large because the energy of the PM state obtained lacks the effect of the random distribution of the direction of the magnetic moments of the Fe atoms above T_c. In order to discuss the FM-PM phase transition in real FeRh, it is necessary to include the above effect in calculating the PM state. However, this calculation is beyond the present work. The DOS near E_F of the PM state of FeRh is calculated and shown Fig. 25. The $D(E_F)$ of the PM state is higher than that of both the AFM and FM states.

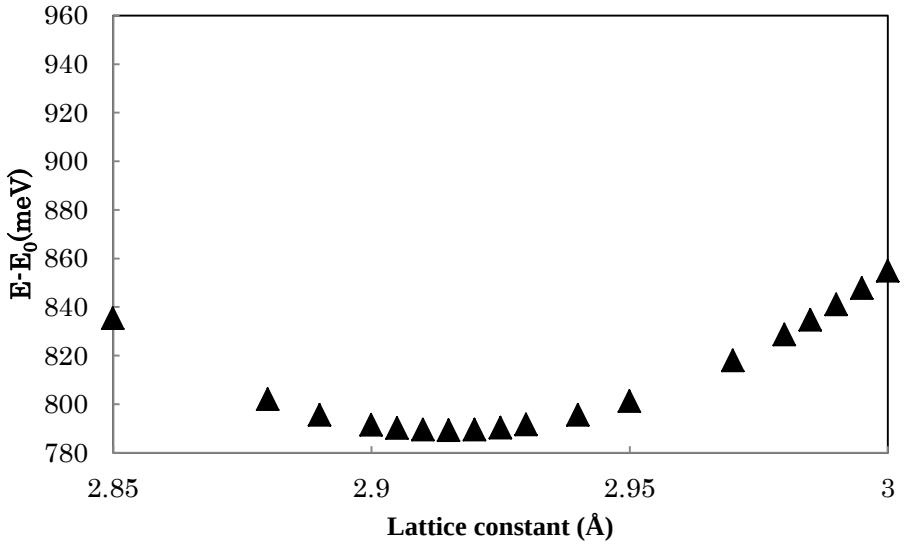

Fig. 24. Total energy of the PM state versus lattice constant with U_{Fe}= 2.0 eV and U_{Rh}= 1.95 eV using the GGA + U method, where the minimum of the AFM state is set to zero.

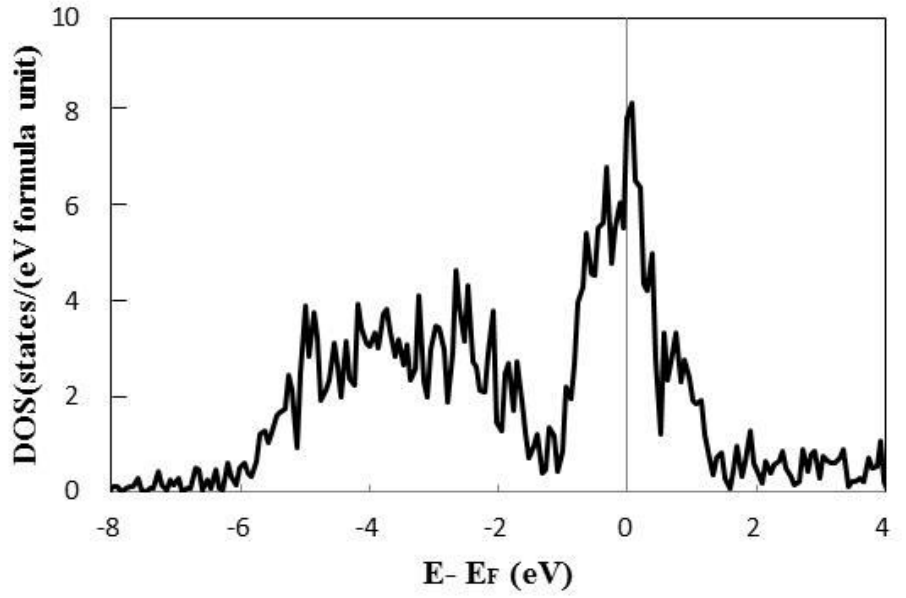

Fig. 25. DOS near E_F of the PM state of FeRh with a_{PM} = 1.915 Å, and U_{Fe}= 2.0 eV and U_{Rh} =1.95 eV using the GGA + U method.

A.6 Stoner mechanism

In this appendix, the Stoner mechanism for FM metals[157-160] is explained in order to understand the stability of the FM and PM states. The Stoner model can be formulated using the energy relationship for spin up and spin down electrons.

$$E_{\uparrow}(k) = \varepsilon(k) - I\frac{N_{\uparrow} - N_{\downarrow}}{N}, \tag{A.6.1}$$

$$E_{\downarrow}(\mathbf{k}) = \varepsilon(\mathbf{k}) + I\frac{N_{\uparrow} - N_{\downarrow}}{N}, \tag{A.6.2}$$

$$N = N_{\uparrow} + N_{\downarrow}. \tag{A.6.3}$$

where $\varepsilon(\mathbf{k})$ is the dispersion relation of the electrons without taking account of the spin, $N_{\uparrow}$ and $N_{\downarrow}$ are the up spin electron number and the down spin electron number, respectively, and I is the exchange energy, which is called the Stoner parameter.

$$\text{The FM state occurs if } \quad IN(E_F) > 1, \tag{A.6.4}$$

where $N(E_F)$ is the DOS per atom per spin at E_F.

We investigated whether the Stoner criterion for the obtained electronic structures of FeRh is satisfied or not. The Stoner criterion for alloy systems is expressed as follows.

$$I_{\text{alloy}} * N_{\text{alloy}}(E_F) \geq 1, \tag{A.6.5}$$

where I_{alloy} is the generalized Stoner parameter, and $N_{\text{alloy}}(E_F)$ is the DOS per atom per spin at E_F of the alloy. The value of $N_{\text{alloy}}(E_F)$ obtained in the present work is 2.1. The Stoner parameter of an alloy system is computed using the following formula.[161]

$$I_{\text{alloy}} = \sum_{Q} I_Q \left(N_Q(E_F) / N(E_F) \right)^2, \tag{A.6.6}$$

where I_Q is the local spin density Stoner parameter. Because Stoner parameters have been calculated to date, we used the reported values. From I_{Fe} = 0.91 eV for a BCC Fe crystal and I_{Rh}=0.61 eV for a FCC Rh crystal,[162] we obtain

$$I_{alloy} * N_{alloy}(E_F) \approx 1.61. \quad \text{(A.6.7)}$$

Petukhov et al.[163] suggested that $D(E_F)$ (or $N(E_F)$) is underestimated using the LSDA +U method, so I_Q must be increased. Therefore, I_{alloy}* $N_{alloy}(E_F)$ in equation A.6.7 is greater than 1.61.This suggests that at least, at 0 K, the FM state is more stable than the PM state. In fact, the FM state is more stable than the PM state below T_c (the AFM state is more stable than the FM state below T_{tr}). Therefore, the Stoner criterion for FeRh is satisfied. The above result is consistent with that obtained by Kulikov et al.[63]

A.7 Relationship between the origin of the IMCE of FeRh and those for the AFM-FM and AFM-FI phase transitions

In spite of the differences in crystal structure between Mn_3GaC[15], (Co,Fe)MnP[16], $Mn_{2-x}Cr_xSb$[17] and FeRh, they have similar IMCEs corresponding to temperature and an applied magnetic field. Therefore, the origins of their IMCEs may be similar. Therefore, we investigated the origins of the IMCEs of these other materials and compared them with that of FeRh.

In particular, Caron et al.[17] suggested that the IMCE in $Mn_{2-x}Cr_xSb$ could be predicted from the occurrence of the AFM-FI phase transition without an applied magnetic field. Mn_2Sb is in a FI state with T_c around 550K and has a tetragonal Cu_2Sb –type structure. The magnetic structure consists of Mn_I and Mn_{II} sublattices stacked in triple layers in a Mn_I-Mn_{II}-Mn_{II} structure that repeats along the c-direction. Both sublattices show FI interlayer interactions, with the Mn_{II} moment being roughly twice that of Mn_I, both parallel to the tetragonal axis. However, adjacent Mn_I-Mn_{II} layers couple antiparallel to each other, while Mn_{II}-Mn_{II} layers couple parallel to each other,

resulting in a FI Mn_I-Mn_{II}-Mn_{II} configuration. The magnetic properties change drastically if parts of the Mn atoms are substituted. In the case of $Mn_{2-x}Cr_xSb$, it has a FI Mn_I-Mn_{II}-Mn_{II} configuration. Below a critical distance between adjacent Mn_{II} layers, due to the Pauli exclusion principle, interlayer exchange interactions must change and become a AFM Mn_I-Mn_{II}-Mn_{II} configuration, in a phenomenon known as exchange inversion proposed by Kittel.

However, we think that the origin of the IMCE in $Mn_{2-x}Cr_xSb$ can be understood using the electronic and magnetic entropy changes between the AFM and FI states (the DOS for their states was calculated by Wijngaard et al. using the ASW method,[164] in spite of the total energies of the AFM and FI states not being calculated.). We think that this is similar to the origin of the IMCE in FeRh. The value of $|\Delta T_{ad}|$ for $Mn_{2-x}Cr_xSb$ under an applied magnetic field (= 1 T) is 6.7 K and is almost the same as that of FeRh. It is much larger than that of normal MCMs such as $Gd_5Si_2Ge_2$,[7] $MnAs_{1-x}Sb_x$,[8] $MnFeP_{0.45}As_{0.55}$,[9] $La(Fe_xSi_{1-x})_{13}H_y$,[10] MnFe(P, Si)[11] and so on (ΔT_{ad} is at most around 3.0 K under 1 T).

The electronic and magnetic structures of Mn_3GaC have been reported by Shirai et al.[165] who unfortunately found that the total energy of the FM state was more stable than that of the AFM state, in disagreement with the experimental evidence. We think that their calculation method was insufficient to understand the electronic and magnetic structures of Mn_3GaC because they did not contain *U*. In Mn_3GaC, a volume contraction occurs with the AFM-FM phase transition, which is different from FeRh. The origin of the IMCE seems to be similar to that of FeRh.

There are few experiments concerning (Co,Fe)MnP, therefore, we are unable to comment on the origin of the IMCE in (Co,Fe)MnP.

Because the origins of the IMCEs of the above IMCMs seem to be similar to that of FeRh, utilization of IMCMs with an AFM-FM phase transition or an AFM-FI phase transition may be more advantageous than that of MCMs in order to obtain a material with large $|\Delta T_{ad}|$ at room temperature under a low applied magnetic field.

References

1) V. K. Pecharsky and K. A. Gschneidner Jr, J. Magn. Magn. Mater. **200**, 44 (1999).

2) A. M. Tishin and Y. I. Spichkin, “The Magnetocaloric Effect and its Applications”, Taylor & Francis, 2003.

3) S. L. Russek and C. B. Zimm, Int. J. Refrig. **29**, 1366 (2006).

4) A. Kitanovski and P. W. Egolf, Int. J. Refrig. **29**, 3 (2006).

5) K. G. Sanderman, Scripta Mater. **67**, 566 (2012).

6) O. Sari and M. Balli, Int. J. Refrig. **37**, 8 (2014).

7) V. K. Pecharsky and K. A. Gschneidner, Jr., Phys. Rev. Lett. **78**, 4494 (1997).

8) H. Wada and Y. Tanabe, Appl. Phys. Lett. **79**, 3302 (2001).

9) O. Tegus, E. Brück, K. H. J. Buschow, and F. R. de Boer, Nature **415**, 150 (2001).

10) A. Fujita, S. Fujieda, Y. Hasegawa, and K. Fukamichi, Phys. Rev. B **67**, 104416 (2003).

11) N. H. Dung, Z. Q. Ou, L. Caron, L. Zhang, D. T. C. Thanh, G. A. de Wijs, R. A. de Groot, K. H. J. Buschow, and E. Brück, Adv. Energy Mater. **1**, 1215 **(**2011**)**.

12) M. P. Annaorazov, K. A. Asatryan, G. Myalikgulyev, S. A. Nikitin, A. M. Tishin, and A. L. Tyurin, Cryogenics. **32**, 867 (1992).

13) M. P. Annaorazov, S. A. Nikitin, A. L. Tyurin, K. A. Asatryan, and A. Kh. Dovletov, J. Appl. Phys. **79**, 1689 (1996).

14) M. P. Annaorazov, M. Ünal, S. A. Nikitin, A. L. Tyurin, K. A. Asatryan, and A. Kh. Dovletov, J Alloy Compd. **348**, 18 (2003).

15) Ö. Çakır and M. Acet, Appl. Phys. Lett. **100**, 202404 (2012).

16) F. Guillou and E. Brück, J. Appl. Phys. **114**, 143903 (2013).

17) L. Caron, X. F. Miao, J. C. P. Klaasse, S. Gama, and E. Brück, Appl. Phys. Lett. **103**, 112404 (2013).

18) L. J. Swartzendruber, Bull. Alloy Phase Diagrams **5**, 45662 (1984).

19) V. I. Zverev, A. M. Tishin, and M. D. Kuz’min, J. Appl. Phys. **107**, 043907 (2010).

20) A. M. Tishin and Y. I. Spichkin, Int. J. Refrig. **37**, 223 (2014).

21) M. Fallot, Ann. Phys. **10**, 291 (1938).

22) T. Miyanaga, T. Itoga, T. Okazaki, and K. Nitta, J. Phys. Conf. Ser. **190**, 012097 (2009).

23) A. I. Zakharov, A. M. Kadomtseva, R. Z. Levitin, and E. G. Ponyatovskii, Soviet Phys. JETP **19**, 1348 (1964).

24) D. W. Cooke, F. Hellman, C. Baldasseroni, C. Bordel, S. Moyerman, and E. E. Fullerton, Phys. Rev. Lett. **109**, 255901 (2012).

25) G. Shirane, C. W. Chen, P. A. Flinn, and R. Nathans, Phys. Rev. **131**, 183 (1963).

26) G. Shirane, R. Nathans, and C. W. Chen, Phys. Rev. **134**, A1547 (1964).

27) N. Kunitomi, M. Kohgi, and Y. Nakai, Phys. Lett. A **37**, 333 **(**1971).

28) J. B. McKinnon, D. Melville, and E. W. Lee, J. Phys. C **3**, S46 **(**1970).

29) B. K. Ponomarev, Sov. Phys. JETP **36**, 105 (1973).

30) T. Zhou, M. K. Cher, L. Shen, J. F. Hu, and Z. M. Yuan, Phys. Lett. A **377**, 3052 (2013).

31) I. Suzuki, T. Naito, M. Itoh, T. Sato, and T. Taniyama, J. Appl. Phys. **109**, 07C717 (2011).

32) J. U. Thiele, S Maat, and E. E Fullerton, Appl. Phys. Lett. **82**, 2859 (2003).

33) M. R. Ibarra and P. Algarabel, Phys. Rev. B **50**, 4196 (1994).

34) C. Marquina, M. R. Ibarra, P. A. Algarabel, A. Hernando, P. Crespo, P. Agudo, A. R. Yavari, and E. Navarro, J. Appl. Phys. **81**, 2315 (1997).

35) J.-S. Lee, E. Vescovo, L. Plucinski, C. M. Schneider, and C.-C. Kao, Phys. Rev. B **82**, 224410 (2010).

36) A. X. Gray, D. W. Cooke, P. Krüger, C. Bordel, A. M. Kaiser, S. Moyerman, E. E. Fullerton, S. Ueda, Y. Yamashita, A. Gloskovskii, C. M. Schneider, W. Drube, K. Kobayashi, F. Hellman, and C. S. Fadley, Phys. Rev. Lett. **108**, 257208 (2012).

37) P. Tu, A. J. Heeger, J. S. Kouvel, and J. B. Comly, J. Appl. Phys. **40**, 1368 (1969).

38) J. Ivarsson, G.R. Pickett, and J. Tóth, Phys. Lett. A **35**, 167 (1971).

39) M. A. de Vries, M. Loving, A. P. Mihai, L. H. Lewis, D. Heiman, and C. H. Marrows, New J Phys. **15**, 013008 (2013).

40) C. J. Schinkel, R. Hartog, and F. H. A. M. Hochstenbach, J. Phys. F **4**, 1412 (1974).

41) L. I. Vinokurova, A. V. Vlasov, and M. Pardavi-Horváth, Physica Status Solidi B **78**, 353 (1976).

42) L. I. Vinokurova, A. V. Vlasov, N. I. Kulikov, and M. Pardavi-Horvath, J. Magn. Magn. Mater. **25**, 201 (1981).

43) S. A. Nikitin, M. P. Annaorazov, V. Y. Bodriakov, and A. L. Tyurin, Phys. Lett. A **176**, 275 (1993).

44) J. S. Kouvel, J. Appl. Phys. **37**, 1257 (1966).

45) J. M. Lommel, J. Appl. Phys. **40**, 3880 (1969).

46) Y. Feng, T. Fukuda, and T. Kakeshita, Intermetallics **36**, 57 (2013).

47) M. Sharma, H. M. Aarbogh, J.-U. Thiele, S.Maat, E. E. Fullerton, and C. Leighton, J. Appl. Phys. **109**, 083913 (2011).

48) S. O. Mariager, F. Pressacco, G. Ingold, A. Caviezel, E. Möhr-Vorobeva, P. Beaud, S. L. Johnson, C. J. Milne, E. Mancini, S. Moyerman, E. E. Fullerton, R. Feidenhans'l, C. H. Back, and C. Quitmann, Phys. Rev. Lett. **108**, 087201 (2012).

49) M. Loving, F. Jimenez-Villacorta, B. Kaeswurm, D. A. Arena, C. H. Marrows, and L . H. Lewis, J. Phys. D: Appl. Phys. **46**, 162002 (2013).

50) C. Baldasseroni, C. Bordel, A. X. Gray, A. M. Kaiser, F. Kronast, J. Herrero-Albillos, C. M. Schneider, C. S. Fadley, and F. Hellman, Appl. Phys. Lett. **100**, 262401 (2012).

51) Y. Choi, D. J. Keavney, M. V. Holt, V. Uhlíř, D. Arena, E. E. Fullerton, P. J. Ryan, and Jong-Woo Kim, arXiv:1405.4319 (2014).

52) G. Ju, J. Hohlfeld, B. Bergman, R. J. M. van de Veerdonk, O. N. Mryasov, J.-Y. Kim, X. Wu, D. Weller, and B. Koopmans, Phys. Rev. Lett. **93**, 197403 (2004).

53) B. Bergman, G. Ju, J. Hohlfeld, R. J. M. van de Veerdonk, J.-Y. Kim, X. Wu, D. Weller, and B. Koopmans, Phys. Rev. B **73**, 060407(R) (2006).

54) H. Kumar, M. C. A. Fantini, and D. R. Cornejo, IEEE Trans. Magn. **49**, 4506 (2013).

55) E. Mancini, F. Pressacco, M. Haertinger, E. E. Fullerton, T. Suzuki, G. Woltersdorf, and C. H. Back, J. Phys. D: Appl. Phys. **46**, 245302 (2013).

56) S. Maat, J.-U. Thiele, and E. E. Fullerton, Phys. Rev. B **72**, 214432 (2005).

57) C. Kittel, Phys. Rev. **120**, 335 (1960).

58) J. A. Ricodeau and D. Melville, J. Phys. F **2**, 337 (1972).

59) T. Moriya and K. Usami, Solid State Comm. **23**, 935 (1977).

60) Y. Teraoka and J. Kanamori, Physica B **91**, 199 (1977).

61) H. Hasegawa, J. Phys. Soc. Jpn. **49**, 178 (1980).

62) M. A. Khan, Y. Khwaja, and C. Demangeat, J. Physique **42**, 573 (1981).

63) N. I. Kulikov, E. T. Kulatov, L. I. Vinokurova, and M. Pardavi-Horvath, J. Phys. F **12**, 91 (1982).

64) C. Koenig, J. Phys. F:Met. Phys. **12**, 1123 (1982).

65) V. L. Moruzzi and P. M. Marcus, Phys. Rev. B **46**, 2864 (1992).

66) V. L. Moruzzi and P. M. Marcus, Solid State Commun. **83**, 735 (1992).

67) V. L. Moruzzi and P. M. Marcus, Phys. Rev. B **46**, 14198 (1992).

68) V. L. Moruzzi and P. M. Marcus, Phys. Rev. B **48**, 16106 (1993).

69) A. Szajek and J. A. Morkowski, J**.** Magn**.** Magn. Mater. **115**, 171 (1992).

70) A. Szajek and J. A. Morkowski, Physica B **193**, 81 (1994).

71) M. Pugacheva, J. A. Morkowski, A. Jezierski, and A. Szajek, Solid State Commun. **92**, 731 (1994).

72) Y.-M. Zhou, X. Gao, and D.-S. Wang, J**.** Magn**.** Magn. Mater. **226**, 1042 (2001).

73) M. E. Gruner, E. Hoffmann, and P. Entel, Phys. Rev. B **67**, 064415 (2003).

74) R. Y. Gu and V. P. Antropov, Phys. Rev. B **72**, 012403 (2005).

75) K. Uebayashi, H. Shimizu, and H. Yamada, Mater. Trans. **47**, 456 (2006).

76) K. Nakada and H. Yamada, J**.** Magn**.** Magn. Mater**. 310**, 1046 (2007).

77) Y. Kaneta, S. Ishino, Y. Chen, S. Iwata, and A. Iwase, Jpn. J. Appl. Phys. **50**, 105803 (2011).

78) L. M. Sandratskii and P. Mavropoulos, Phys. Rev. B **83**, 174408 (2011).

79) L. M. Sandratskii and P.Buczek, Phys. Rev. B **85**, 020406(R) (2012).

80) P. M. Derlet, Phys. Rev. B **85**, 174431 (2012).

81) J. Barker and R. W. Chantrell, arXiv:1405.3043 (2014).

82) J. B. Staunton, R. Banerjee, M. dos Santos Dias, A. Deák, and L. Szunyogh, Phys. Rev. B **89**, 054427 (2014).

83) A. Deák, E. Simon, L. Balogh, L. Szunyogh, M. dos Santos Dias, and J. B. Staunton, Phys. Rev. B **89**, 224401 (2014).

84) J. Kudrnovský, V. Drchal, and I. Turek**,** Phys**.** Rev. B **91**, 014435 **(**2015).

85) M. Born, R. Oppenheimer, Ann. Physik **84**, 457 (1927).

86) L. H. Thomas, Proc. Camb. Phil. Soc. **23**, 542 (1927).

87) E. Fermi, Z. Physik **48**, 73 (1928).

88) P. Hohenberg and W. Kohn, Phys. Rev. **136**, 864 (1964).

89) W. Kohn and L. J. Sham, Phys. Rev. **140**, 1133 (1965).

90) P. A. M. Dirac, Proc. Cambridge Philos. Soc. **26**, 376 (1930).

91) M. Gell-Mann and K. A. Brueckner, Phys. Rev. **106**, 364 (1957).

92) W. J. Carr, Jr. and A. A. Maradudin, Phys. Rev. **133**, A371 (1964).

93) D. M. Ceperley and B. J. Alder, Phys. Rev. Lett. **45**, 566 (1980).

94) J. P. Perdew and A. Zunger, Phys. Rev. B, **23**, 5048 (1981).

95) J. P. Perdew, K. Burke, and M. Ernzerhof, Phys. Rev. Lett. **77**, 3865 (1996).

96) J. P. Perdew, K. Burke, and M. Ernzerhof. Erratum, Phys. Rev. Lett. **78**, 1396 (1997).

97) A. I. Liechtenstein, V. I. Anisimov, and J. Zaanen, Phys. Rev. B **52**, R5467 (1995).

98) B. Himmetoglu, A. Floris, S. de Gironcoli and Matteo Cococcioni, arXiv:1309.3355 (2013).

99) S. L. Dudarev, G. A. Botton, S. Y. Savrasov, C. J. Humphreys, and A. P. Sutton, Phys. Rev. B **57**, 1505 (1998).

100) O.K. Andersen, Phys. Rev. B **12**, 3060 (1975).

101) D. R. Hamann, M. Schlüter and C. Chiang, Phys. Rev. Lett. **43**, 1494 (1979).

102) D. Vanderbilt, Phys. Rev. B **41**, 7892 (1990).

103) P. E. Blöchl, Phys. Rev. B **50**, 17953 (1994).

104) G. Kresse and D. Joubert, Phys. Rev. B **59**, 1758 (1999).

105) G. Kresse and J. Furthmüller, Comput. Mat. Sci., **6**, 15 (1996).

106) G. Kresse and J. Furthmüller, Phys. Rev. B, **54**, 11169 (1996).

107) P. Pou, F. Flores, J. Ortega, R. Pérez, and A. L. Yeyati, J. Phys.: Condens. Matter **14**, 421 (2002).

108) A. I. Lichtenstein, M. I. Katsnelson, and G. Kotliar, Phys. Rev. Lett. **87**, 067205 (2001).

109) J. Łażewski, P. Piekarz, AM Oleś, and K. Parlinski, Phys. Rev. B **74**, 174304 (2006).

110) I. V. Solovyev, P. H. Dederichs, and V. I. Anisimov, Phys. Rev. B **50**, 16861 (1994).

111) N. Stojic, N. Binggeli, and M. Altarelli, Phys. Rev. B **73**, 100405(R) (2006).

112) H. J. Monkhorst and J. D. Pack, Phys. Rev. B **13**, 5188 (1976).

113) M. Methfessel and A. T. Paxton, Phys. Rev. B **40**, 3616 (1989).

114) D. van der Marel and G. A. Sawatzky, Phys. Rev. B **37**, 10674 (1988).

115) J. E. Sansonettia and W. C. Martin, J. Phys. Chem. Ref. Data, **34**, 1559 (2005).

116) I. Seki and K. Nagata, ISIJ International **45**, 1789 (2005).

117) G. Ghosh and G. B. Olson, Acta Materialia **50**, 2655 (2002).

118) K. Miyoshi and D. H. Buckley, NASA technical paper 1883 (1981).

119) Z.-Y. Zeng, C.-E. Hu, X.-R. Chen,L.-C. Cai, andF.-Q. Jing, J. Phys.: Condens. Matter, **20**, 425217 (2008).

120) D. Chandesris, J. Lecante, and Y. Petroff, Phys. Rev. B **27**, 2630 (1983).

121) H. Kato, T. Ishii, S. Masuda, Y. Harada, T. Miyano, T. Komeda, M. Onchi, and Y. Sakisaka, Phys. Rev. B **32**, 1992 (1985).

122) S. Raaen and V. Murgai, Phys. Rev. B **36**, 887 (1987).

123) K. B. Hathaway, H. J. F. Jansen, and A. J. Freeman, Phys. Rev. B **31**, 7603 (1985).

124) D. J. Singh, W. E. Pickett, and H. Krakauer, Phys. Rev. B **43**, 11628 (1991).

125) H. Wang, P.-W. Ma, and C. H. Woo, Phys. Rev. B **82**, 144304 (2010).

126) M. Cococcioni and S. de Gironcoli, Phys. Rev. B **71**, 035105 (2005).

127) J. W. Arblaster, Platinum Metah Rev. **41**, 184 (1997).

128) E. Walker, J. Ashkenazi, and M. Dacorogna, Phys. Rev. B **24**, 2254 (1981).

129) J. Merker, D. Lupton, M. Töpfer, and H. Knake, *Platinum Metals Rev.*, 2001, **45**, 74 (2001).

130) L. M. García-Cruz and R. Baquero. Rev. Mex. Fis **49**, 317 (2003).

131) D. T. Pierce and W. E. Spicer, Phys. Rev. B **5**, 2125 (1972).

132) G. Borstel, W. Braun, M. Neumann, and G. Seitz, Phys. Status Solidi(b) **95**, 453 (1979).

133) G. Borstel, M. Neumann, and W. Braun, Phys. Rev. B **23**, 3113 (1981).

134) H. Höchst and M. K. Kelly, Phys. Rev. B **30**, 1708 (1984).

135) N. E. Christensen, Phys. Status Solidi B **55**, 117 (1973).

136) V. L. Moruzzi and P. M. Marcus, Phys Rev B **39**, 471 (1989).

137) R. Gaudoin, W. M. C. Foulkes, and G. Rajagopal, J. Phys.: Condens. Matter **14**, 8787 (2002).

138) B. Lee and R. E. Rudd, Phys. Rev. B **75**, 195328 (2007).

139) W. Nolting and A. Ramakanth, "Quantum Theory of Magnetism", springer 2009.

140) U. Mizutani, "Introduction to the Electron Theory of Metals", Cambridge University Press, 2003, p. 269.

141) N. A. de Oliveira and P. J. von Ranke, Phys. Rep. **489**, 89 (2010).

142) E. P. Nóbrega, N. A. de Oliveira, P. J. von Ranke and A. Troper, J. Appl. Phys. **99**, 08Q103 (2006).

143) V. I. Anisimov and O. Gunnarsson, Phys. Rev. B **43**, 7570 (1991).

144) M. M. Steiner, R.C. Albers, and L.J. Sham, Phys. Rev. B **45**, 13272 (1992).

145) N. L Stojić and N.L Binggeli, J. Magn. Magn. Mater. **320**, 100 (2008).

146) P. Piekarz, K. Parlinski, and A. M. Oleś, Phys. Rev. B **76**, 165124 (2007).

147) A. Devey and N. H. de Leeuw, Phys. Rev. B **82**, 235112 (2010).

148) W. L. Yang, A. P. Sorini, C-C. Chen, B. Moritz, W.-S. Lee, F. Vernay, P. Olalde-Velasco, J. D. Denlinger, B. Delley, J.-H. Chu, J. G. Analytis, I. R. Fisher, Z. A. Ren, J. Yang, W. Lu, Z. X. Zhao, J. van den Brink, Z. Hussain, Z.-X. Shen, and T. P. Devereaux, Phys. Rev. B **80**, 014508 (2009).

149) J. Minár, S. Mankovsky, O. Šipr, D. Benea, and H. Ebert, J. Phys. Condens. Matter **26**, 274206 (2014).

150) N. Mansourian-Hadavi, S. Wansom, N. H. Perry, A. R. Nagaraja, T. O. Mason, L. Ye, and A. J. Freeman, Phys. Rev. B **81**, 075112 (2010).

151) K. Knížek, J. Hejtmánek, M. Maryško, Z. Jirák, and J. Buršík, Phys. Rev. B **85**, 134401 (2012).

152) H. A. Kramers, Physica **1**, 182 (1934).

153) P. W. Anderson, Phys. Rev. **79**, 350 (1950).

154) J. B. Goodenough, J. Phys. Chem. Solids **6**, 287 (1958).

155) J. Kanamori, J. Phys. Chem. Solids **10**, 87 (1959).

156) T. Oguchi,"Statistical Theory of Magnetism**"**, Shokabo, 1970 (in Japanese).

157) L. Fritsche and B. Weimert, Phys. Status Solidi B **208**, 287 (1998).

158) R. M. White, "Quantum Theory of Magnetism", 3rd Edition, Springer-Verlag, 2007.

159) E. C. Stoner, Proceedings of the Royal Society of London. Series A, Mathematical and Physical Sciences, **165**, 372 (1938).

160) M. Shimizu, Rep. Prog. Phys. **44**, 329 (1981).

161) S.S. Jaswal, Solid State Commun. **52**, 127 (1984).

162) O. K. Andersen, J. Madsen, U. K. Poulsen, O. Jepsen, and J. Kollár, Physica B+C, **86-88**, 249 (1977).

163) A. G. Petukhov, I. I. Mazin, L. Chioncel, and A. I. Lichtenstein, Phys. Rev. B **67**, 153106 (2003).

164) J. H. Wijngaard, C. Haas, and R. A. de Groot, Phys. Rev. B **45**, 5395 (1992).

165) M. Shirai**,** Y. Ohata**,** N. Suzuki, and K. Motizuki, Jpn**.** J. Appl. Phys. **32**, 250 (1993).